1. TESTS OF THE COUPLED SHOCK TUBE/MASS-SPECTROMETER TECHNIQUE

2. THE PYROLYSIS OF NEOPENTANE BY ATOMIC RESONANCE ABSORPTION SPECTROPHOTOMETRY

by

Diane Lois Bernfeld

Dissertation submitted to the Faculty of the

Virginia Polytechnic Institute and State University

in partial fulfillment of the requirements for the degree of

DOCTOR OF PHILOSOPHY

in

Chemistry

APPROVED:

J. F. Wolfe, Chairman

R. L. Belford

G. B. Skinner

H. M. McNair

R. E. Dessy

E. F. Brown

July, 1982

Blacksburg, Virginia

ACKNOWLEDGMENTS

The successful completion of the research studies presented in this dissertation could not have been accomplished without the continual support and persistent efforts of Dr. David Roselle, Dean of Research and Graduate Studies. The highest standards of academic tradition hallmarked his intellectual honesty and scientific integrity. It has been a privilege to know him as a friend during my years at Virginia Tech.

Professor R. L. Belford, my former teacher at the University of Illinois, followed my career and beyond the call of duty, joined my advisory committee. The scientific insights that he taught me have been the basis of my learning during my years in graduate school. This enduring friendship has meant a great deal to me.

Professor Gordon Skinner provided me with the opportunity to complete my research in his laboratory at Wright State University. His support as a committee member and his encouragement during my year at Wright State have been very much appreciated.

The help of my advisory committee members from Virginia Tech, Professors Eugene Brown, Ray Dessy, Harold McNair and my chairman, James Wolfe is gratefully acknowledged. Professor Dessy was a member of my committee from the outset of my graduate studies at Virginia Tech, and his sense of academic ethics prevailed until my studies were completed. Professor Wolfe became my chairman shortly before I went to Wright State University. He exerted every effort to bring my studies to a successful conclusion.

TABLE OF CONTENTS

PART 1. TESTS OF THE COUPLED SHOCK-

TUBE/MASS-SPECTROMETER TECHNIQUE

TABLE OF CONTENTS

PART 2. THE PYROLYSIS OF NEOPENTANE BY ATOMIC ABSORPTION SPECTROPHOTOMETRY

I. INTRODUCTION

A. Shock Tube Theory

Basically, the chemical shock tube is a tube of constant cross-sectional area separated into two sections, the driver and test sections. These two sections are divided by a breakable partition, the diaphragm. When the diaphragm ruptures, after pressuring the driver with high-pressure (usually inert) gas, the driver gas expands into the low-pressure test section and compresses and heats the gas ahead of it. A shock wave is formed as the leading edge of the compressed test gas. It moves ahead of the contact front, which is the interface between test and driver gas. The shock wave so formed is called the incident shock wave.

The incident shock wave traveling down the tube then reflects from the endwall and moves back into the heated and compressed test gas. It may then collide with the contact front and be re-reflected to the endwall. In this event, the maximum test time of our studies is the time difference between the creation of the reflected shock wave and its repropagation to the endwall after interacting with the contact front. Another possibility is that the shock wave collides with the rarefaction wave. The rarefaction wave is created simultaneously with the shock wave. It moves into the driver section, reflects from the end of the driver

section, and moves down into the test section where it may interact with the reflected shock wave. The wave diagram shown in Figure 1 shows these events as a function of time as given by ideal shock theory.[16] The maximum test time for shock tube-mass spectrometer experiments, shown as Δt experiment, is on the order of 1 msec.

During the actual performance of shock tube experiments in the laboratory, some of the experimental conditions assumed by the ideal theory (for example, instantaneous breaking of diaphragms) cannot be achieved in practice. These effects, which can cause deviations from ideal theory, are discussed in the standard shock tube references.[16]

The advantages of using shock waves in chemical kinetic studies are shown in Table 1.

B. The Use of the Free Jet in Gas-Phase Studies

An extension of the standard kinetic experiment utilizing a shock tube was created when a mass-spectrometer was coupled to a shock tube. In this technique, gas is heated to reaction by a shock wave and expands into an evacuated mass-spectrometer chamber through a pinhole orifice or nozzle. In this way, the pressure build-up does not immediately swamp the analyzer. Produce analysis is then carried out on the gas sample in which reaction has been quenched by the isentropic expansion through the nozzle.

Table 1. Advantages of Shock Heating in Chemical Kinetic Studies

1. Very rapid heating of a gas sample so that fast kinetic processes may be studied. The heating time can be on the order of a few microseconds.
2. Very high temperature may be obtained. All temperatures of interest for reactive studies are available. It is easy in a typical shock tube to heat a gas to 4000° K.
3. Selection of temperatures may be made. One can produce a range of temperatures depending on the strength of the shock used. The upper limit to the shock strength in our studies is dictated by the breaking pressure of the diaphragm of the shock tube at about 23 p.s.i.
4. Uniform heating of the test gas is obtained.

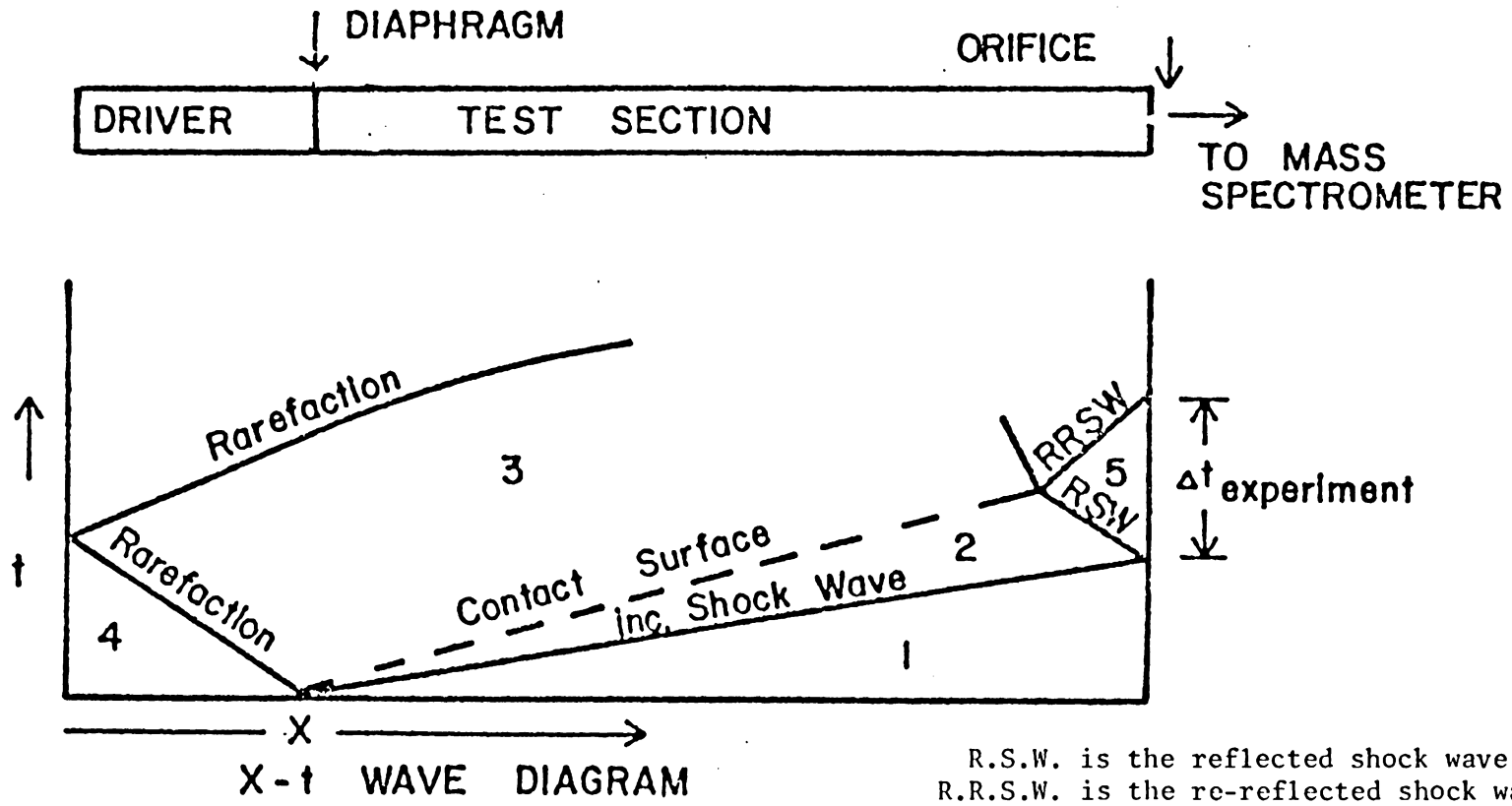

Figure 1. X-t Wave Diagram.

Region 1 - undisturbed test gas ahead of incident shock wave.
Region 2 - test gas heated by incident shock wave.
Region 3 - expanding driver gas
Region 4 - driver gas at initial conditions
Region 5 - test gas heated by reflected shock wave (R.S.W.)

However, the analysis of gas in a supersonic jet by a mass-spectrometer is certainly not restricted to kinetic experiments involving shock-heated gases. Flame studies[1-3] have been performed in which the heated gases of a burner system react and form combustion products. As in the case with shock-heated gases, any reaction is quenched by expanding the gases through a nozzle or orifice and the resulting jet flow is sampled by mass-spectrometry. Molecular beam studies involve the formation of an essentially collision-free beam to allow the microscopic properties of reactive species to be explored. The pioneering studies of Kantrowitz and Grey[5] in the early 1950's paved the way for molecular beam studies in which a supersonic jet (formed with a converging-diverging nozzle and skimmed with a cone-shaped skimmer) was used to obtain improved beam intensities.

In all of these gas-kinetic studies utilizing supersonic flow, gas streams from a high-pressure region into a low-pressure region. The characteristic plume (see Figure 2) created when high pressure gas streams through the orifice into the low pressure (mass-spectrometer) chamber is called the free jet. Such a flow pattern at (modified) Knudsen numbers K_m on the order of 0.1 or greater.

[a]See reference 58 for the use of K_m in predicting shock structures for the free jet.

The shock structure surrounding the plume (called the barrel shock) and the Mach disc are created by the interaction of the jet flow with background molecules present in the low-pressure chamber.

The structure of the free jet, so-called because the gas expands freely, without confinement by container walls, has been well-characterized. Some of its basic features are X_B, the axial distance from the orifice to the barrel (the widest part of the plume); X_M, the axial distance from the orifice to the Mach disk (terminal plane of the jet); and D_B and D_M, the diameters of the barrel and the Mach disk, respectively. Table 2 shows the relevant jet parameters for a typical shock experiment.

Some of the first studies to establish other properties of the free jet were performed with molecular beam applications in mind. Kantrowitz and Grey[5] investigated the velocity distribution of the free jet. The flow regime was that of transition flow; the flow began as continuum flow and eventually became molecular. Eventually, a theoretical model was evolved which predicted the form of the translational velocity distribution. Later experiments showed that for monatomic gases $M_T = 1.17\ Kn^{-0.4}$, where M_T is the terminal (frozen) Mach number, and Kn is the Knudsen number, as defined in Table 2. The velocity distribution in a jet with transition flow was found to be anisotropic. The distribution parallel to the direction of flow narrowed and eventually

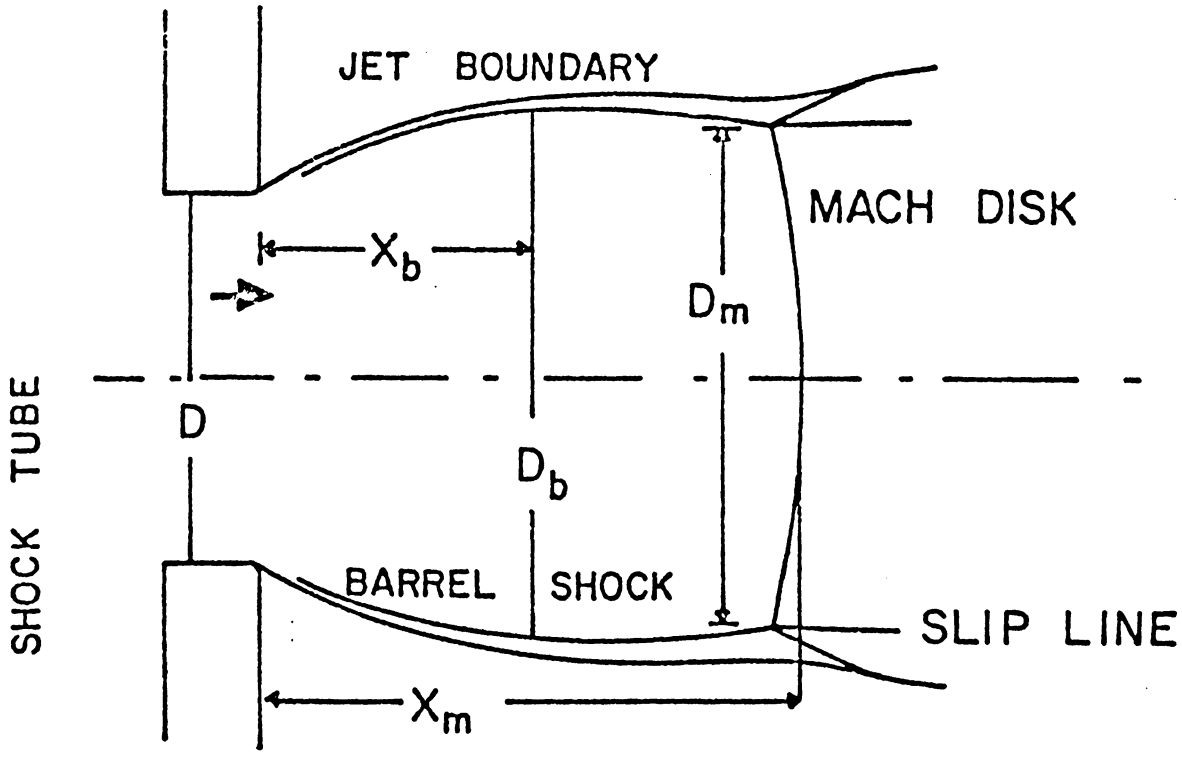

See text (Section B) for an explanation of terms. The plume shown here is the basic flow pattern obtained in chemical kinetic studies utilizing supersonic jet expansion.

Figure 2. The Free Jet Plume.

Table 2. Jet Parameters[a]

For the following shock parameters:

$T_5 = 2100°$ K

$M_{incident} = 3$

$P_1 = 10$ torr

$\rho_5 = 3.6 \times 10^{-6}$ moles/cm^3

$D_{orifice} = 0.005$ cm

these argon jet parameters are found:

$X_M = 51.4$ cm

$X_B = 32.4$ cm

$D_M = 19.5$ cm

$D_B = 23.6$ cm

$\delta_{centerline} = 5.5 \times 10^{-10}$ moles/cm^3

$M_{terminal} = 5.39$

$P_{centerline}$ (at M = 5.39) $= 6.8 \times 10^{-3}$ torr

X_{jet} (at M = 5.39) $= 1.09 \times 10^{-2}$ cm

Jet start-up time at sampling position = 14.6 sec

$\dot{m}_{max}$ for viscous flow $= 2.72 \times 10^{-6}$ moles/sec

---

[a] T_5 is the reflected shock temperature
M_5 refers to Mach number, P is pressure, ρ is density
The subscripts 1,2,5 refer to shock regions as noted on the wave diagram, Figure 1.

The listed jet parameters were found by the following equations.[4,5]

a) $X_M = \frac{X_M}{D} D = 0.67 \left(\frac{P_0}{P_+}\right)^{1/2} D$

D = diameter of orifice

$P_0 = P_5 = \rho_5 RT$

$P_+ = P_{\text{Mass-Spectrometer Chamber}} = 2 \times 10^{-6}$ torr

b) $X_B = 0.63\ X_M$

c) $D_M = 0.38\ X_M$

d) $D_B = 1.21\ D_M$

e) $\rho_{\text{centerline}} = 0.018 \left(\frac{\gamma^2}{\gamma-1}\right)^{\frac{1}{\gamma-1}} \left(\frac{D}{X}\right)^2 \rho_5$

$\gamma = 1.67$

$X = 0.063"$

f) $M_{\text{Terminal}} = 1.17\ Kn^{-.4}$

Kn = Knudsen # $= \frac{1}{\pi n \sigma^2 D} = 0.022$ for the shock parameters listed in Table 2

n = number density upstream of orifice = $\rho_5 \times$ Avogardro's No.

σ = diameter of argon = 3.66×10^{-8} cm.

D = orifice diameter = 0.005 cm.

g) $P_{\text{centerline}} = \text{centerline}\ R\ T_{jet}$ (at Mach # = 5.39)

$\left(\frac{T_{jet}}{T_5}\right)^{1/2} = \left(1 + \frac{\gamma-1}{2} M^2\right)^{-1/2}$

M = terminal Mach # = 5.39

$T_{jet} = 198.6°K$ at $M = 5.39$

h) Jet rise time, Δt_{jet} (also called start-up time)

$$\Delta t_{jet} = 0.794 \frac{D}{a_5} \left(\frac{X}{D}\right)^{5/3}$$

a_5 = sound speed in the reflected shock region = $\left(\frac{\gamma R T_5}{M.W.}\right)^{1/2}$

X = sampling position of the jet by electron beam = 0.063"

i) $\dot{m}_{max}$(viscous flow) = $0.8 \left(\frac{2}{\gamma-1}\right)^{\frac{\gamma+1}{2(\gamma-1)}} \rho_5 \frac{\pi D^2}{4} a_5$

froze, that is it remainded unchanged with increasing distance from the orifice. The perpendicular distribution in a transitional free jet became increasingly narrow with distance from the orifice. This latter finding was in contrast to the case of effusive flow where the perpendicular distribution also freezes in that flow regime.

C. The Coupled Shock Tube/Mass-Spectrometer Technique

Bradley and Kistiakowsky[6] performed the first studies of reaction kinetics using both a shock tube and a mass spectrometer. This technique, called the coupled shock tube/mass spectrometer technique has since been used by other gas kineticists. Some have used the time-of-flight (T.O.F.) mass spectrometer to scan the spectra of several chemical species[6-14]; others have chosen the quadrupole mass spectrometer to monitor the concentration of a single species.[15,20,28] A typical experimental set-up is shown in Figure 3.

The use of spectroscopic methods such as chemiluminescent emission or absorption to monitor concentration are well established techniques in shock tube work[16]; the development of the coupled shock tube-mass spectrometer method provided the experimentalist with another technique to obtain kinetic parameters from shock tube experiments. When used in conjunction with shock-heating of a gas sample, both the spectroscopic and mass

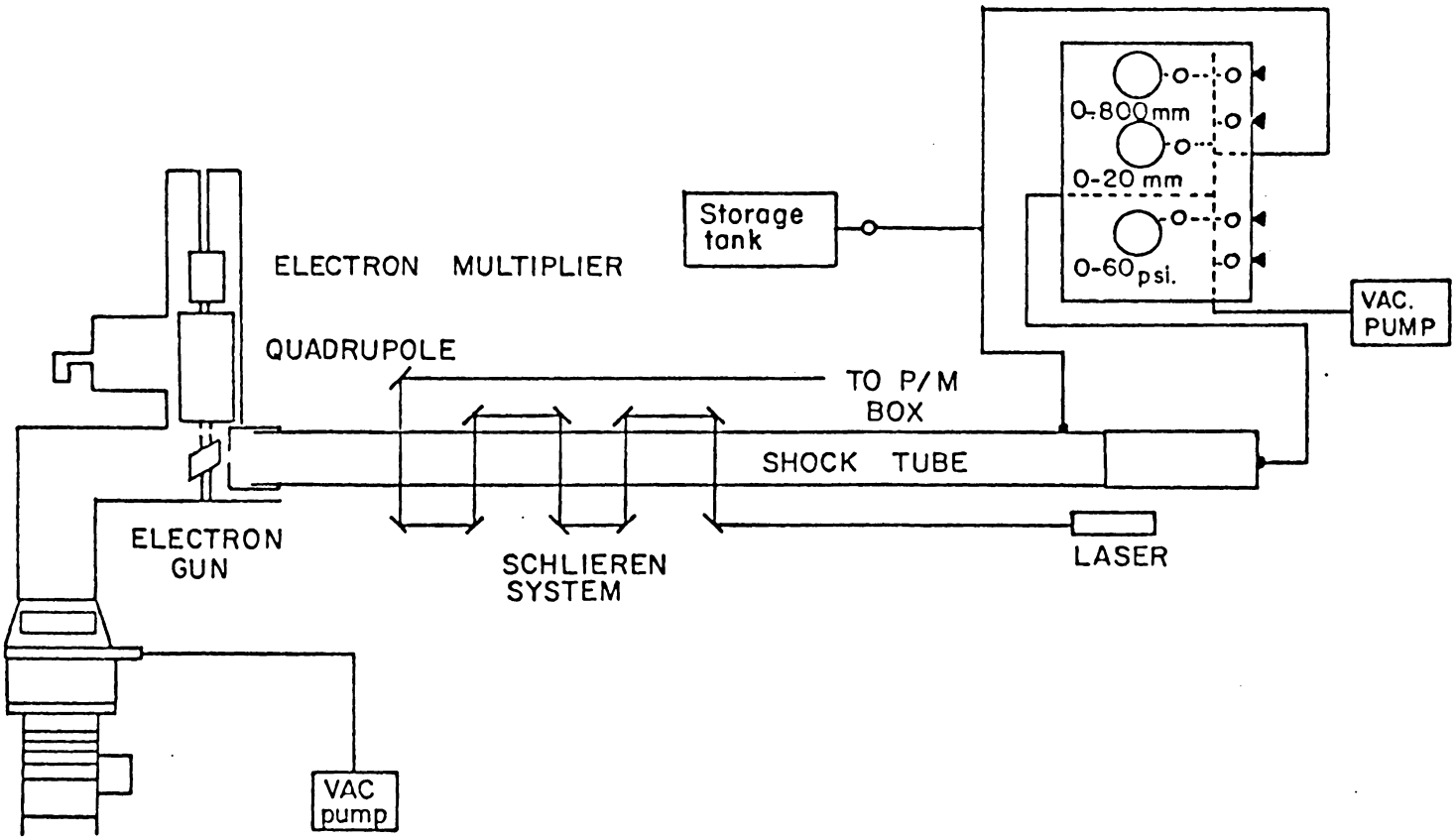

Figure 3. Coupled Shock Tube - Mass Spectrometer Experimental Set-up.

spectrometric techniques have their inherent difficulties which limit the accuracy of the kinetic data. In both spectroscopic and mass-spectrometric work, calculating correct gas temperatures is crucial for obtaining meaningful rate constants (from concentration data) and Arrhenius activiation energies from the equation $k(T) = Ae^{-Ea/RT}$. In both techniques, "ideal" temperatures are calculated from the Rankine-Hugoniot relations.[16] The Rankine-Hugoniot equations, Table 3, are valid for gases with a constant heat capacity. However, chemical reaction makes the heat capacity C_p temperature-dependent. There may also be contributions to C_p from excited vibrational and rotational degrees of freedom. In the Rankine-Huboniot equations, the calculated temperature is a function of $\gamma = C_p/C_v$. The use of a constant C_p is therefore an oversimplification which causes the "ideal" calculations to be in error (lower limit: $\pm$1% for a monatomic gas).[17] However, these equations have been corrected for temperature effects and reaction enthalpies in treating real polyatomic gases.[16]

Spectroscopic work has been the standard experimental method of obtaining rate data. Here, the growth of a velocity boundary layer (a layer of cold, dense gas forming next to the shock tube walls) creates additional problems in obtaining accurate gas temperatures. Consequently, concentration data from spectroscopic experiments can be inaccurate. In Figure 4, the velocity boundary

Table 3. Rankine-Hugoniot (conservation) Equations*

1. Conservation of mass: $\rho_1(u_{shock}-v_1) = \rho_2(u_{shock}-v_2)$

2. Conservation of momentum: $\rho_1(u_{shock}-v_1)^2 + p_1 = \rho_2(u_{shock}-v_2) + p_2$

3. Conservation of energy: $h_1[(u_{shock}-v_1)^2/2] = h_2[(u_{shock}-v_2)^2/2]$

these are combined with:

4. ideal gas law: $p_1 = (\rho_1 RT_1/MW_1)$

5. ideal gas law: $p_2 = (\rho_2 RT_2/MW_2)$

6. calorically perfect gas law: $h_2 - h_1 = c_p(T_2-T_1)$

and

known variables: v_1, p_1, ρ_1, T_1, h_1; u_{shock} by experiment.

One can therefore use six equations to get five unknown variables:

v_2, p_2, ρ_2, T_2, h_2.

*Here, v = particle velocity, lab coordinates, p = pressure, ρ = density, T = °K, h = enthalpy/mass, u = shock wave velocity, lab coordinates, MW = molecular weight.

The subscripts 1 and 2 refer to initial and incident shock conditions respectively, as discussed in section A.

layer which has formed around the core of hot shocked gas is idealized by a ring of gas labeled "cold". In reality, note that there is a temperature gradient from the shock tube wall to the hot free-steam gas. For absorption experiments in which there are no boundary layers (see case a), $A_{observed} = \varepsilon(T_{hot})(2b)c$, where A is absorptivity, ε is the absorption coefficient, 2b is the path length, and c is the concentration. Here the problem in obtaining accurate concentrations arises because the temperature-dependence of the absorption coefficients is not well known for most molecules. Also, the concentration and gas density is different in the hot and cold regions. Most shock tube experiments are carried out over a wide range of temperatures, but, generally, a representative ε is used. Ideally, a shot-by-shot value of ε would be desired. In case b, it can be seen that the velocity boundary layer introduces three additional unknowns, T_{cold}, b_2, and c_2 into Beer's Law. The observed absorbance is a complicated function of unknowns b_1, b_2, and T_{cold}; however, the average concentration $c'_{average}$ is calculated from $A_{observed} = \varepsilon(T_{ideal})2bc'_{average}$, which is sufficiently accurate if $\varepsilon(T)$ is not strongly temperature-dependent. The ideal temperature, T_{ideal}, is corrected for possible boundary layer effects.

In emission studies, chemiluminescence is observed from the hot gas only. One generally obtains concentration data in the following way. From the order of reaction, initial concentration

of reactant, and from the history of the decay (or growth) of the chemiluminescence one can obtain intermediate concentrations without having to use the Einstein coefficients.[21] Therefore, temperature corrections to emission intensities caused by the velocity boundary layer are avoided. However, the T_5 of the bulk gas should be corrected; the corrections to the idea gas temperatures T_2 and T_5 due to boundary layer growth and deceleration of the incident shock wave can be found in Trafton's thesis.[21] Also, the cold gas can absorb some of the emission.

It should be noted that similar reasoning applies to the calculation of gas densities; here, also, "ideal" densities are obtained from the Rankine-Hugoniot equations and are functions of γ. The velocity boundary layer gas is denser than the hot free-stream gas, and this causes deviations from calculated ideal values.

In addition to the problems introduced with the formation of a velocity boundary layer on the side walls of the shock tube, any sampling done at the endwall of the shock tube is further complicated by the fact that a stationary layer of cold gas (a thermal boundary layer) forms at the endwall. The mass spectrometer almost invariably has been used to sample reactions at the endwall of the shock tube. The formation of an endwall thermal boundary layer can affect the reflected shock temperature. Goldsworthy,[18] for

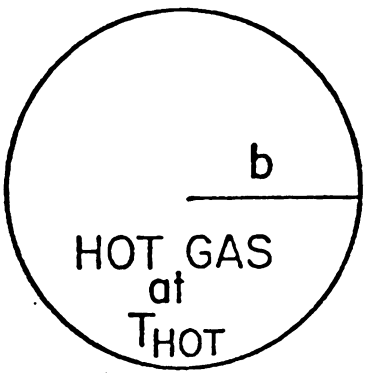

Case (a) no velocity boundary layer.

$A_{observed} = \epsilon(T_{Hot})(2b)c.$

In practice, we find a value ϵ at some representative T from spectroscoptic data.

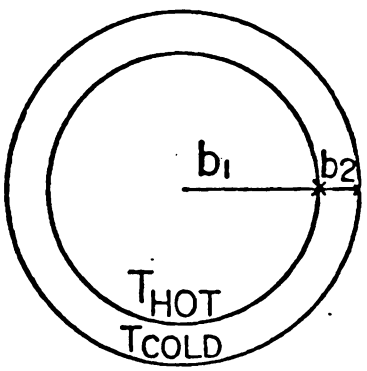

Case (b) simplified boundary layer at one temperature, T_{cold}; b_2 is thin compared to b_1.

$A_{Hot} = \epsilon(T_{Hot})(2b_1)c_1$

$A_{Cold} = \epsilon(T_{Cold})(2b_2)c_2$

where c_1, c_2 are concentrations of the reactant in hot and cold gas, respectively.

However, in practice, we calculate concentrations from $A_{observed} = \epsilon(T_{ideal})2(b_1+b_2)c'_{ave}$, where T_{ideal} is the calculated shocked gas temperature from the Rankine-Hugoniot relations, corrected for velocity boundary layer effects,[21], and c'_{ave} is the calculated concentration.

Figure 4. Velocity Boundary Layer Problems in Spectroscopic Experiments.

example, has shown that because of the thermal boundary layer, the reflected shock velocity may be slightly less than expected from the ideal reflection of the incident shock. However, the thermal boundary layer may present far more significant problems with respect to faithful sampling of the shock tube reaction mixture.

A summary of the errors present in both spectroscopic and mass-spectrometric techniques is presented in Table 4.

It is interesting to compare rate data obtained by both techniques on the same reaction. Table 5 lists some of these experiments. For the N_2O unimolecular decomposition, there is a wide range of values for the activation energy when data obtained by both techniques are compared. However, in the two examples (experiments 3 and 4) where the mass-spectrometric data do not agree with the spectroscopic result, the mass-spectrometric activation energy appears to be lower. The differences in the activation energy values for the N_2O reaction cannot be attributed to the different collision efficiencies of the various third bodies used in these experiments.[12] With the exception of the Bradley-Kistiakowsky study, the mole fraction of reactant in the N_2O experiments was kept small to avoid complications created by endo- or exothermicity; therefore, any discrepancies between the spectroscopic and mass-spectrometric experiments are not due to enthalpy effects. A likely possibility is that an experimental

Table 4. Summary of Problems Involved in Spectroscopic and Mass-Spectrometric Reflected Shock Studies

Problems common to both techniques

1. Errors in the calculation of ideal gas temperatures and densities from the Rankine-Hugoniot equations when chemical reaction causes severe deviations from thermal equilibrium.
2. Errors in the determination of u_5, the reflected shock velocity. Therefore, the temperature of the hot shock-treated gas may show additional deviations from the ideal value.

Problems unique in spectroscopic work

1. Errors in temperature and density calculations due to velocity boundary layer effects. These effects are amplified in reflected shock work.
2. Difficulties in determining the temperature dependence of absorption coefficients in absorption studies.

Problems unique in mass-spectrometric work

1. Inaccuracies in sampling due to the formation of the thermal boundary layer.

artifact introduced by the mass-spectrometric technique is responsible for the observed trend. However, it should be noted that the differences between the spectroscopic results are in themselves large, and so the mass-spectroscopic results are within the range of the spectroscopic measurements.

When other reactions are considered, we see that the mass-spectrometric and spectroscopic data agree, except for the one piece of mass-spectrometric data on the COS reaction. Here the mass-spectrometric result is high; the spectroscopic value for the experiment was obtained on the same shock tube.[21,22]

It seems that there are insufficient data to fully assess the validity of the mass-spectrometric technique on the basis of the few experiments performed with both techniques. However, there is other available evidence for the effects of the boundary layer (both thermal and velocity boundary layers[20]) on shock tube data from single pulse studies.[54,55,56]

In these experiments, samples of gas quenched by the expansion wave after reflected shock heating are withdrawn from the end of the test section and analyzed. Consequently, if colder gas from the boundary layer is withdrawn along with gas which was heated to T_5 before quenching, the accuracy of rate constants could be affected.

The single pulse sampling studies may have implications for

shock tube/mass spectrometer experiments in which shocked gas samples could also be contaminated by the cooler boundary layer gas. In both the single pulse experiments and time-resolved shock tube mass-spectrometer studies, gas samples are withdrawn from the test section endwall. The typical size of single-pulse samples, however, is far larger than those used in jet sampling[a] of shock tube flows. Skinner[55] estimated that the length of sample in his studies was about 10 cm. Also, it is questionable whether the quenching of the gas in the single pulse technique is instantaneous. Therefore, apparent extents of reaction might in reality be too large so that the error imposed by sampling cool gas therefore would be overestimated. Nevertheless, it is interesting to note that the presence of boundary layer gas could, in part, account for rate constant errors in another sampling technique.

Skinner[54] indicated that the magnitude of the correction to the (single pulse) extents of reaction was a function of the size of sample withdrawn for analysis as well as a function of heating time and reaction temperature. (Both of these would, of course, affect the rate of product formation). He estimated typical errors to be on the order of 5-20% for small conversion rates. Another paper on the pyrolysis of ethylene[55] attempted to correct the observed

---

[a]A discussion of typical sample size used in the coupled technique is presented later. It is shown that the sampling hemisphere radius extends about 0.06 cm. from the endwall in Section D.

extents of reaction for wall cooling and more specifically to understand the influence of thermal boundary layer cooling on kinetic data using Goldworthy's equation.[18] Skinner calculated the conversion rates with wall cooling after reflected shock heating of the gas sample and also after both incident and reflected shock heating. These values ranged from 0.86 to 0.80 of the expected conversion rate if no cooling were present.

Lifshitz et al.[56] studied the lowering of conversion rates in a shock tube for the $C_4F_8 \rightarrow 2C_2F_4$ reaction. Hollow cylinders were inserted into the test section and soldered to the endplate. In this way, the surface area per unit volume of the test section was increased. Therefore, the chance of sampling cold gas (velocity, boundary layer gas) was increased, and reactive experiments with and without cylinders could be compared.

In calculating the chemical conversion rates of samples withdrawn near the endwall with no cylinders, only thermal boundary layer effects were considered to account for the cooling of shocked gas. It was calculated that conversion rates were affected by the thermal boundary layer only within 1 mm of the endwall. The good agreement between calculated and observed extents of reaction indicated that thermal boundary layer effects should be considered when gas close to the endwall is analyzed.

In experiments run with cylinders, the lowering of the extent of reaction was proportional to the surface/volume ratio of the

Table 5. Spectroscopic (S) versus Mass-Spectroscopic (MS) Rate Parameters for Some Shock Tube Experiments[19]

Reaction	Technique	Rate Parameter: Rate Constant (cm^3/mol-sec) and Activation Energy	Reference and Comments
$N_2O + M \rightarrow N_2 + O + M$	MS	2×10^8 - 2.3×10^9 cm^3/mol sec = $k_{2nd\ order}$ T = 1565°K - 1997°K E_a = 57,600 cal/mol	Bradley & Kistiakowsky, J.C.P.,[a] 35, 256 (1961). Reflected shock wave. M = Ar. 24% N_2O in Ar.[b] $[N_2O]$, $[O_2]$, [O], $[N_2]$ followed by TOF. 1/2" i.d. shock tube.
	MS	$1.8 \times 10^{14} \times e^{-26,400/T}$ T = 1870°K - 2370°k E_a = 52,800 cal/mol	Gay et al., J.C.P., 43, 1720, (1965). Reflected shock wave. M = Ne. 5% N_2O in Ne. $[N_2O]$ followed by TOF.
	MS	$(7.2 \pm 1.5)\ 10^{12}\ e^{-(+20,500 \pm 500/T)}$ T = 1800°K - 2800°K E_a = 41,000 cal/mol	Barton & Dove, Canad. J. Chem., 47, 521 (1969). Reflected shock wave. M = Kr. 2.1% N_2O in Kr. $[N_2O]$, $[N_2]$, $[O_2]$, [NO] followed by TOF.

[a] J.C.P. is J. Chem. Phys.

[b] all gas mixtures presented in this work are expressed as mole percentages

[c] J.C.P. is J. Phys. Chem.

Table 5, continued

Reaction	Technique	Rate Parameter: Rate Constant (cm^3/mol-sec) and Activation Energy	Reference and Comments
	MS	T = 2400°K - 3300°K E_a = 57,400 cal/mol	Modica, J.P.C.[c] 69, 2111 (1965). Reflected shock wave. M = Ar. [Ar][N_2O] followed by TOF [N_2O] = 5% Identical results for T_5 3000°K for nozzle and orifice technique. At high T_5's, orifice technique yields somewhat higher errors. 2.54" i.d. shock tube.
$N_2O + M \rightarrow N_2 + O + M$	MS	1.8×10^{13} $e^{-21,000/T}$ T = 1600°K - 2100°K E_a = 42,000 cal/mol	Clark et al., J.C.P., 52, 4692 (1970). M = Ne. Reflected shock. 1.1% N_2O in Ne. TOF.
	MS	1.2×10^{7} $T^{.5}$ $(30,000/T)^{5.09}$ $e^{-30,000/T}$ T = 1800°K-2500°K 1.7×10^{6} $T^{.5}$ $(30,000/T)^{5.84}$ $e^{-30,000/T}$ T = 2500°K-3500°K E_a = 60,000 cal/mol for both temperature ranges	Gutman, et al., J.P.C., 70, 1793 (1966). M = Ar. 4% N_2O in Ar [N_2O], [NO], [O] monitored by quadrupole.

Table 5, continued

Reaction	Technique	Rate Parameter; Rate Constant (cm^3/mol-sec) and Activation Energy	Reference and Comment
$N_2O + M \rightarrow N_2O + M$	S	$4.9 \times 10^{13} \; e^{-24,900/T}$ $T = 1900°K - 2200°K$ $E_a = 48,800$ cal/mol	Fishburne, et al., J.C.P., 41, 1297 (1964). M = Ar.
		$4.1 \times 10^{13} \; e^{-24,300/T}$ $T = 1500°K - 2150°K$ $E_a = 48,600$ cal/mol	M = O_2. Incident shock. $[N_2O]$ = 2%, monitored by i.r. emission. 3.5" i.d. shock tube.
	S	$10^{14.56} \; e^{-53,000/RT}$ $E_a = 53,100$ cal/mol	Trafton, W., Ph.D. Dissertation, University of Illinois, 1973. M = Ar. Incident shock. $[N_2O]$ = 1%, 2%, 0.5%. Boundary layer corrections applied, extrapolation to ∞ diameter.
	S	$5 \times 10^{14} \; e^{(-29,000/T)}$ $T = 1500°K-2500°K$ $E_a = 58,000$ cal/mol	Olschewski, et al., Ber. Bunsenges Physik. Chem., 70, 450 (1966). M = Ar. Reflected and incident shock. $[N_2O]$ = 0.02 - 1%. i.r. emission + UV absorption 3.2" i.d. shock tube.

Table 5, continued

Reaction	Technique	Rate Parameter: Rate Constant (cm^3/mol-sec) and Activation Energy	Reference and Comments
$N_2O + M \rightarrow$ $N_2O + M$	S	$1 \times 10^{15}\ e^{(-31,000)/T}$ T = 1750°K - 2500°K E_a = 62,000 cal/mol	Jost, et al., Z. Naturforschung, 19a, 59 (1964). M = Ar. $[N_2O]$ = 0.5% - 3% Reflected shock. $[N_2O]$ monitored by u.v. absorption.
$N_2O + M \rightarrow$ $N_2 + O + M$	S	$1.42 \times 10^{14}\ e^{(-51,000/RT)}$ E_a = 51,280 cal/mol	Monat, et al., Combust. Sci. and Technology, 16, 21 (1977). M = Ar, Kr. $[N_2O]$ = 0.7 - 2.7% $[N_2O]$ followed by i.r. emission.
	S	$3.25 \times 10^{-10}\ e^{-51,400/RT}$ T = 1950°K - 3075°K E_a = 51,400 cal/mol	Dean, A. Inst. J. Chem. Kinetics 8, 459 (1976). M = Ar. Reflected shock. $[N_2O]$ = 0.5%, 1.01%, 1.08% i.r. emission). 3" i.d. shock tube. Runs were also done in the presence of H_2 to analyze the contribution of $N_2O + O \rightarrow 2NO$ $N_2O + O \rightarrow N_2 + O_2$ to the N_2O dissociation mechanism. The reported E_a is the best value for all runs, with and without H_2.

Table 5, continued

Reaction	Technique	Rate Parameter : Rate Constant (cm^3/mol-sec) and Activation Energy	Reference and Comments
	S	$10^{-9.31 \pm 0.012}$ $e^{-52,366 \pm 1,200}$ T = 1800°K - 2535°K E_a = 52,366 ± 1200 cal/mol	Baber, S.C. and Dean, A., Int. J. Chem. Kinetics 7, 381 (1975). M = Ar. Reflected shock. [N_2O] = 0.5%, 1.01% without added CO (i.r. + UV emission) 1.02% + 0.5% CO, 1.05% + 1.03% CO, 1.01% + 2.11% CO (u.v. emission) Addition of CO had no effect on the kinetics of N_2O.
$N_2O + M \rightarrow N_2 + O + M$	S	3.6×10^{14} $e^{-28,600/T}$ T = 1165°K - 1920°K E_a = 57,200 cal/mol	Drummond, et al., Aust. J. Chem., 20, 815 (1967). M = Ar. Reflected shock. [N_2O] = 6%. u.v. absorption. Rectangular shock tube, 3.75" hydraulic diameter.
$N_2O + M \rightarrow N_2 + O + M$	single[b] pulse	$10^{13.1}$ $e^{-44100/RT}$ T = 1300°K - 1950°K E_a = 44,100 cal/mol	Lipkea, et al. Combust. Sci. and Technol. 6, 257 (1973). M = Kr. Reflected shock.

[b] Lipkea's experimental data is included here as an additional piece of information on the N_2O reaction by another technique. The E_a of 44.1 Kcal/mol is within the range of the spectroscopic results

Table 5, continued

Reaction	Technique	Rate Parameters: Rate Constant (cm^3/mol-sec) and Activation Energy	Reference and-Comments
			N_2O, NO, O_2, N_2 analyzed by gas chromatography. i" i.d. shock tube.
N_2H_4 + M → $2NH_2$ + M	MS	2.4×10^9 - 1.0×10^{10} = $k_{(2nd\ order)}$	Diesen, J.C.P., 39, 2121 (1963). M = Ar. 0.5 - 1% N_2H_4.
	S	1.7×10^9 - 7.7×10^9 = $k_{(2nd\ order)}$ T = 1390°K - 1570°K	Meyer, et al.' 12th Combust. Symp., 345 (1969).
M + COS → CO + S + M	S	$10^{14.2}$ $e^{-(61,000/RT)}$ T = 1500°K - 3100°K E_a = 61,000 cal/mol	Schrecker and Wagner, Int. J. Chem. Kin., 1, 541 (1969). i.r. emission from COS. u.v. absorption of S_2. 3.2" and 2.8" i.d. shock tube.
M + COS → CO + S + M	S	$10^{14.92}$ $e^{-(63,000) \pm 1300)/RT}$ E_a = 63,000 cal/mol ± 1300	Trafton, W., Ph.D. Dissertation, University of Illinois, 1973. [COS] = 0.4%. No boundary layer; corrections due to velocity measurement problems. 2.9" i.d. shock tube.

Table 5, continued

Reaction	Technique	Rate Parameters: Rate Constant (cm^3/mol-sec) and Activation Energy	Reference and Comments
M + COS → CO + S + M	MS	$1.3 \times 10^{10}\ T^{.5}\ (76{,}000/RT)^{2.94}\ e^{-76{,}000/RT}$ T = 2000°K - 3200°K E_a = 76,000 cal/mol	Hay, A., Ph.D. Dissertation, University of Illinois, 1966. [COS] = 0.5%.
HCl + D_2 → DCl + HD	S	$10^{16.45 \pm 0.47}\ e^{-36.31 \pm 4.90/RT}$ cm^3/mol sec T = 1700°K - 2800°K E_a = 36,310 ± 4900 cal/mol	Kern, R.D. and Nika, G., J.P.C., 75, 176 (1971). M = Ar, Ne reflected shock. 1.50" i.d. shock tube. [HCl] monitored by i.r. emission.
HCl + D_2 → DCl + HD	MS	$10^{16.03 \pm 0.42}\ e^{(-33.95 \pm 4.40)/RT}$ E_a = 33,950 ± 4400 cal/mol	Kern, R.D. and Nika, G., J.P.C., 75, 176 (1971). [HCl], [D_2] = 2%. [DCl], [HCl], followed by TOF.
2 HCN + D_2 → 2 DCN + H_2	S	$10^{22.58 \pm .28}\ e^{(-54.84 \pm 3.05)/RT}$ T = 2000°K - 3000°K E_a = 54,840 ± 3050 cal/mol	Brupbacher, J.M. and Kern, R.D., J.P.C., 76, 285 (1972). [HCN], [DCN] followed by i.r. emission.
2 HCN + D_2 → 2 DCN + H_2	MS	$10^{22.07 \pm .29}\ e^{(-49.53 \pm 3.04)/RT}$ E_a = 49,530 ± 3040 cal/mol	Brupbacher, J.M. and Kern, R.D., J.P.C., 76, 285 (1972).

Table 5, continued

Reaction	Technique	Rate Parameters: Rate Constant (cm^3/mol-sec) and Activation Energy	Reference and Comments
			M = Ar. [HCN], [DCN], followed by TOF. [HCN], $[D_2]$ = 2%
$C_2N_2 + H_2 \rightarrow$ 2 HCN	S	$10^{25.29 \pm 0.23}$ $e^{(-65.72 \pm 5.38)/RT}$ cm^3/mol-sec $[M]^{-.75}$ T = 1850°K - 2650°K E_a = 65,750 ± 5380 cal/mol	Brupbacher, J.M. and Kern, R.D., J.P.C., 77, 1329 (1973). i.r. emission from HCN.
$C_2N_2 + H_2 \rightarrow$ 2 HCN	MS	$10^{25.29 \pm .023}$ $e^{(-61.02 \pm 2.29)/RT}$ E_a = 61.020 ± 2270 cal/mol	Brupbacher, J.M. and Kern, R.D., J.P.C., 77, 1329 (1973). [HCN], $[C_2N_2]$ followed by TOF. M = Ar, Ne $[C_2N_2]$, $[H_2]$ = 2%.
2 HBr + $D_2 \rightarrow$ 2 DBr + H_2	S	$10^{22.31 \pm 0.048}$ $e^{(-83,020 \pm 4970)/RT}$ E_a = 83,020 ± 4970 cal/mol	Kern, R.D. and Nika, G., J.P.C., 78, 2549 (1974). i.r. emission from HBr, DBr. $[D_2]$, [HBr] = 1.5%, 3%.

Table 5, continued

Reaction	Technique	Rate Parameters: Rate Constant (cm^3/mol-sec) and Activation Energy	Reference and Comments
$2\ HBr + D_2 \rightarrow 2\ DBr + H_2$	MS	[both experiments, S and MS, on this reaction yielded the same rate parameters]	Kern, R.D. and Nika, G., J.P.C., 78, 2549 (1974). 2% = [HBr], [D_2]. [$Br]_{79}$, [$Br]_{81}$, [HBr], [DBr] monitored by TOF.
$H_2 + CO_2 \rightarrow CO + H_2O$ $D_2 + CO_2 \rightarrow CO + D_2O$	S,MS	$10^{20.0 \pm 0.02}\ e^{(-81.4 \pm 2.3)/RT}$ cm^3/mol-sec E_a = 81,400 ± 2300 cal/mol	Brupbacher, J., et al., J.P.C., 80, 1031 (1976). M = Ar. [CO_2][D_2] = 2 - 10% [CO_2] = 1 - 5%, also. [D_2O], [CO_2] by i.r. emission. [H_2] - 10%.

test section. This indicated that velocity boundary layer (v.b.l.) effects could likely cause substantial problems in small diameter tubes (diameters of cylinders were 12.2-43.1 mm), particularly at low gas densities where the v.b.l. would be thicker and could be sampled.

In experiments performed with the coupled technique, a very small amount of gas near the endwall was sampled. The thermal boundary layer is considered to be the source of the colder gas which could contaminate the shocked gas sample. A further discussion of thermal boundary layer effects is presented in Section D.

D. The Effect of the Thermal Boundary Layer on the Sampling of Shock Tube Flows.

The thermal boundary layer which grows on the shock tube endwall is a thin layer of cold gas resulting from forced convection of the heated, shocked gas against the cold endwall. The formation of the thermal boundary layer depends upon the properties of the velocity boundary layer. For example, the thickness of the velocity boundary layer and whether it is laminar or turbulent will influence the temperature variation in the thermal boundary layer.[23] In the coupled technique, shock-heated gas flows from the orifice into the mass-spectrometer and the possibility of sampling some of this colder gas exists. It is expected that the cooling of the gas by the thermal boundary layer creates the major problem in the

sampling process using this technique. It seems likely that the velocity boundary layer does not play a direct role in causing deviations from the reflected gas temperature for sampling of orifice flows. A simple calculation shown here, indicates that only gas very close to the endwall becomes part of the jet flow, and this result is incorporated into a postulated model (see Figure 5) to explain the effects of the thermal boundary upon sampling.

The loss of fluid from the shock tube during a sampling period of time Δt can be found by considering the sink motion[45] through a small hole in a flat plate. For this type of motion, fluid moves in streamlines through a sampling hemisphere towards the hole (see Figure 6); the velocity of the fluid is proportional to $\frac{1}{r^2}$, according to the theoretical model. For viscous flow, the $\frac{\Delta mass}{\Delta time}$, maximum = $\dot{m}$ max, is approximately $\dot{m}_{max} \sim 0.8 \frac{2}{\gamma+1} \frac{\gamma+1}{2(\gamma-1)} \rho_5 \frac{D^2}{4} \left[\frac{\gamma R T_5}{M.W.}\right]^{\frac{1}{2}}$.

For typical experimental parameters, as indicated below,

$\dot{m}_{max} = 272 \times 10^{-8}$ mol/sec., $\rho_5 = 3.6 \times 10^{-6} \frac{mol}{cm^3}$, $T_5 = 2100°K$,

$D = 0.002"$, $M.W. = 40$.

The Δmoles lost during a test time, $\Delta t = 500$ μsec, is $\dot{m}_{max}\Delta t = 1360.5 \times 10^{-12}$mol which corresponds to a volume of $V_{lost} = \frac{\Delta mol}{\rho_5} = 377.9 \times 10^{-6}$ cm^3.

This volume would originally occupy a hemisphere of $V_{hemisphere} = \frac{2}{3} \pi r^3 = 377.9 \times 10^{-6}$ cm^3 and radius, $r = 5.7 \times 10^{-2}$ cm. Therefore, fluid within 0.06 cm of the endwall is sampled.

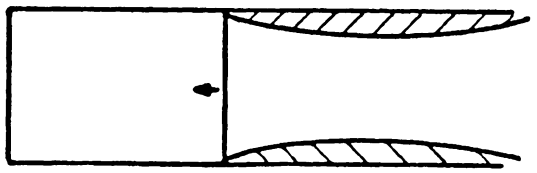

Formation of the incident shock velocity boundary layer.

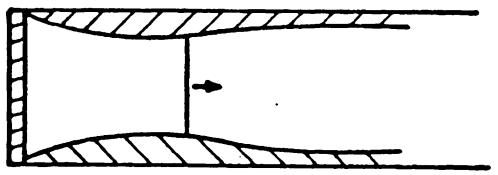

As the reflected shock moves back into the once-heated gas, there is additional thickening of the incident boundary layer due to thermal effects. The reflected shock brings the gas to rest; this additional thickness is not caused by viscous effects. A thermal boundary layer forms on the endwall.

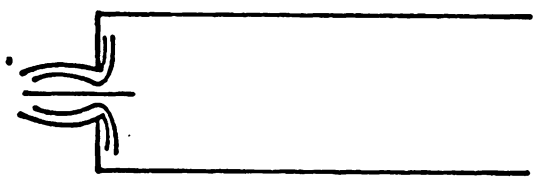

In sampling through the orifice, a very small volume of gas is lost. During the time of flow, the endwall boundary layer is sampled. In our experiment, $\sim$.76 cm^3/sec of gas is lost, $\frac{377.9 \times 10^{-6} cm^3}{500 \times 10^{-6} sec}$ (see text p.)

$T_5 > T_{\text{thermal boundary layer}}$ $\qquad$ $P_5 \simeq P_{\text{thermal boundary layer}}$

Figure 5. A Model for the Effects of the Thermal Boundary Layer on Sampling.

At the same time that the fluid is exiting through the orifice, a thermal boundary layer is growing on the endwall. It is clear from Figure 6 that for a given boundary layer thickness δ, off-axial streamlines experience thermal boundary layer cooling to a far greater extent than axial streamlines. A greater amount of cold gas is sampled as off-axial molecules approach the orifice. Furthermore, the effect of a larger orifice diameter (which increase $\dot{m}_{max}$) favors the sampling of a greater amount of shock-treated gas. Voldner[49] has treated these effects quantitatively in a theoretical study of fluid flow and heat transfer through the orifice.

Many of the experimentalists using the shock tube/mass-spectrometer technique were concerned that errors in kinetic parameters could possibly result from the sampling of cold thermal boundary layer gas along with the hotter shocked gas during kinetic runs. The colder gas has a smaller extent of reaction than the gas which was heated by the shock wave; consequently, the accuracy of rate constants which are based on mass-spectrometer analysis of colder gas could be questioned. These rate constants would be smaller than the rate constants based on measurements of concentration from gas which was shock-heated to the reflected temperature, T_5. (Note that T_5 would approach the ideal value for data obtained on large diameter shock tubes; in this instance, velocity boundary layer corrections[21,24] for the rate constant would be small. Most of the spectroscopic data shown previously in Table 5, was in fact,

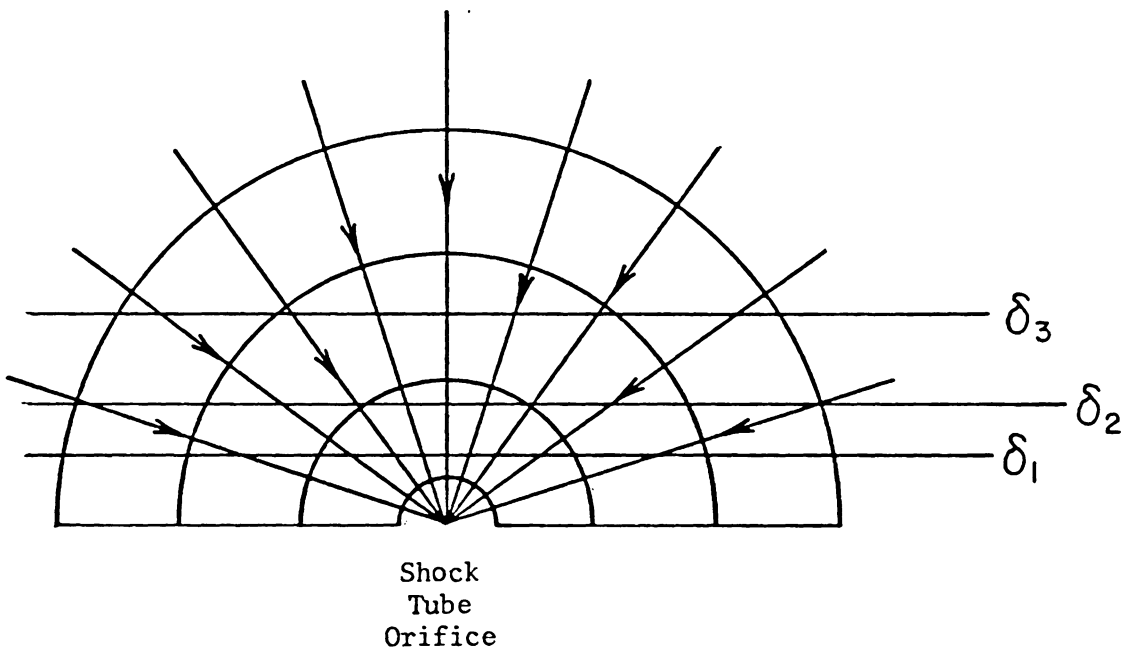

The sampling hemisphere represents the volume of gas which is sampled during the test time of the experiment. The fully grown hemisphere of radius r is shown. The development of the thermal boundary layer (t.b.l.) at arbitrary times t_1, t_2, t_3 and t_4 with boundary layer thicknesses of δ_1, δ_2, δ_3, δ_4 is shown. This illustration is a qualitative one only. As the radius of the sampling hemisphere grows by more and more gas feeding into the orifice, the thermal boundary layer is also expanding. They grow with different time dependencies[57]; $r \propto t^{1/3}$, $\delta_{t.b.l.} \propto t^{1/2}$.

Figure 6. Sampling Hemisphere.

obtained with large diameter shock tubes.) In mass spectrometer experiments in which faithful sampling of the hot gas was not maintained, rate constants lower than their true values would be expected.

Bradley and Kistiakowsky[6] maintained that only about 3% of the flow from their shock tube was from the cold thermal boundary layer, and that hydrodynamic flow from the orifice into the shock tube eliminated most of the endwall effects. Dove and Moulton[25] calculated the radius of a hemisphere of gas leaking from the orifice during the time of sampling after the arrival of the reflected shock wave. They concluded that the growth of a laminar thermal boundary layer during a time interval of <1 msec after shock arrival could ruin the accuracy of the sampling process. Modica[12] performed experiments on the decomposition of N_2O (2400-3300° K) using both a pinhole orifice and a pyrex nozzle protruding into the reflected shock region shock tube into a T.O.F. mass spectrometer. He found that the orifice technique yielded lower rate constants than sampling through a nozzle at temperatures above 3000° K. The nozzle sampled gas mainly from the bulk, and so the systematic error in rate constant introduced by orifice sampling was attributed to thermal boundary layer gas. The error was less for the nozzle technique. Gutman et al.[15] maintained that the effect of thermal boundary layer cooling on N_2O decomposition at temperatures > 2500° K needed further examination. Wang[26] presented a theoretical model to simulate the problems of sampling from a high-

pressure/high-temperature region (the reflected shock region) into a low pressure region (the mass spectrometer). He concluded that these preliminary studies indicate the need for further experimental work.

The objectives and goals of our investigation were to set up a coupled shock tube-mass-spectrometer apparatus, to test its design, and to perform a series of experiments to analyze the characteristics and capabilities of our apparatus. These experiments are fully described in the experimental section of this work, page 77. Additionally, on the basis of these characterization studies, we hoped to conclude our work, if possible, with the following jet scanning study.

Since the apparatus was basically a copy of the set-up used initially by Gutman, we decided to design an experiment which would be an extension of his earlier N_2O work. The proposed experiment would probe the contribution of the thermal boundary layer to the jet structure and relate the kinetic parameters so obtained to the sampling process itself.

Gutman[15,28] had used an electron beam to ionize in bulk a sample of gas from an entire cross sectional plane of the jet. Therefore, gas from the core, as well as gas from the outer regions of the jet (where thermal boundary layer effects might be expected) was analyzed simultaneously by the quadrupole mass spectrometer. There was no selective analysis made of gas in any particular portion of

the jet face. Despite the method of bulk analysis, Gutman[15] obtained an activation energy of 60,000 cal/mole for the N_2O decomposition reaction; this is on the upper end of the range of values of E_a (see Table 5) obtained for the N_2O reaction. This result suggested that the contribution of cold thermal boundary layer gas to the jet was for all practical purposes negligible.

Our proposed study intended to probe the jet structure for the N_2O reaction in greater detail. By using a very thin electron beam to selectively ionize portions of gas transversing a cross-sectional plane of the jet, we hoped to obtain rate constants and activation energies (for the N_2O unimolecular decomposition) which would yield a detailed composition profile of the jet. [More specifically, one would need to obtain only relative (rather than absolute) rate parameters in order to see any differences in activation energies (or rate constants) as the jet was scanned.] For scanning, we intended to move a thin electron beam through a cross-sectional plane of the jet close to the orifice both to minimize jet start-up time[4] and to maximize the signal to noise ratio of the mass peaks. The N_2O^+, O_2^+, and NO^+ peaks would be monitored for each scanning position of the beam. Consequently, an apparent activation energy for $N_2O + M \rightarrow N_2 + O + M$, the reaction of interest, would be obtained for each scanning position of the beam during the ionization process. (The monitoring of O_2^+ and NO^+ would be necessary to estimate the contribution of the two other reactions ($N_2O + O \rightarrow 2\ NO$;

$N_2O + O \rightarrow O_2 + N_2$) in the N_2O decomposition mechanism (see Section E).

In a typical shock tube experiment utilizing mass-spectrometric analysis of the gas flow through the orifice, the flow is expected to be laminar.[23,45] Therefore, without mixing of gas due to turbulence in the flow, the integrity of the flow features present in the shock tube at the time of heating would be preserved in the jet structure. It would be expected, in the absence of quenching, that the temperature gradient in a jet composed of both thermal boundary layer gas and a substantial amount of shocked gas (at T_5) would increase if one could probe gas temperatures from the jet edge onward to the jet core.

In a real experiment, all of the gas is at the same temperature after the jet expansion. Consequently, for the scanning study, one would experimentally obtain apparent activation energies or rate constants to measure the extent of reaction in specified portions of the jet. This in turn would provide an indirect probe of the temperature gradient formed in the gas sample while it was in the shock tube. This gas then took the form of a free jet as it exited from the shock tube. Reaction was quenched during the expansion process.

The observed trends in the distribution of apparent rate constants or activation energies obtained experimentally would give insight into the errors that might be expected in gas-phase experiments utilizing sampling of supersonic jet flow. For example,

a distribution of rate constants in which most of the values were low (and therefore most probably obtained from the ionization of thermal boundary layer gas) would indicate that the chance of sampling shock heated gas would be minimal for that particular set of experimental conditions. The proper choice of values of P_1, T_5 range, orifice size and shape, etc. would optimize the proportion of core gas that could be sampled in a specified shock tube experiment using the coupled technique. The jet scanning study would therefore provide additional insight into the validity of the coupled technique.

As we proceeded with our experiments and explored the characteristics of our apparatus, it became apparent that the capabilities of our apparatus were not yet adequate to perform the proposed study. (I wish to thank Professor J. Dove (University of Toronto) for consultations about the characteristics of the apparatus).

Accordingly, the results of this investigation, which will be outlined in detail in the experimental section, showed that dynamic ion signals with good signal to noise characteristics could be detected with our equipment and that non-reactive signals of proper shape could be obtained. Furthermore, our experiments have also suggested other modifications and improvements in equipment design which would be necessary for obtaining a detailed composition profile of the jet by the proposed scanning study.

E. The Thermal Decomposition of N_2O

Although the thermal decomposition of N_2O has been widely studied, there are still unsettled questions regarding the reaction mechanism. It is now accepted[19,21,28] that the major steps in the mechanism are:

1. $N_2O + M \rightarrow N_2 + O + M$ (pseudo-unimolecuular step)
2. $N_2O + O \rightarrow 2NO$
3. $N_2O + O \rightarrow N_2 + O_2$.

Here, M is an added inert gas molecule. However, the activation energy for reaction 1 is not firmly established (see Table 5). Moreover, the contribution of the two side reactions to the dissociation process (for various temperature ranges and N_2O concentrations of experimental interest) still creates problems in the analysis of kinetic data.

A review of the early (pre-1973) work on the dissociation has been discussed elsewhere[19,21,28] and therefore only the more recent literature will be presented here.

Lipkea[51] et al. attempted to study the thermal decomposition near the lower end (1300°K - 1950°K) of the temperature range studied by other investigators. They used a single pulse shock tube to heat dilute mixtures of N_2O in Kr, and analyzed the quenched samples of gas (N_2O, NO, N_2, O_2 were monitored) by gas chromatography. The overall rate of N_2O decomposition, as well as the rates of reaction 1, and the ratio k_3/k_2 were determined. They found that E_a for the unimolecular step was 44,100 cal/mole and that the average value of k_3/k_2 over

their temperature range of interest was 0.5 ± 0.016; the ratio was a slowly varying function of temperature. Moreover, their study substantiated the claim that the steady state assumption for 0 atom would be valid,[28] even at the lower temperature range of their study.

Baber and Dean[52] studied the dissocation of N_2O by monitoring infrared and ultraviolet emission. The thrust of this work was to explore some of the discrepancies in the rate data for the secondary reactions (2) and (3). In particular, a reliable value for k_2 was sought. Although earlier studies[19] showed that k_2 was about equal to k_3, the apparent rate constant $(k_{app})^a$ for the overall 3-step dissociation varied between k_1 and $2k_1$. The constant k_{app} would equal $2k_1$ only if a steady state concentration of 0 atoms maintained at the experimental conditions of interest. The experiments performed by Baber and Dean attempted to understand better what experimental parameters influenced the attainment of a steady state.

In addition, the N_2O dissociation was studied by adding CO to the N_2O-Ar mixtures.[b] The addition of CO to the N_2O system (which releases 0 atom) permitted the 0 atom concentration to be monitored by the ultraviolet (flame band) emission which is proportional to [CO][0]. The interesting finding in the CO studies was that the addition of CO to

---

[a] k_{app} was defined as $\left[\frac{-d \ln(IR)}{dt} / [M]\right]$ where (IR) is the infrared signal and [M] is the total gas concentration.

[b] The two reactions of CO in this mechanism are thought to be:

4. $CO + N_2O \rightarrow CO_2 + N_2$ 5. $CO + 0 \rightarrow CO_2 + M$

the N_2O mixture (1% N_2O) had no effect on k_{app} at 1850-2535°K. However, the observed levels of flame band emission increased in a time period similar to that of the N_2O decay. Furthermore, a comparison of the kinetic data obtained from two sets of kinetic runs, performed at similar temperatures and $(N_2O]_{init.}$ but at different $[CO]_{init.}$ showed that similar O atom concentrations were found for both sets of kinetic runs. It was therefore concluded that the steady state approximation was not valid in this experimental system. The constant k_{app} could not be set equal to $2k_1$, but on the other hand, there was no evidence to believe the k_{app} was equal to k_1. In this latter case, reactions (2) and (3) are too slow to contribute to the kinetics.

Baber et al.[52] attempted to resolve this dilemma by calculating values of $\frac{k_1}{k_2+k_3}$ from observed values of k_{app} and reaction half-times. Oxygen atom concentration was calculated as a function of the extent of reaction. It was found that the ratios obtained by such computations were higher than any previously reported literature values. In the numerical treatment of the observed data, the calculated O atom concentrations were a function of the rate constant ratio. In order to determine if the high rate constant ratio they obtained yielded meaningful O atom concentrations, Baber, et al. decided to fit known values of k_1, k_2 and k_3 in the numerical treatment to obtain a good value of k_{app}. Then they compared their own experimentally obtained rate parameters to the computed parameters to check for consistency and to judge the reliability of their own results. The error bar

limits in the calculated 0 atom concentrations were set by employing the low value[28] of the ratio and the high value (found by Baber et al.[52]) in the error analysis. It was consequently determined that the their experimental conditions, a constant concentration of 0 atoms was reached for temperatures greater than 2050°K at times of 600 μsec. or less. The kinetic parameters obtained in their study are presented in Table 5.

Dean[53] repeated the N_2O dissociation in Ar (reflected shock) for a higher temperature range (1950-3075°K) than in the earlier (1975) study. In order to estimate the importance of the secondary reactions to the N_2O reaction mechanism, an additional set of reactions was explored:

6) $O + H_2 \rightarrow OH + H$

7) $H + N_2O \rightarrow N_2 + OH$

8) $O + OH \rightarrow O_2 + H.$

Small amounts of H_2 0.011% to 0.104%) were added to the N_2O-Ar mixtures $[N_2O]$ = (1.01% to 1.09%). In the presence of enough atomic oxygen from reaction 1, H atom is released and reacts with the N_2O. Another pathway for N_2O decomposition is created. Therefore, a comparison of similar experiments performed with and without added H_2 would provide a measure of the importance of reactions 2 and 3 to the N_2O reaction mechanism.

Dean found that an increase in the observed rate constant, k_{obs}, resulted from the addition of H_2. However, the discrepancies in the

existing literature on reactions (2) and (3) were not resolved by an analysis of the experimental data obtained in the N_2O-Ar-H_2 studies.

1) Dean attempted to simulate the observed increase in k_{obs} by choosing values of k_2 and k_3 ("high" and "low" values of each), as reported by Fenimore and Jones and Fishburne and Edse (see Table 5), respectively. It was found that the low values of k_2 and k_3 gave better agreement with the experimental observations, with adjusted values of k_6, k_7, k_8 from the literature. The use of the high values did not allow a reasonable choice of k_7 in the data treatment; the observed dependence of k_{obs} on temperature and H_2 concentration was also not reproduced.

2) However, in the reactions of N_2O performed without H_2 at low temperatures, Dean found experimentally that the observed overall rate constant, k_{obs} did not even approach the $2k_1$ limit. Under these conditions, one would have expected the secondary reactions to play a large role in the reaction mechanism. Numerical integration of the reactions (details not reported here) with use of the high values of $k_2 = k_3$ gave good agreement with k_{obs}. However, low values of $k_2 = k_3$ were needed to give good agreement between experimental and calculated O atom $t^{1/2}$ values. Overall, the low values were chosen as the preferred values for k_2 and k_3.

3) As an additional probe to check the consistency of experimental observations with calculated results, Dean performed other calculations using N_2O concentrations (0.02%, 0.2%, 1%) with various combinations of

low and high values of k_2 and k_3. The previous work of Olschewski, et al. (see Table 5) had shown that N_2O concentrations greater than 0.2% at temperatures above 2000°K would make $k_{obs} = 2k_1$. However, Dean could not adjust k_2 and k_3 to simulate k_{obs} at the above N_2O concentrations.

4) Dean noted other discrepancies between his study and the existing literature. One point of disagreement was with regard to the expected values of NO concentration one would monitor during the course of reaction.

Monat et al. (see Table 5) studied the N_2O decomposition (incident shock wave) over the temperature range 1815-3365°K. N_2O and NO were monitored; and contribution of $N_2O + O \rightarrow N_2 + O_2$ to the reaction scheme was ignored for the high temperature experiments. In addition, computations utilizing both literature[a] and observed values of k_1, k_2, and k_3 attempted to simulate the behavior of N_2O decay as predicted by theory. The determination of the rate constants was not noticeably affected by the use of different third bodies (M = Arc, Kr, Ne) in the experiments.

In particular, Dean's work on the N_2O reaction scheme has some important practical implications for our proposed experiment. Since the unimolecular step was the desired reaction we wished to study by

---

[a]Monat et al. indicate only that "best" literature values of $k_2 = k_3$ were used. If these are the values recommended by the University of Leeds[19], Monat's $k_2 = k_3$ would be the so-called "high" value used by Dean.

quadrupole, it would be essential to know which reaction species would be most valuable to monitor. The quadrupole is capable of analyzing only one species per spectral run. It would be helpful to know if one could choose a set of reaction conditions so that k_{app} would be equal to its k_1 limit; then only one species (for example, N_2O) need be mass-analyzed. The ability to monitor just one mass peak would eliminate our having to do duplicate sets of kinetic runs for each species of interest whenever a new electron beam scan position would be chosen. Dean's work indicates that the N_2O mechanism may be very sensitive to the experimental conditions chosen.

F. Criteria for the Selection of Mass-Spectrometer

The time-of-flight (T.O.F.) mass-spectrometer has been the most widely used instrument for performing mass analyses on shock tube flows. The T.O.F. mass-spectrometer allows for the rapid scanning of several mass peaks at once. This ability of the T.O.F. instrument to see several mass peaks, all of which were created at one time, is termed "time purity." Time purity is an advantage in kinetic studies where one may wish to monitor several reactants and/or products simultaneously.

The T.O.F. mass-spectrometer can therefore be used to obtain ratios of peak heights and, if desired, can be used with an internal standard to quantify amounts of material present as well as to calibrate mass number. However, one cannot use the T.O.F. instrument to monitor any one mass peak continuously in time, as there is a finite

(20-100 sec) scan period. For this application, the quadrupole instrument is the analyzer used.

The magnetic sector mass-spectrometer has many of the desirable features of the quadrupole; however, the prohibitive cost of most models and extremely high resolution characteristics (which are generally not needed in kinetic studies) have eliminated it as the instrument of choice in shock tube-mass spectrometer studies. A summary of the properties of the three mass analyzers is shown in Table 6.

Table 6. Mass-Spectrometer Properties

Instrument	T.O.F.	Quadrupole	Magnetic
Time Purity	yes	no	no
Continuous Sampling	no	yes	yes
Use of Internal Standard	yes	no	no
Signal-to-Noise Ratio	varies*	varies*	good

*Varies with the time period over which a spectrum is recorded. Fast scans tend to lower signal to noise ratios.

II. EQUIPMENT AND APPARATUS

A. The Shock Tube System

The 4" i.d. shock tube consists of an 18 foot long test section and a 5 foot driver section. The driver is made of Corgard reinforced glass (Corning); the test section is Pyrex conical pipe with an initial 2 foot long stainless steel section and a terminal foot long sleeve of aluminum which inserts into the mass-spectrometer chamber. A stainless steel endwall plate on the end of the sleeve is held in place by 13 flathead screws. A 0.002" diameter spinneret leak (Engelhard Industries, Incorporated) was epoxied (by using Torr-Seal) into the machined circular groove of the endwall. Electrical continuity between the leak and the endwall was provided by thin stripes of silver conducting paint. The spinneret allows gas to leak from the shock tube into the mass-spectrometer chamber. The test section is equipped with a Veeco 2.5" stainless bellows valve; the driver is pumped through a Veeco 1-5/16" bellows valve. The driver section rests on wheels and can be rolled back for insertion and removal of diaphragms.

The shock tube is coupled to the mass-spectrometer chamber which consists of a 6" i.d. ell, cross, and tee of Pyrex conical pipe. The chamber rests on wheels and can be rolled back for maintenance of the electron gun. The coupler between the shock tube and mass-spectrometer chamber is such that the alignment of the shock tube into the chamber

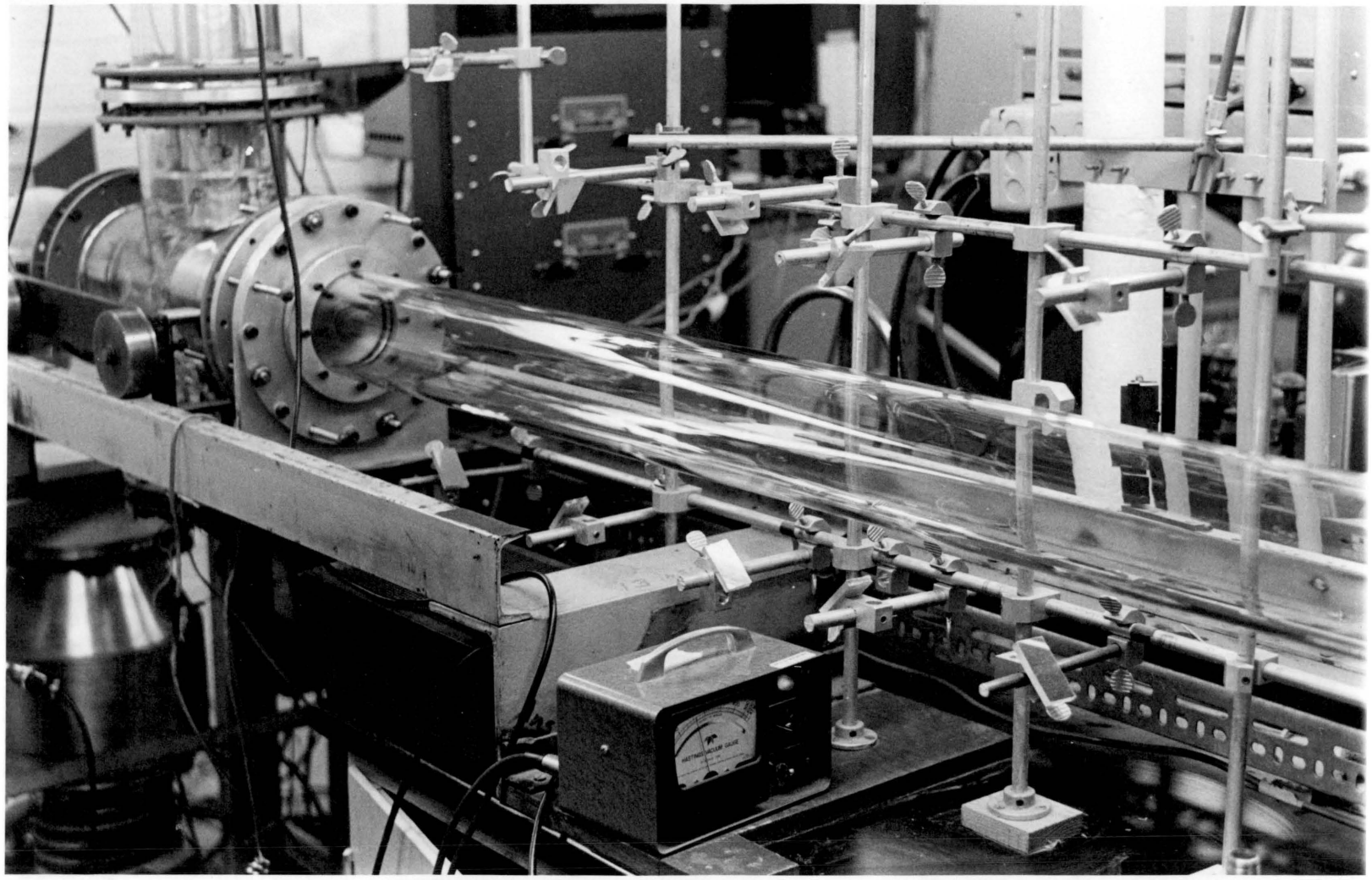

Figure 7. The Shock Tube (Test Section), Schlieren Mirrors, and the Mass-Spectrometer Chamber.

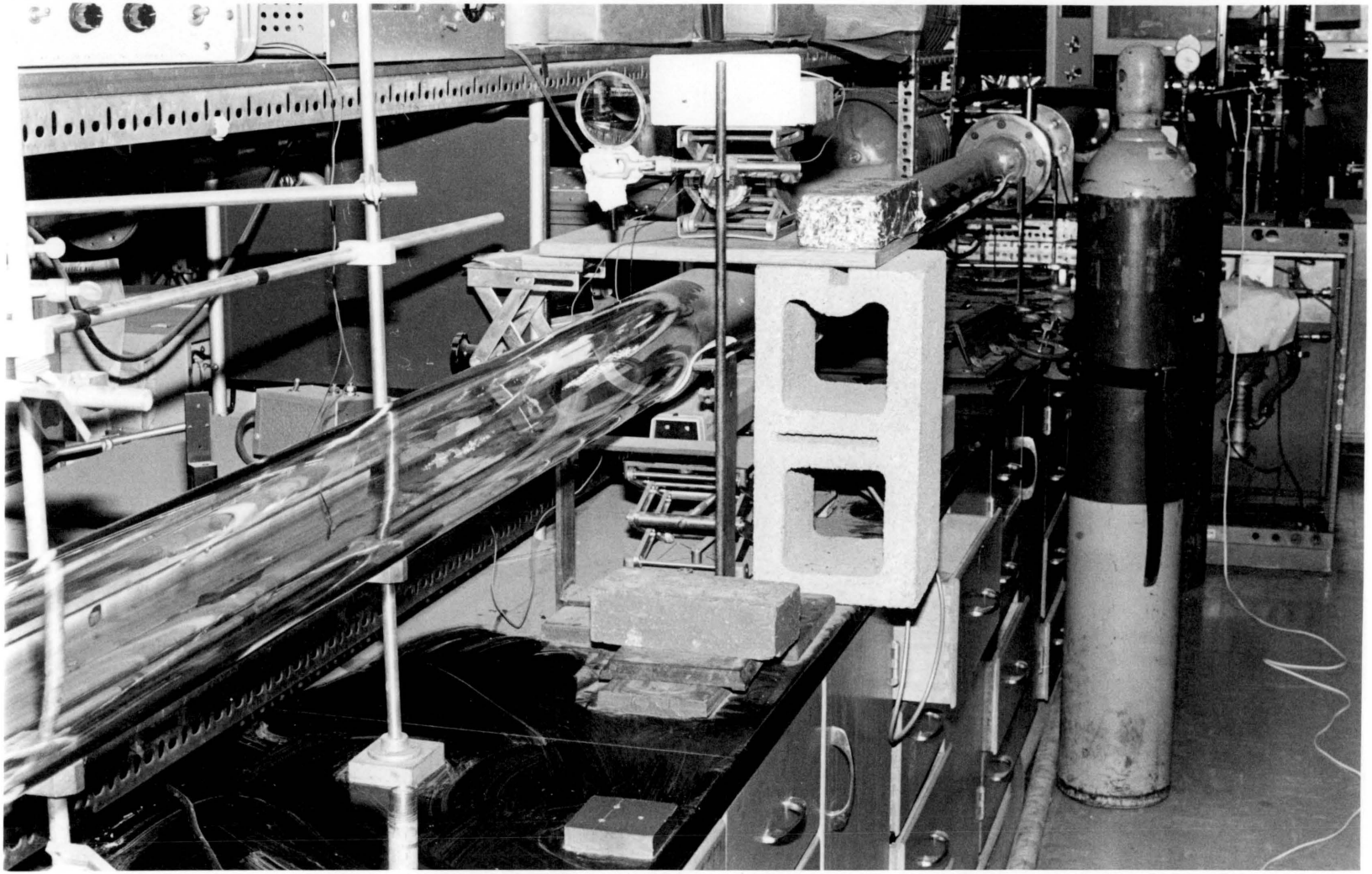

Figure 8. Shock Tube (Test and Driver Sections) with Laser and Photomultiplier Box.

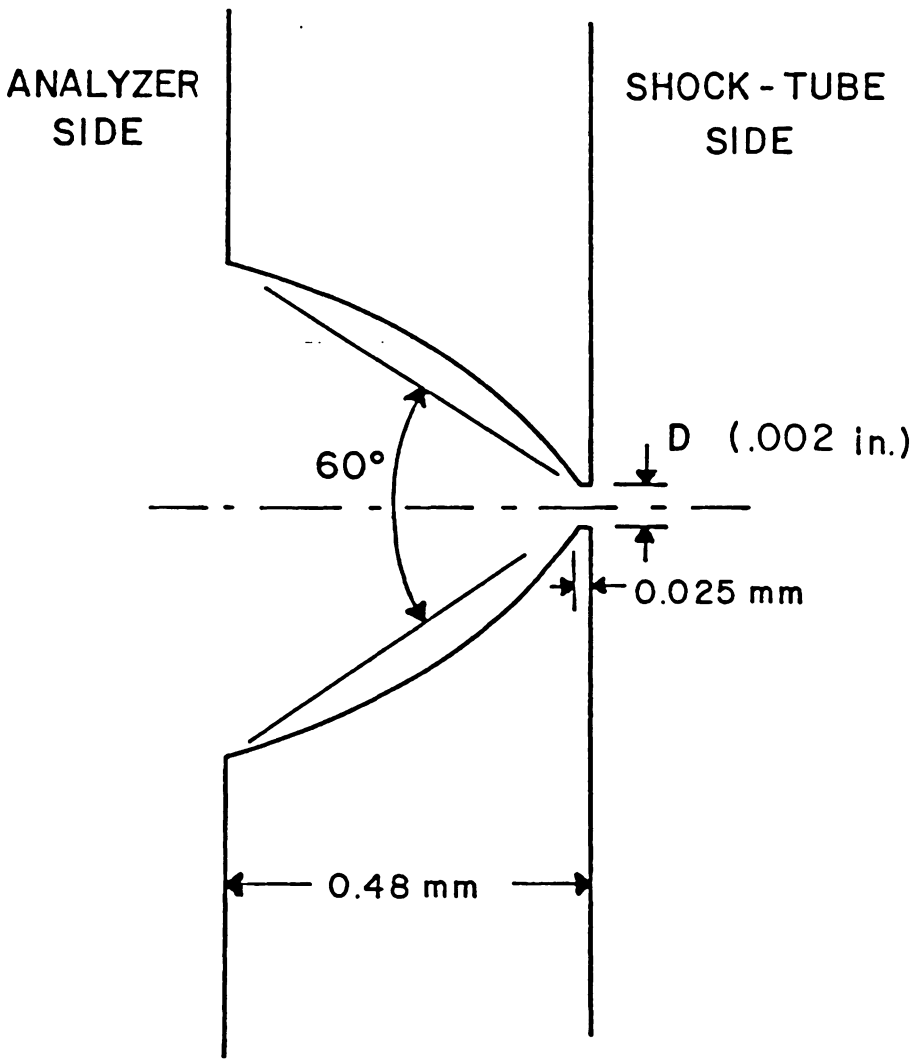

Figure 9. Detail of Spinneret Leak.

is preserved if the two sections are uncoupled and then rejoined. Therefore, the position of the spinneret leak with respect to the electron beam of the electron gun is maintained. The leak is slightly below the line defined by the electron beam.

B. Gas-Handling System

A portable rack consisting of a copper and stainless steel pumping manifold and three precision gauges allows the monitoring of gas pressures in the test and driver sections. These are shown schematically in Figure 3.

The manifold is a copper and stainless steel backbone; the stainless sections vary in diameter from 1/4" to 3/4", the copper section is 2" in diameter. A Jamesbury 2" gate valve and a Goddard 3/4" ball valve isolates three sections (respectively, 11", 15", and 12" long) of the backbone for ease in leak checking and making up gas mixtures. All sections of the backbone are joined with Parker-Hannafin connections. A Veeco 1-5/16" bellows valve acts as the roughing valve for the manifold.

Pressure measurements of the test and driver sections are made by three Wallace and Tiernan gauges with (absolute) pressure ranges of 0-800 mm, 0-20 mm, and 0-60 mm p.s.i. They are connected to the manifold by 1/4" stainless steel and copper tubing. Nuclear Products SS-4H stainless steel valves isolate the gauges from the vacuum system.

Four inlets allow for the connection of high-pressure gas cylinders to the lines leading to the shock tube. These are 3/4" stainless steel

tubing and heavy-duty Teflon-lined vacuum hose. Four stainless steel sample tanks (A.C. Tank Company) used for the storage of gas mixtures are connected to the shock tube by 1/4" stainless steel tubing.

The shock tube and pumping manifold are pumped by an Edwards 330 mechanical pump; the mass-spectrometer chamber is pumped by an Edwards 330 mechanical pump and an Edwards 6" diffusion pump.

C. Diaphragms

The 6-3/4" diameter hexagonal diaphragms are cut from .005" thick 1145-0 aluminum foil (Clecon Metals) and scribed in a cross design by a homemade precision scriber shown in Figure 10. The depth of the scriber tip is adjusted so that the diaphrams break at about 23 p.s.i. A properly broken diaphragm (termed full petal) is shown in Figure 11.

D. Schlieren System

The schlieren system consists of a double rowed frame of 10 front-silvered mirrors, an 8 mw He-Ne laser (Spectra-Physics, Incorporated), a homemade photomultiplier box, and associated electronics. The set-up used for schlieren measurements in shown in Figure 12. A circuit diagram of the photomultiplier box is presented in Figure 13.

As the shock wave passes each of the five mirror stations and cuts the laser beam shining through the centerline of the shock tube, the photomultiplier box gives out a blip in response to the change in light intensity across the light sensitive tube. These signal blips

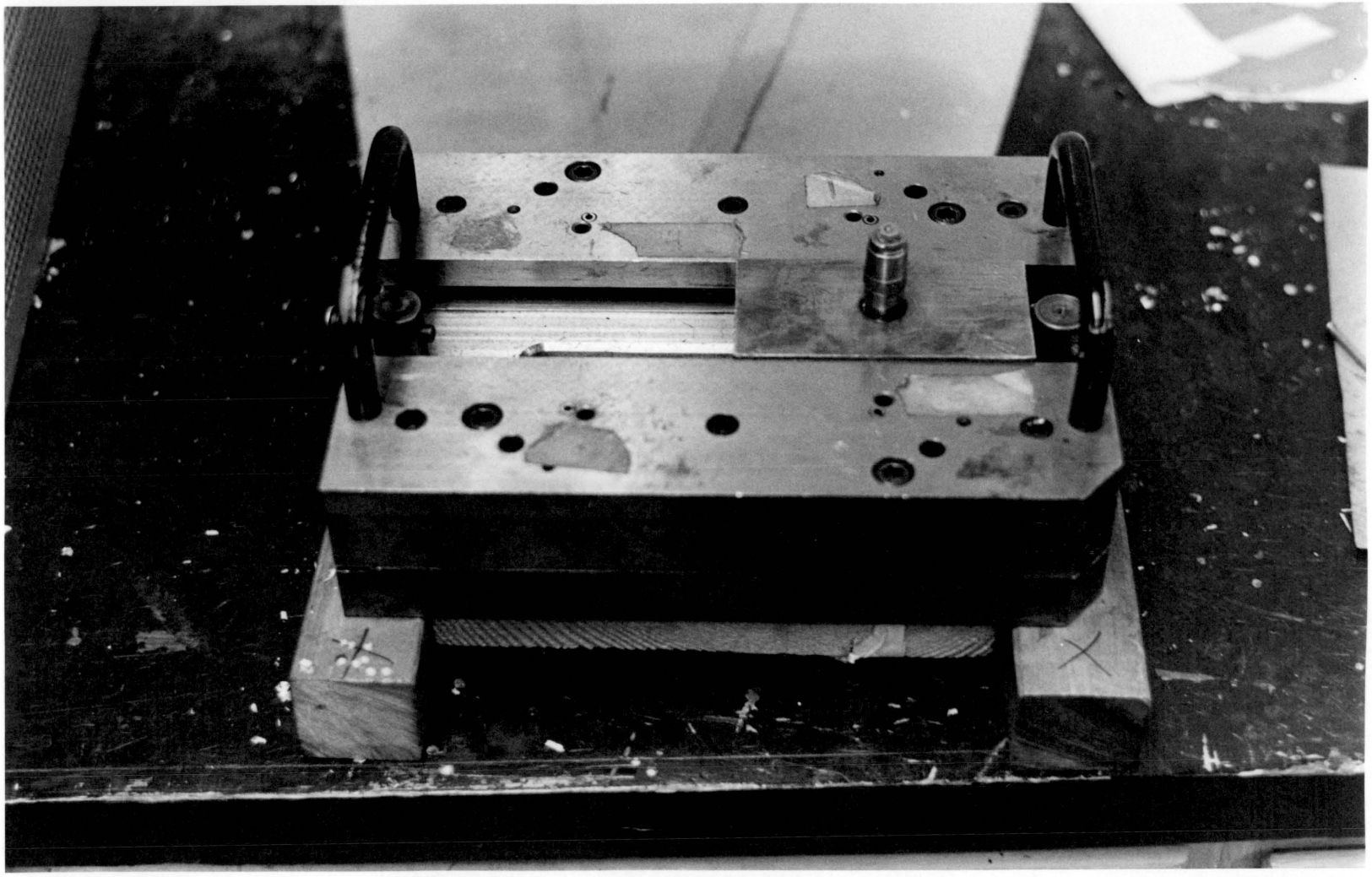

Figure 10. Scriber for Scoring Diaphragms.

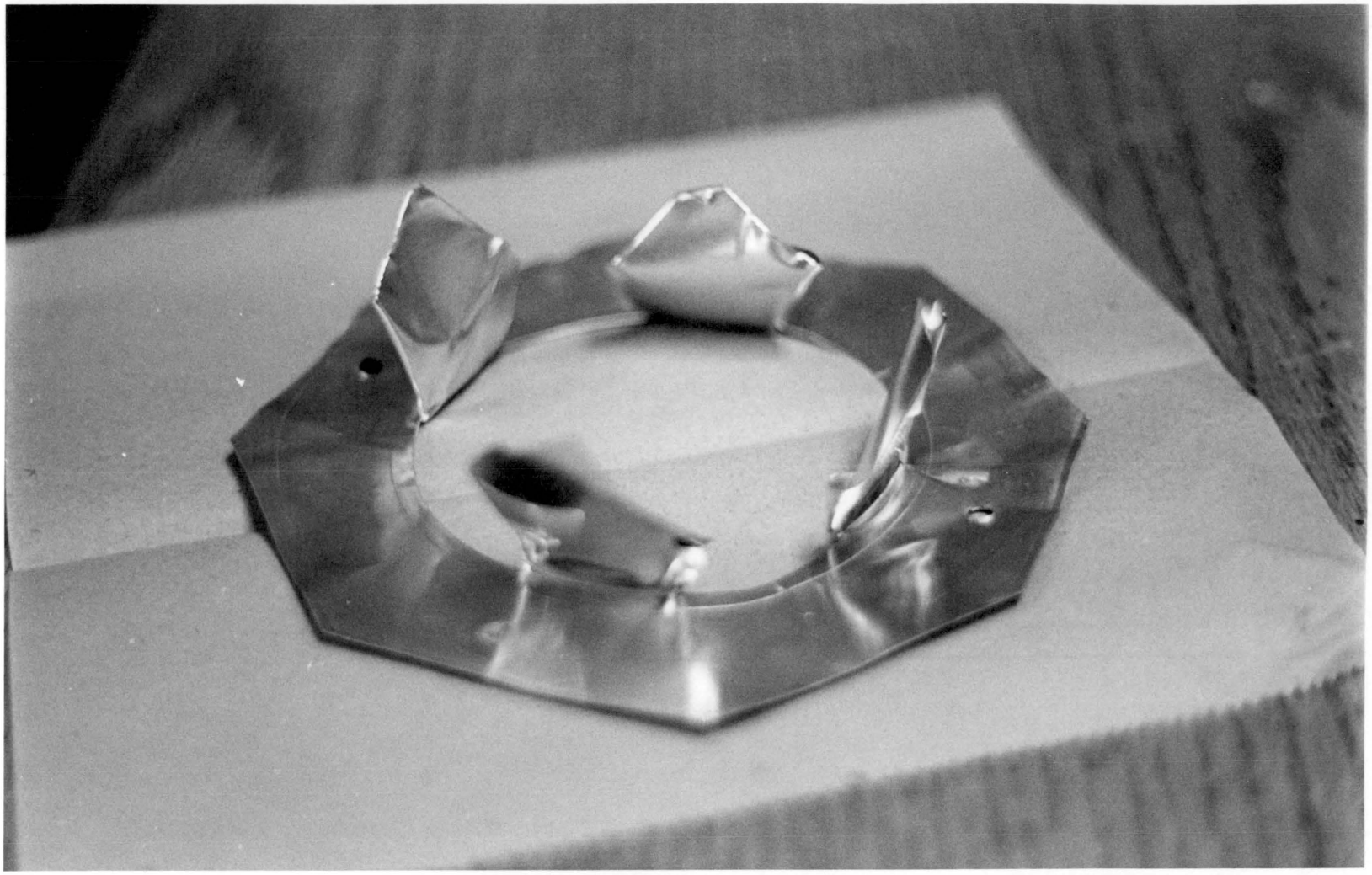

Figure 11. "Full Petal" Diaphragm.

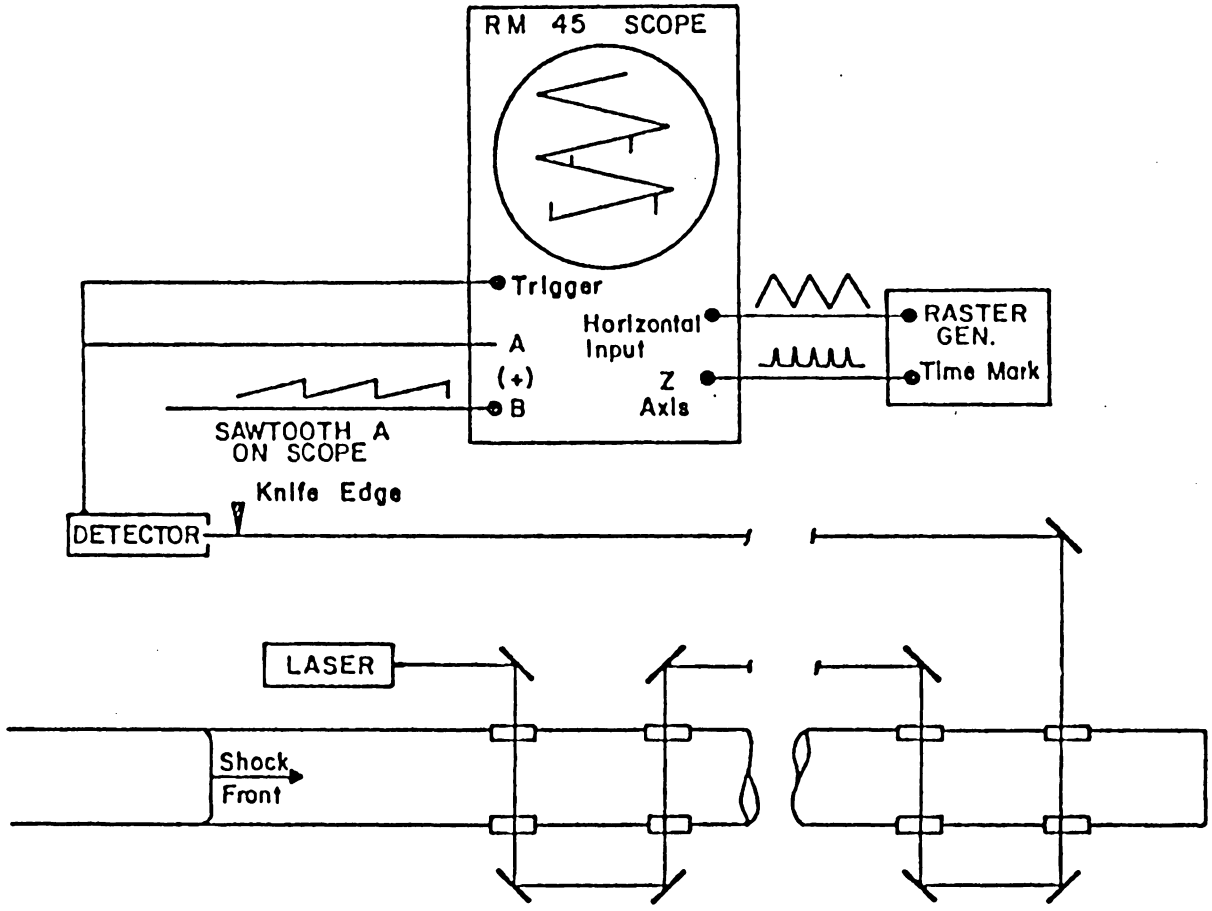

Figure 12. Experimental Set-up for Schlieren Measurements.

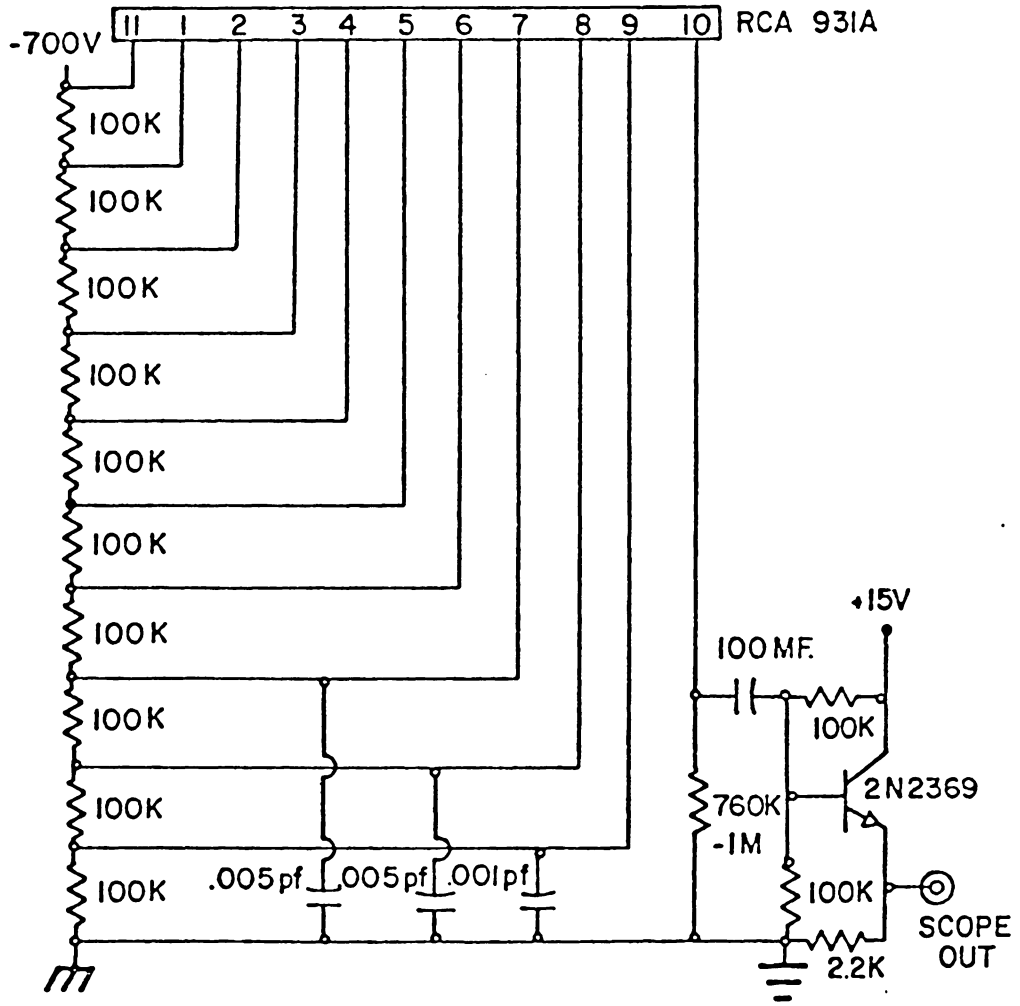

Figure 13. Photomultiplier Box Electronics.

are displayed against the raster time base generated by a crystal-driven triangle and time-mark generator similar to Model TWM-2A produced by Radionics, Incorporated.

The schlieren blips and raster pattern are displayed on a Tektronix RM-45A oscilloscope. It has been modified to give a single sweep output when the raster triangles are fed into the horizontal input of the scope. The vertical sweep is triggered externally by the signal from the first mirror pass and the resulting output is photographed with a Tektronix C-12 camera.

The distance between two adjacent laser beam passes is measured by a Klinger Model 2205 cathetometer. From a schlieren photo (see Figure 14 for a typical example) the time for the shock wave to move between adjacent mirror passes is determined. Therefore, the velocity of the shock wave between beam passes can be obtained, and any deviations from constant velocity are pinpointed. Our schlieren set-up is such that shock wave velocities over the last three feet of the glass portion of the test section are obtained.

E. The Quadrupole Mass-Spectrometer

The quadrupole analyzer is an 11" long aluminum can with Kel-F endcaps. The four cylindrical stainless steel poles are 0.5" in diameter and opposite poles are set 0.436" apart. The Kel-F endcaps support the poles and isolate them from each other.

The R.F. and D. C. voltages are fed to each pair of poles via two feedthroughs on the brass plate of the Pyrex tee of the quadrupole

LASER SCHLIEREN TRACE FOR DETERMINING INCIDENT SHOCK VELOCITIES

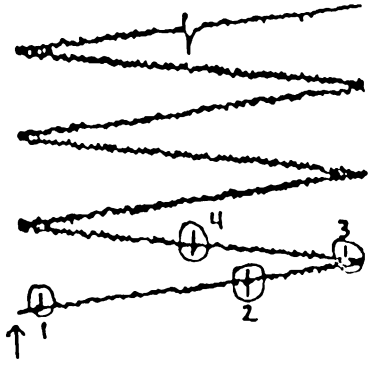

Raster period is 1000 usec. The 4 velocity spikes are labeled. The arrow marks the start of the raster trace.

Figure 14. Schlieren Photo of Sept. 24, 1979; Shot 1.

chamber. The entrance ring of the quadrupole is fixed at -200 V with respect to the electron gun housing. An overview of the quadrupole electronics is presented in Figure 15.

F. The Quadrupole Oscillator

The quadrupole oscillator is a home-made unit operating at a R.F. frequency of 2 MHz. A circuit diagram of the oscillator electronics is presented in Figure 16. Briefly, the oscillator operation is as follows (Figures 15 and 16).

A. When the ϕIE power supply is on the filaments of tubes 6146A, 6BH6, and 12AX7 are activated. The green light on the front panel of the oscillator becomes lit.

Relay K_3 is activated after a short time delay. The K_3 coil, by zener control, allows relay K_1 to close; relay K_2 latches and deactivates relay K_3. The power is shunted via IN2071; the red light becomes lit, indicating that the power amplification portion of the circuit is operational.

B. When the 320 volt power supply is one, the white light on the oscillator is lit, indicating that the 2MHZ crystal is functioning in the circuit. A sine wave at point A at the crystal frequency is the result. [Point A is ganged together with point B].

C. The Fluke power supply on the high voltage setting acts to amplify the magnitude of the sine waves given out at points A and B. The matched pair of sine waves is applied to each respective pair of poles.

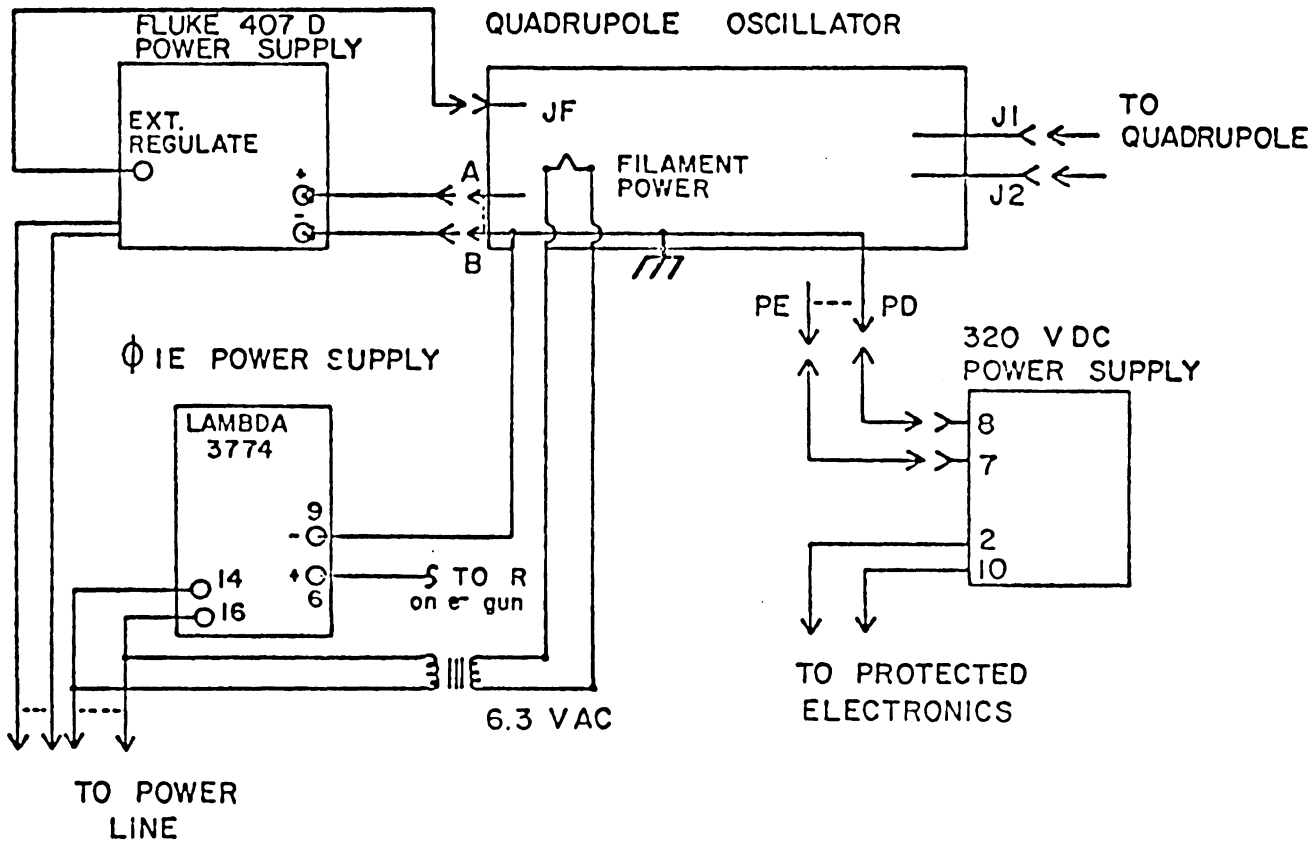

Figure 15. Overview of the Quadrupole Electronics.

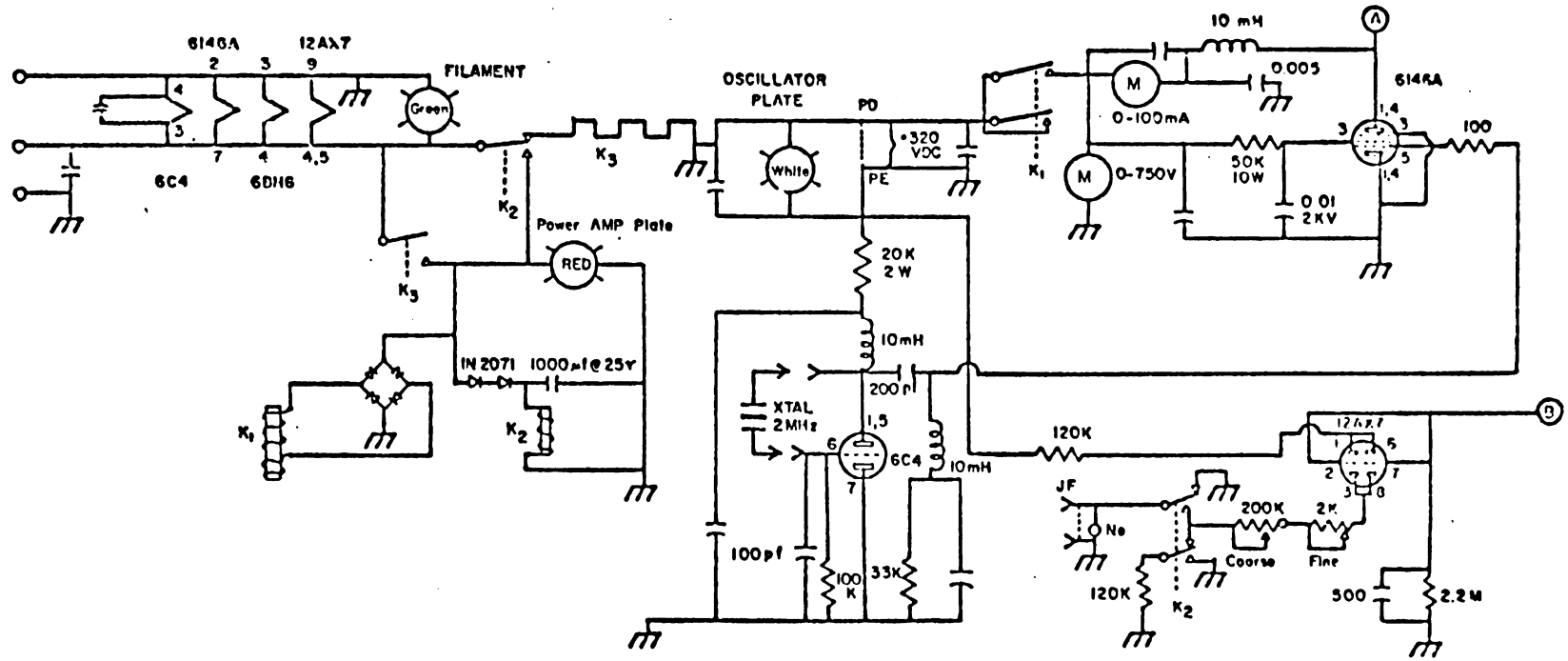

Figure 16a. The Quadrupole Oscillator Electronics.

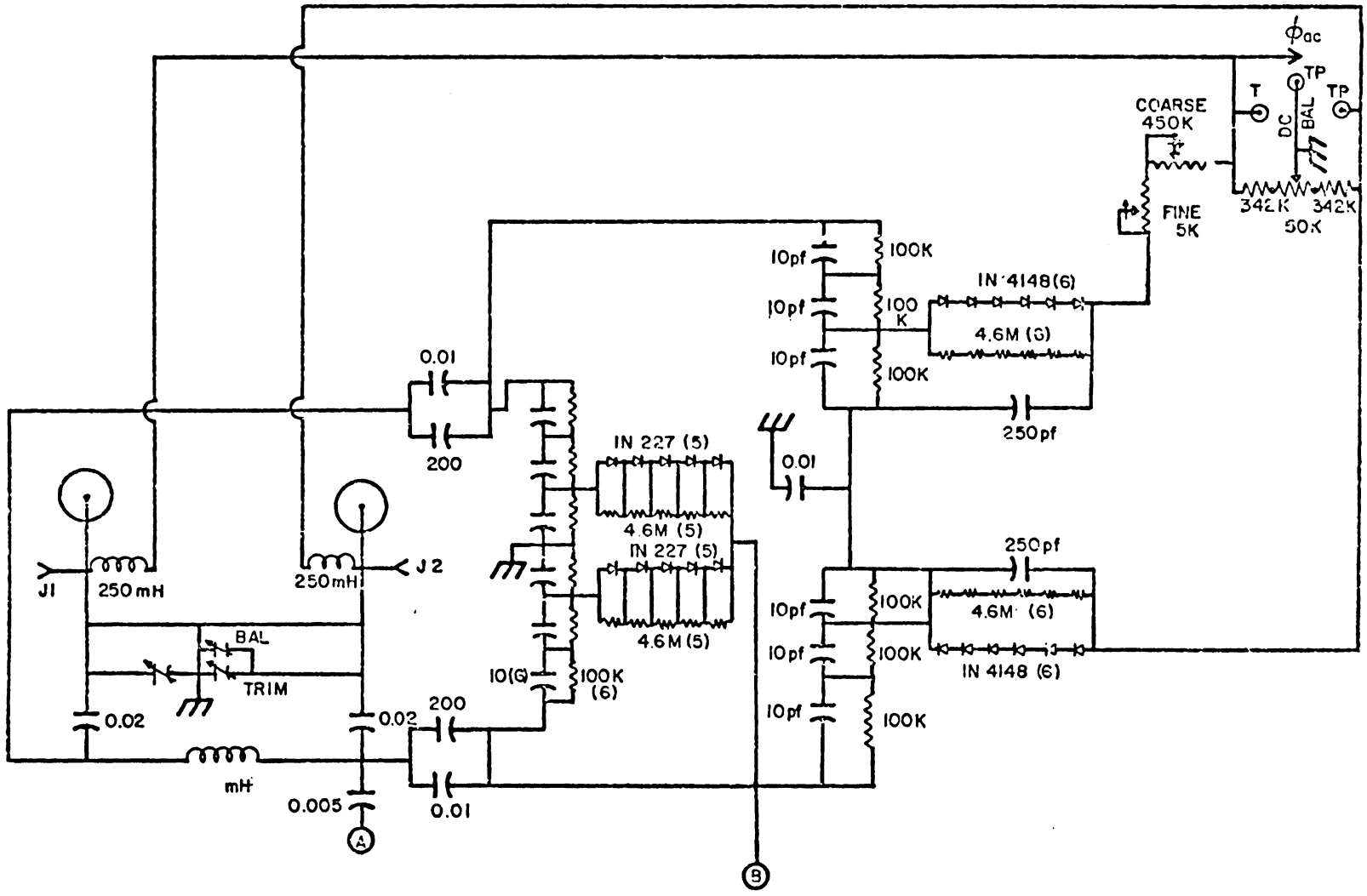

Figure 16b. The Quadrupole Oscillator Electronics for ϕ_{DC}.

G. Ion Source and Associated Electronics

The electron gun (ion source) is shown in Figures 17 and 18. It consists of a commercial filament (Dupont Filament/Heater Assembly 38760), a cylindrical repeller element and lens mounted on a Mykroy 1100 block, and a brass trap which is mounted over the 0.06" diameter exit hole. The collimated electron beam shoots across the open square, goes through the exit hole, is trapped, and registers a trap current (on the order of 5-10 μamps) on the Weston 622 Precision Microammeter. Typical spacings for the electron gun parts are 0.010" spacing between the repeller and lens, and a 0.014" gap between the lens and the adjacent wall. The electron gun power supplies are all commercial except for the homemade trap supply. The commercial supplies are the following: the filament supply is a Kepco JQE model variable from 0-6 volts and 0-10 amps. The electron repeller and lens supplies are Kepco ABC type which can be varied from 0-500 volts. Kepco Kr-11 supplies (0-160 volts) regulate the ion chamber and electron energy voltages. The electron gun power supplies regulate the electron beam functions shown in Table 7.

H. Ion Optics

Positive ions which are created by electron impact of the jet exiting the shock tube are repelled upwards by the positively-charged ion repeller plate. The ions pass through the exit slit into a lens system consisting of nine cylindrical lenses and two deflection plates.

The lenses are variable from 0 to -200 volts with respect to the

Table 7. Functions of the Protected Electronics Voltages

ϕ_{IR} (ion repeller)	Voltage which deflects electronic beam vertically; also repels ions into ion optics
ϕ_{IC} (ion chamber)	Voltage which deflects electron beam horizontally
ϕ_{EE} (electron energy)	Voltage which maintains the electron beam at a fixed energy; it is the potential difference the electrons fall through from their initial energy of formation at the filament to their final energy at the housing of the electron gun
ϕ_{EL} (electron lens)	The lens voltage which allows collimation of the electron beam
ϕ_{ER} (electron repeller)	The repeller voltage causes electrons to be accelerated away from the filament toward the electron lens
ϕ_{Trap} (electron trap)	Traps electrons as they exit the ion chamber so that trap current can be measured
ϕ_{FIL} (filament)	Causes filament to heat up and eject electrons
ϕ_{IE} (ion energy)	Maintains ions at a fixed energy; it is the potential the ions fall through from their creation at the ion chamber to their arrival at the quadrupole entrance
ϕ_{DP1} (deflection plate 1) ϕ_{DP2} (deflection plate 2)	These voltages orient the ions under the entrance to the quadrupole; deflection plate 1 is negative with respect to deflection plate 2

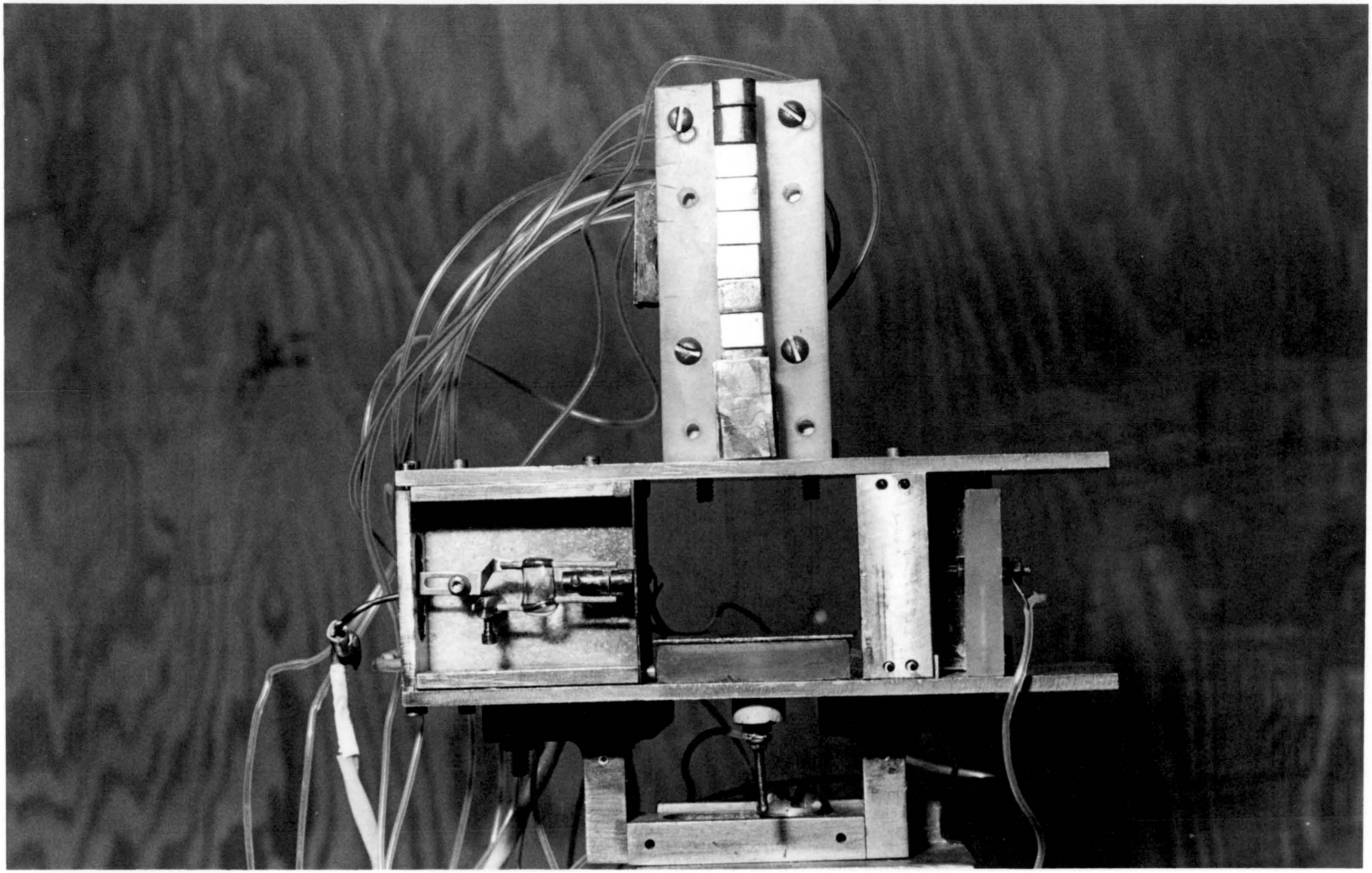

Figure 17. Details of Electron Gun.

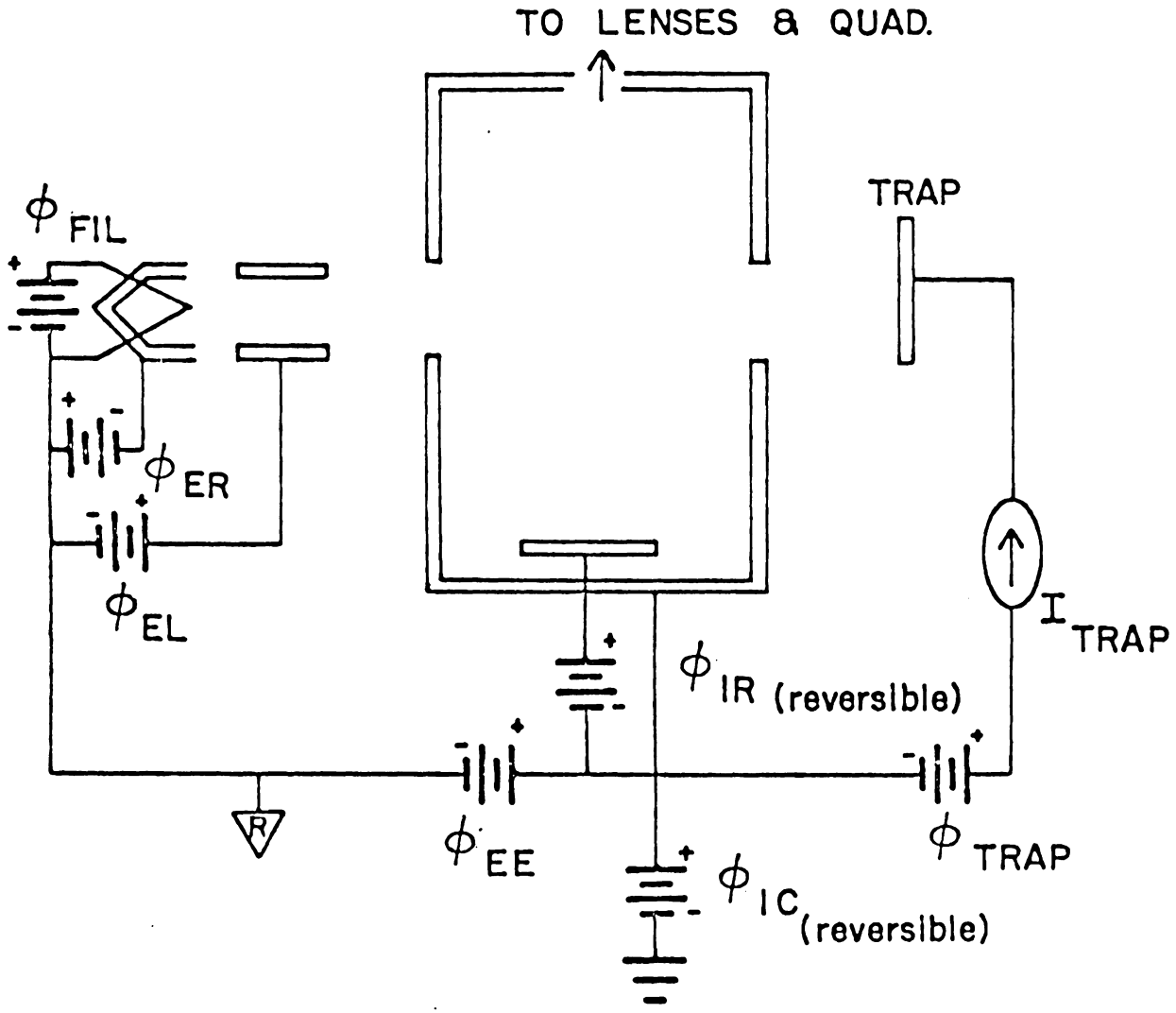

Figure 18. Electron Gun Electronics.

ion chamber. Lenses 2 and 8, 3 and 7, and 4 and 6 are electrically connected so that the nine lenses form one symmetrical einzel lens structure. The two deflection plates (See Table 7) serve to orient the ions on the cylindrical axis of the quadrupole before they transit the lens structure.

Typical spacings between the lenses (set by a feeler gauge) are the following: (lens 9 is the top lens near the quadrupole entrance)

Lens	9-8	.010"
	8-7	.016"
	7-6	.010"
	6-5	.012"
	5-4	.012"
	4-3	.010"
	3-2	.013"
	2-1	.014"

I. Detection

The electron multiplier used in our studies is a Galileo 306 magnetic electron multiplier shown in Figures 21 and 22. The ions exiting the quadrupole pass through the finely-meshed grid and hit a tungsten cathode. Electrons emitted from the cathode cascade down the dynode strip and hit the anode. The resulting current (typically, on the order of 10^{-6} amps) is monitored on a Keithley 410-A electrometer.

During shots, the anode output is fed directly to an HP-450A

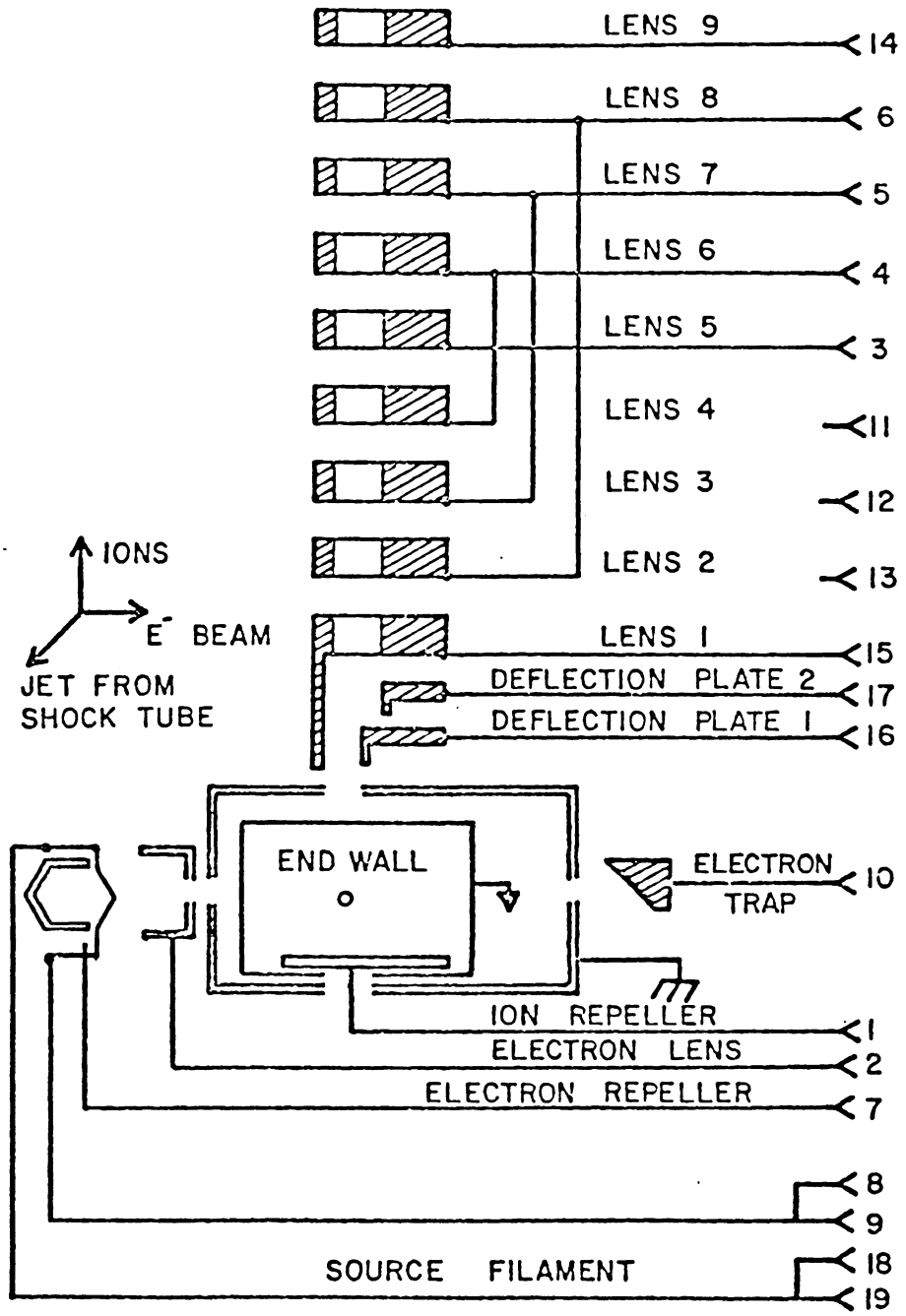

Figure 19. Ion Source Relative to the Shock Tube Endwall.

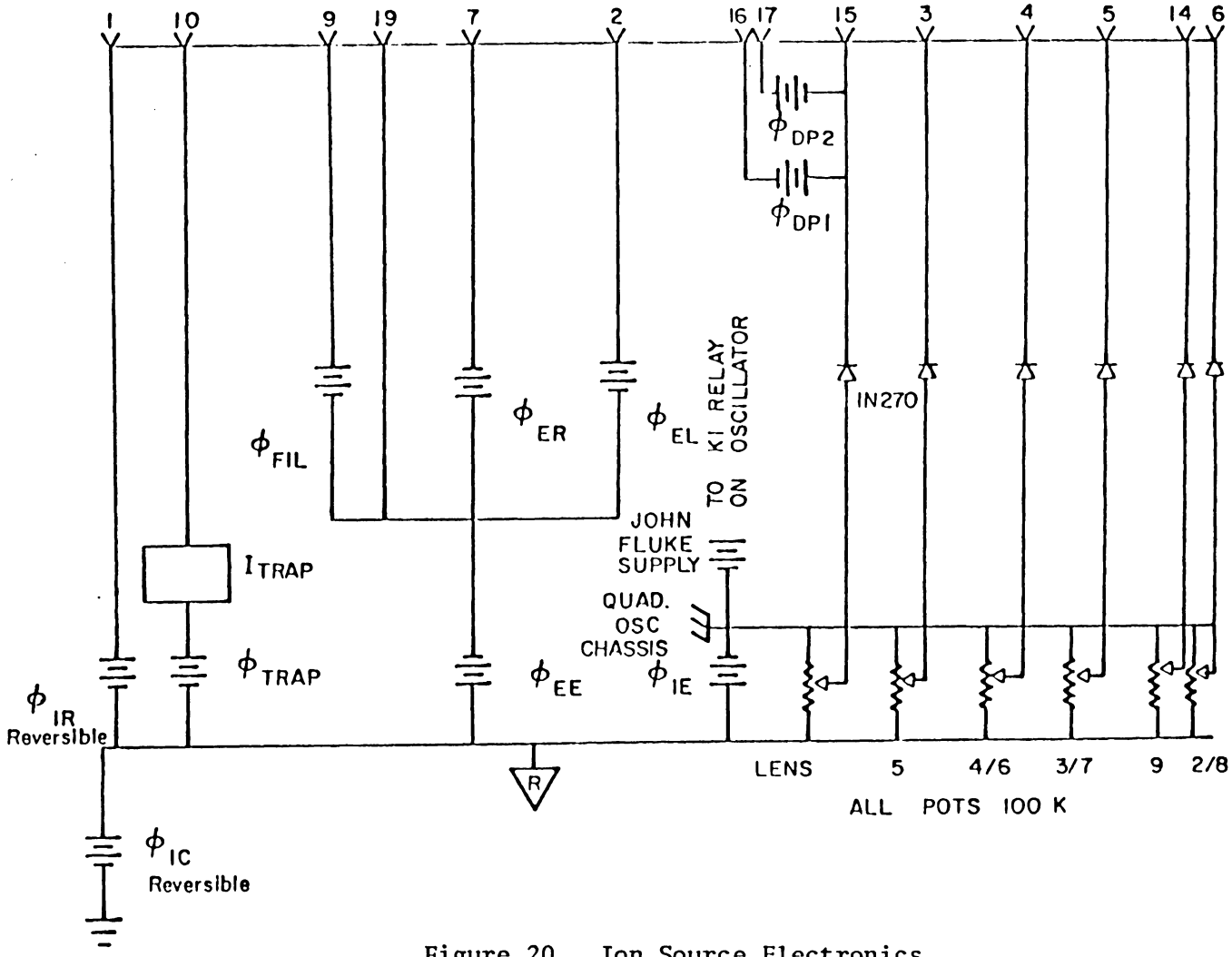

Figure 20. Ion Source Electronics.

amplifier with 150 ohm termination at the slope. The resulting amplified output is sent to the positive input of a Type 565 dual beam oscilloscope. The scope is triggered by the leading edge of the signal itself.

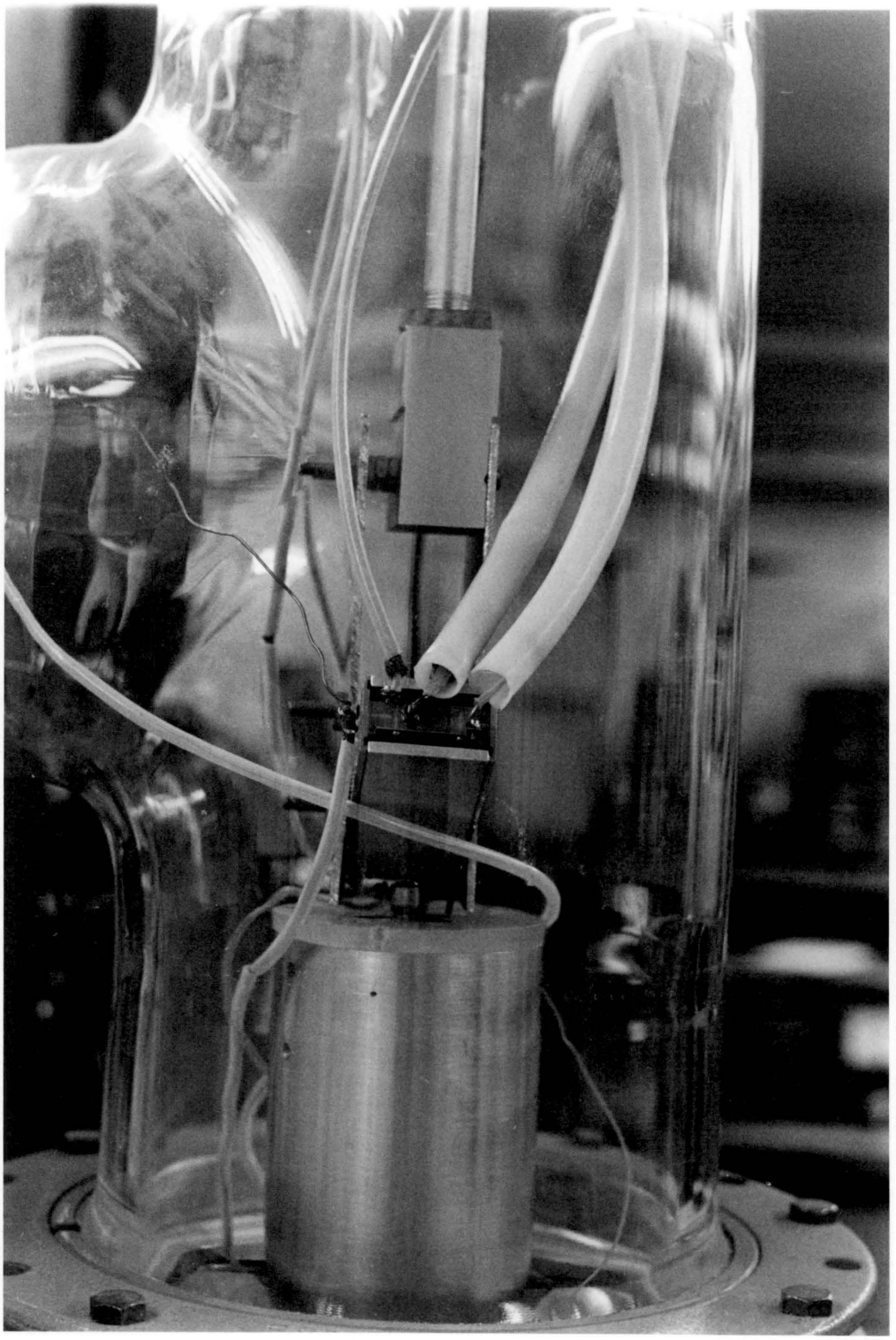

Figure 21. The Mass-Spectrometer Chamber; the Electron Multiplier is above the Quadrupole Mass-Spectrometer.

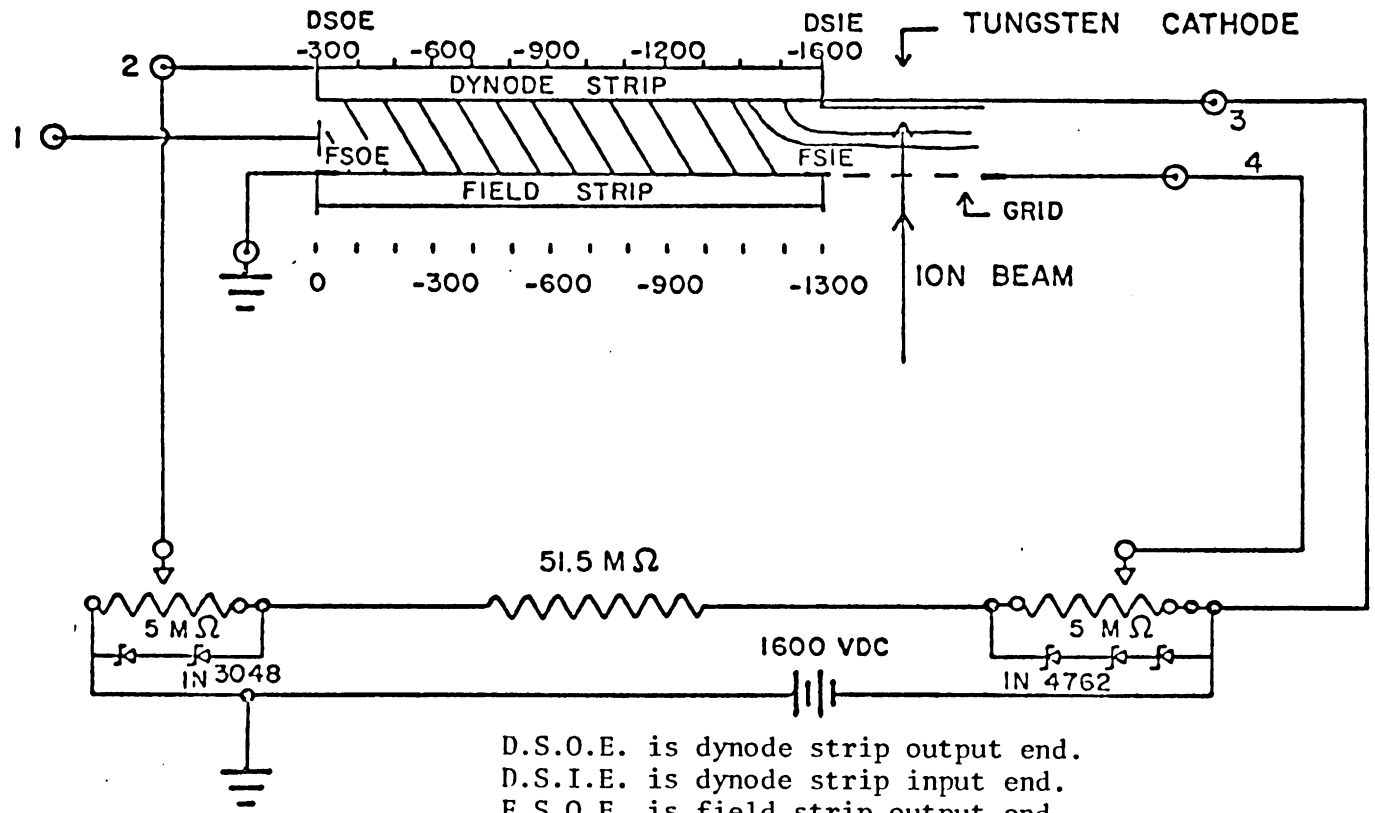

D.S.O.E. is dynode strip output end.
D.S.I.E. is dynode strip input end.
F.S.O.E. is field strip output end.
F.S.I.E. is field strip input end.

Figure 22. The Electron Multiplier.

III. EXPERIMENTAL

The basic components of the shock tube and mass-spectrometer system were available at the outset of this study. A shock tube/mass-spectrometer system was set up with the available equipment. The apparatus was basically a copy with some modifications of the system originally designed by Belford, Hay and Gutman at the University of Illinois. The original design is described in references 15, 20, 22 and 28.

The experiments presented in this section were intended to characterize our apparatus and to test its capabilities for kinetic measurements. Because our apparatus was modeled after the University of Illinois set-up with additional modifications, the possibility of attempting a study which would be an extension of the earlier work of Gutman et al.[15] was suggested. This experiment (a jet scanning study) was described earlier in the introduction, p. 38-41.

A. Schlieren Measurements

These experiments were performed with the shock tube to test the operation of the schlieren system and to characterize the flow properties of the shocked gas. A blank endwall replaced the spinneret endwall for the schlieren measurements.

The experimental setup was as shown in Figure 12. The position of the photomultiplier box was tested by chopping the laser beam with a rotating disk having a small slit cut along a radius. The disk was

mounted on a ringstand and had its speed adjusted by Variac control of its motor. When the laser beam was located in its most sensitive position on the aperture of the box, (this position was when the light was partly on-partly off, the edge of a razor blade placed horizontal across the aperture of the photomultiplier box) blips about 2 volts high were viewed on the RM 45A scope. The scope was switched to "normal mode" and the blips were viewed on channel A during this time. The height of the box was adjusted by its Jiffy-Jack support.

The raster was then connected to the RM 45A scope on single sweep. The scope was switched to raster mode. The trigger level of the scope was adjusted such that the interruption of the beam by a thin flexible wood stick caused a flash of the raster pattern on the scope screen. The trigger slope was negative to catch the blip caused by the shock wave passing the first mirror station.

A series of shots fixed into 5 torr air or 5 torr argon were done using various driver gas mixtures of argon and helium. The results of these experiments are shown in Tables 8-10. It can be noted from Tables 8-10 that the shock wave velocity was non-uniform for all of the shots and that the velocity changes between laser pass intervals were also erratic. Figure 23, a plot of incident shock velocity (Table 9) vs. distance from endwall (here, the shock wave velocity was considered to be measured from the center of a laser pass interval) for some selected argon pictures shows that we are unable to predict the shock wave velocity at the endwall from the trends in the data.

We attempted to pinpoint the causes of the erratic data[a] but found that the schlieren electronics were correctly calibrated and that the large non-uniformities of our data could not be attributed to mirror vibration or movement of the laser.

We decided to move the schlieren mirrors closer to the endwall and to reduce the number of mirrors to five in the hope that we would have enough light intensity to catch all five signal blips. However, during these experiments, it was also found that at the new location the output of the photomultiplier box was weaker so that even pure helium, full petal shots were not always successful in triggering the scope. We attempted to boost the signal gain of the photomultiplier box by replacing the 100K resistor by one of 10^6 ohms. This gave somewhat better success in scope triggering, but difficulties in catching all five blips still remained. Redesigned schlieren electronics would be needed to get higher signal gain.

The data obtained from these shots are shown in Table 10, and shock velocities versus distance from the endwall are plotted in Figure 23. Except for shot 1, September 9, 1979, all the shots again show erratic velocity changes as measured which indicate that the

---

[a] Dean (See Reference 22) also obtained erratic accelerations and decelerations for his flow data. However, the magnitude of his velocity differences was far smaller than ours. Furthermore, he used transducers as the monitoring devices for the passage of the shock wave. He attributed his poor data to possible faulty firing of the pressure transducers for incident shock velocities less than 1 mm./μsec. Our data (Table 10) shows erratic effects for velocities on the order of 1 mm./μsec.

Table 8. Schlieren Data
Test Gas: Air
P_1 = 5 torr

Shot #[a]	Incident Shock Wave Velocity (mm/μsec.) between Laser Passes					% Attenuation/Meter			
	1-2	2-3	3-4	4-5	5-6	1	2	3	4
Aug. 12, 1976 #2]	0.364	0.421	0.637			-76.0	-260.1		
Aug. 12, 1976 #4]	0.836	0.736	0.899	0.822		47.7	-111.9	41.4	
Aug. 12, 1976 #5]	0.577	0.295	0.332			236.4	- 64.9		
Aug. 12, 1976 #6	1.52	0.736	0.728	0.967		249.2	5.83	-157.1	
Aug. 12, 1976 #7?	0.727	0.320	0.306			270.5	22.8		
Aug. 12, 1976 #8?	0.364	0.295	0.566			91.77	-466.9		
Aug. 12, 1976 #9	0.724	0.614	0.300			73.5	259.0		
Aug. 18, 1976 #1	0.836	0.669	.748			96.4	- 44.22		
Aug. 25, 1976 #2?	0.880	0.669				115.7			
Aug. 25, 1976 #3?	0.836	0.818	0.695			10.5	76.4		
Aug. 31, 1976 #3	0.836	0.866	0.849			-17.34	9.99		
Aug. 31, 1976 #4]	1.05	0.866				82.77			
Aug. 31, 1976 #5?	0.984	0.818	1.09			81.36	-169.2		
Sept. 1, 1976 #5?	0.408	0.866	0.665			542.9	117.9		
Sept. 1, 1976 #6	0.984	0.368				302.4			

[a]? indicates a non-uniform diaphragm break,
] means that the break was not recorded,
* indicates am ambiguous noise distance.

See the Schlieren program for a detailed explanation.

Table 9. Schlieren Data[a,b]
Test Gas: Argon
P_1 = 5 torr

Shot #	Incident Shock Wave Velocity (mm/μsec.) between Laser Passes						Attenuation, %/Meter				
	1-2	2-3	3-4	4-5	5-6	6-7	1	2	3	4	5
Feb. 26, 1977 #4*	0.765	0.812	0.763				-29.8	29.4			
Feb. 26, 1977 #5?	0.925	0.798	0.969				66.4	-105.3			
March 2, 1977 #3?	0.878	0.782	0.816	0.740			52.7	-21.4	47.3		
March 2, 1977 #4A	0.448	0.541					100.9				
March 2, 1977 #4B	0.448	1.01	0.884				60.4	59.3			
March 2, 1977 #4C	0.954	0.844	1.01	0.832			55.5	-96.5	89.1		
March 2, 1977 #5*	0.954	0.879	1.12	0.832	0.997		37.7	-132.4	128.7	-93.8	
March 2, 1977 #9?	0.954	0.960	0.884				-2.8	38.7			
March 3, 1977 #4]	0.784	0.812	0.707				-17.4	63.3			
March 3, 1977 #9	0.448	0.880	0.884				465.8	- 2.4			
March 3, 1977 #10*]	0.884	0.660	0.786	0.666	1.09		105.5	-93.9	77.2	-300.2	
March 3, 1977 #12	0.708	0.918					143.3				
March 6, 1977 #1?*	0.645	0.782	0.589	0.768			102.2	121.0	-153.1		
March 6, 1977 #2	0.878	0.704	0.816	0.740	0.825	0.720	95.8	78.4	47.3	-54.6	62.0
March 6, 1977 #3*	0.978	0.941	0.800	0.753	0.809	0.874	18.3	73.6	29.7	-35.1	-39.4
March 6, 1977 #4*	0.828	0.740	0.905	0.725			51.5	-109.8	100.1		
March 6, 1977 #7*	0.879	0.725	0.816	0.711	0.920	0.692	84.7	-61.7	64.9	-139.2	120.7
March 6, 1977 #8*?	0.844	0.752	0.927	0.738	1.05		52.7	-114.6	102.8	-197.0	
March 6, 1977 #11*?	1.04	0.812	0.884	0.832	0.997		107.7	-43.6	29.7	-93.8	
March 6, 1977 #12*?	0.936	0.796	0.991	0.783	0.938	0.734	71.7	-120.0	105.8	-93.8	106.0
March 6, 1977 #13*?	0.828	0.714	0.905	0.783	0.757	0.734	66.4	-131.2	67.7	16.1	14.4

[a]See computer output notebook for the Schlieren program.

[b]This set of data was taken after a new test section bellows stem had been machined to be flush with the contours of the shock tube wall; the former valve protruded into the gas flow.

Table 10. Schlieren Data[a,c]
Test Gas: Argon
P_1 = 5 torr

Shot #	Rupture	Velocities, mm./μsec. 1-2	2-3	3-4	4-5	Attenuation, %/meter 1	2	3
Sept. 9, 1979 #1	Full Petal	1.21	1.39	1.34	1.26	-69.7	19.5	33.1
Sept. 17, 1979 #1	Full Petal	1.68	1.18	1.02		139.4	73.5	
Sept. 17, 1979 #7	Full Petal	1.6	1.16	0.903		128.9	120	
Sept. 24, 1979 #2	Half Petal	0.971	1.43	0.697	0.963	-221.4	277.8	-211.
Sept. 24, 1979 #3	Half Petal	0.923	1.67	0.909	0.876	-379	246.9	20.1
Sept. 24, 1979 #4	not noted[b]	1.09	1.43	0.631	1.01	-146.1	302.8	-322.8
Sept. 24, 1979 #5	Half Petal[b]	0.902	1.22	0.281		-165.1	417.2	
Sept. 24, 1979 #7	not noted[b]	0.784	1.22	0.539		-260.4	302.5	

[a]Schlieren mirrors were moved closer to the endwall for these shots. Laser pass intervals were: 1-2, 205 mm.; 2-3, 222 mm.; 3-4, 147 mm.; 4-5, 214 mm. Endwall to mirror 5 was 48.3 mm.

[b]Was either a half or full petal.

[c]Only photos having 4 or 5 blips were analyzed. 17 3-blip photos were rejected from the total sample.

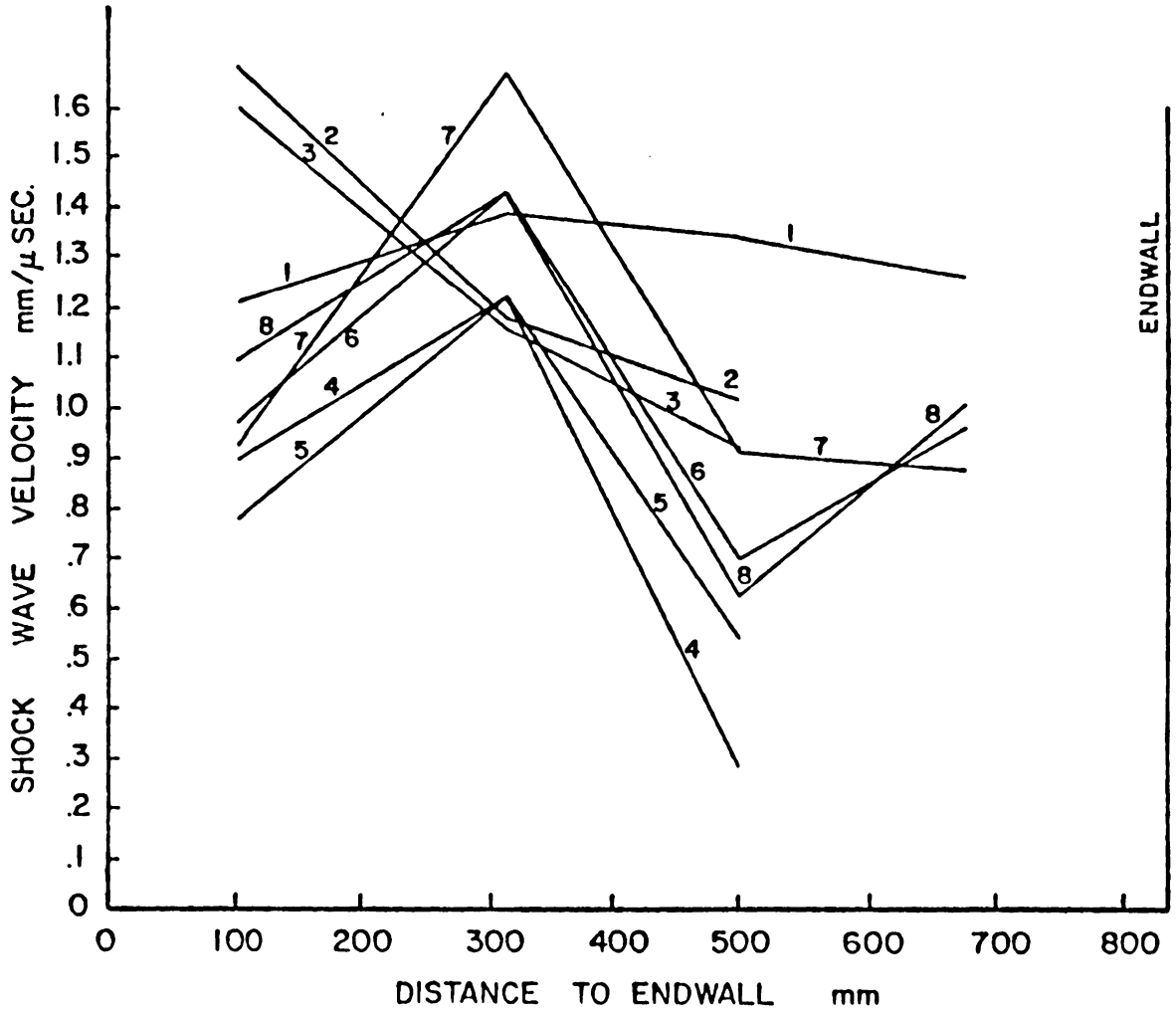

Figure 23. Schlieren Data of Table 10.

shock wave velocity at the endwall cannot be predicted from data obtained further upstream. Schlieren work cannot be done further down on the tube as the aluminum sleeve coupling the shock tube with the mass-spectrometer chamber begins a short distance after the last mirror. A discussion of the errors in the schlieren data is presented in a later section.

B. Calibration Experiments

These experiments were performed with the coupled shock tube/mass spectrometer to check the operation of the mass-spectrometer under conditions that would simulate those found during the firing of shots.

These experiments include the measurement of ion current versus $P_{\text{shock tube (s.t.)}}$ and $P_{\text{mass-spectrometer (m.s.)}}$ for static conditions in which gas was leaked into the mass-spectrometer chamber via the shock tube. The results of these experiments are shown in Figures 24-25. The purpose of the calibration experiments was to compare the ion signal [N_2^+ was monitored) with the shock tube pressure obtained when air was leaked into the shock tube. One could consequently expect that a similar correlation would hold during actual kinetic runs. The magnitude[a] of ion current obtained when gas was

[a] Under similar operating conditions (some partial pressure of the monitored component in the test gas mixture, same electron multiplier gain) the output ion current for the non-reactive dynamic shots (see Section D) was in general, lower than the ion current obtained during the static experiments presented here. The density difference between the free jet flow (dynamic experiments) and the (viscous) flow of the leaked gas (static experiments) might account for this experimental observation.

compressed by shock heating could then be compared to the partial pressure of the monitored component in the test gas mixture.

It can be noted that for the pressure vs. ion signal plots (Figures 24, 25) that the results were affected by whether gas was bled into the mass-spectrometer chamber or evacuated out of the chamber. The measurements of ion current were taken only after the pressure in the chamber stabilized when gas was bled in or removed. The reason for the data scattering in Figure 24 is not obvious in the cases where $p_{\text{shock tube}}$ was increased. (See points 1-10). In any event, the plot shows a linearity in ion signal up to about $p_{\text{shock tube}} = 5$ torr.

For the plot of $p_{\text{mass-spectrometer chamber}}$ vs. ion current, a reasonable explanation for the data scatter for points 1-10 is simply that the measurement of pressure in the chamber was made at a position far removed from the site of gas flow into or out of the chamber. Therefore, it could well be that the measured pressure was not a true reflection of the gas pressure (density) sampled by the quadrupole to give an ion current. It could be that the ion gage responded to the different effects caused near the gage by the local increases in pressure in the ionization chamber of the ion source. The pressure in such a case should be monitored by an additional ion gage near the ion source.

It should be noted here that the mass flow can be affected by a dirty leak. Earlier linearity studies showed that higher (-10 torr) shock tube pressures could be used without swamping the mass-

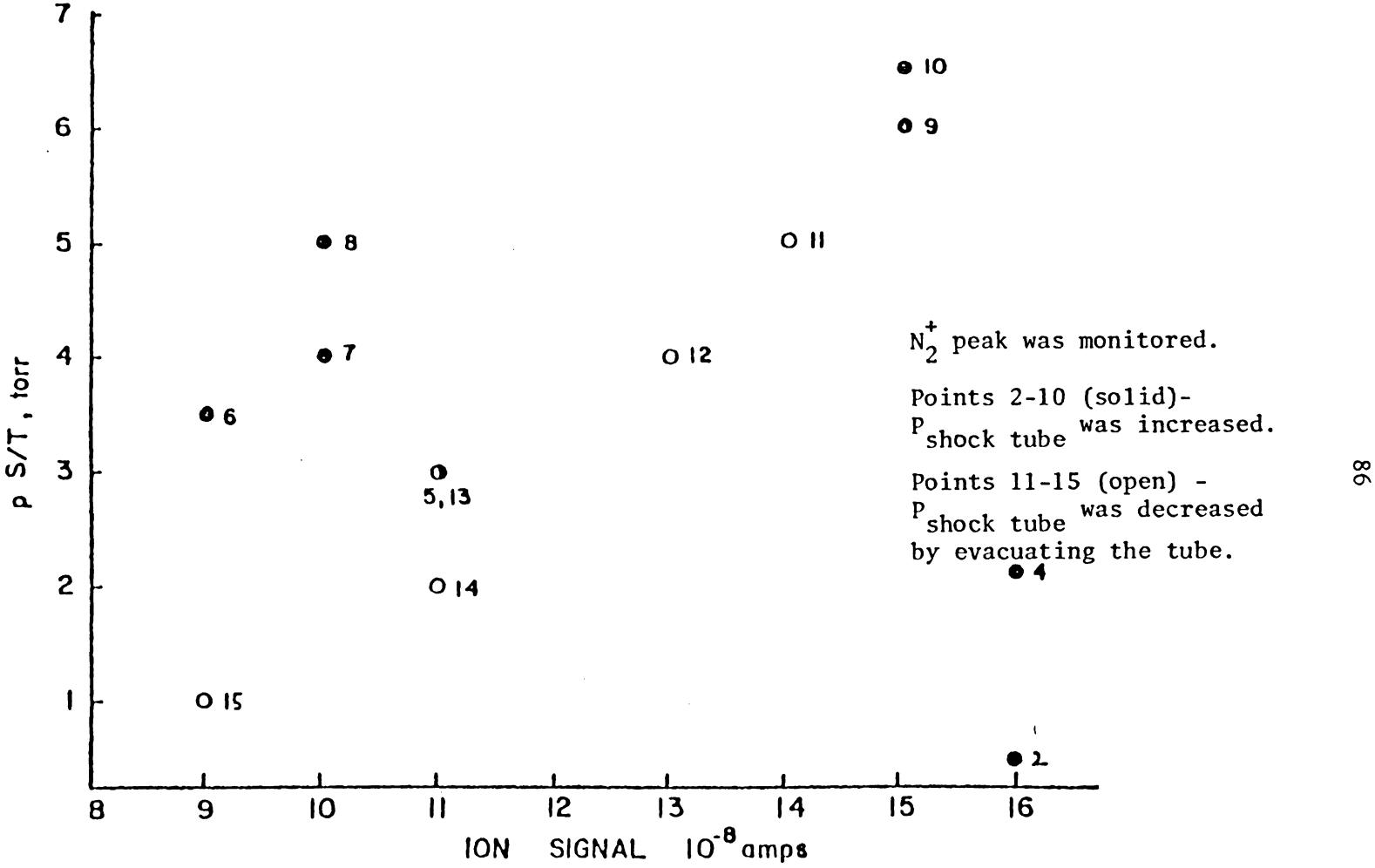

Figure 24. Plot of $P_{shock\ tube}$ Vs. Ion Current.

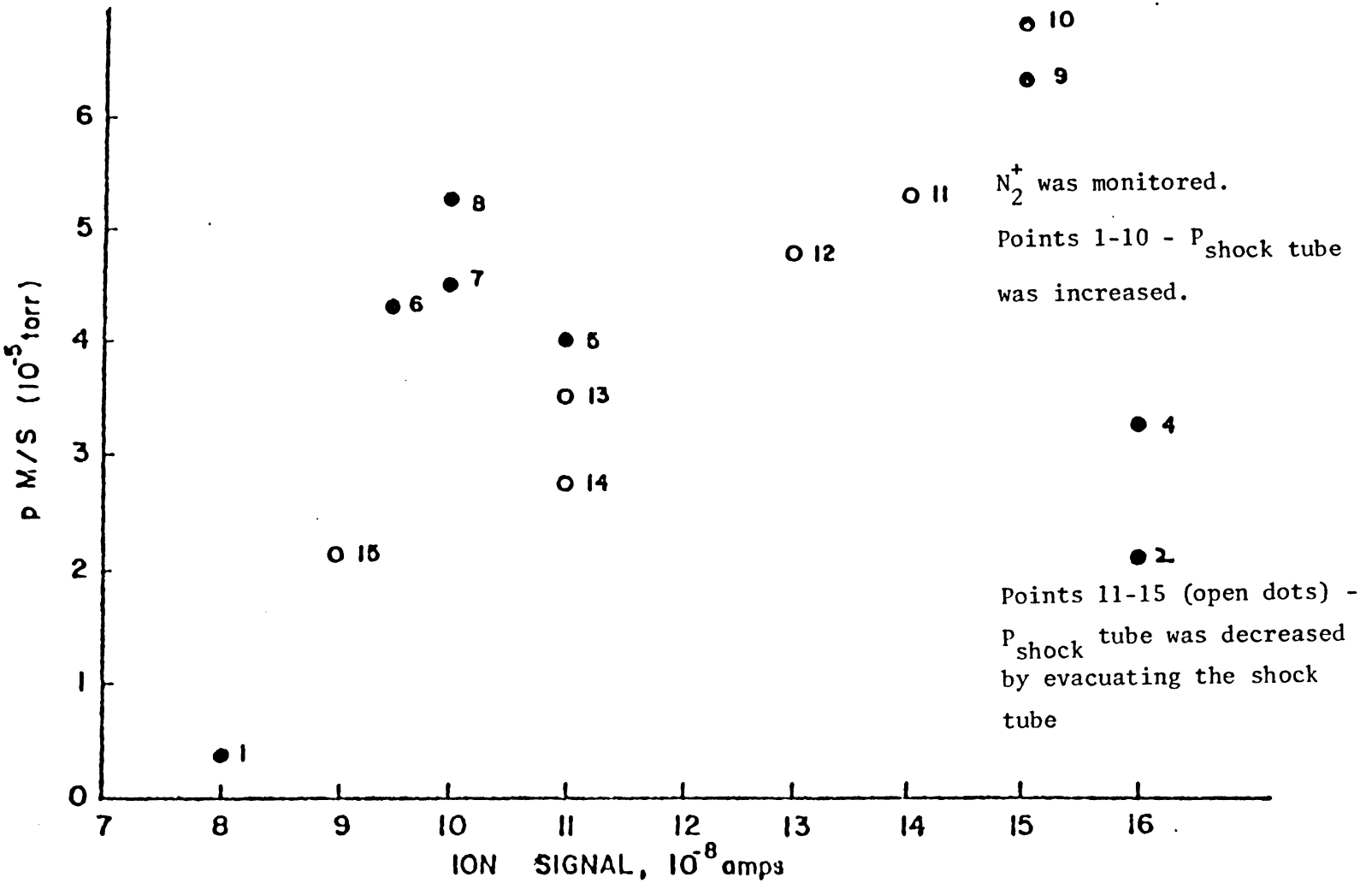

Figure 25. Plot of $P_{mass\text{-}spectrometer}$ Vs. Ion Current.

spectrometer. Cleaning of the leak was done with an ultrasonicator and by using several changes of alcohol and acetone during the cleaning process.

Electron multiplier voltages of 1600V were adequate for the static studies, ion currents of 10^{-6} amps could be attained.

A plot of the electron multiplier voltages versus ion current (static measurement) is shown in Figure 26.

C. Testing of Amplifiers for Dynamic Ion Signals

a) Short time response

During a dynamic shot, the anode output of the electron multiplier (current $\sim 10^{-8}$ - 10^{-6} amps for static, non-reactive conditions) is amplified and fed to an oscilloscope so that photographs of shots can be made. The amplification of ion current from a non-reactive shot is the most strenuous test of an amplifier; the square shape of a non-reactive signal involves the greatest number of harmonics and these can cause "droop" of the signal should an unsuitable amplifier be used.

We chose to test our amplifiers by simulating the shape of a non-reactive signal (ion current) and then amplifying the resulting ion current. The ion drawout pulse of the T.O.F. (width - 1 μsec. height = 100 v.) served to simulate the sharp leading and falling edges of a non-reactive ion signal and in addition, provided a check on the short term response of the amplifier.

The experimental set-up used is shown in Figure 27. Ion current (10^{-8} amps) was obtained by monitoring the Ar^+ peak. A train of

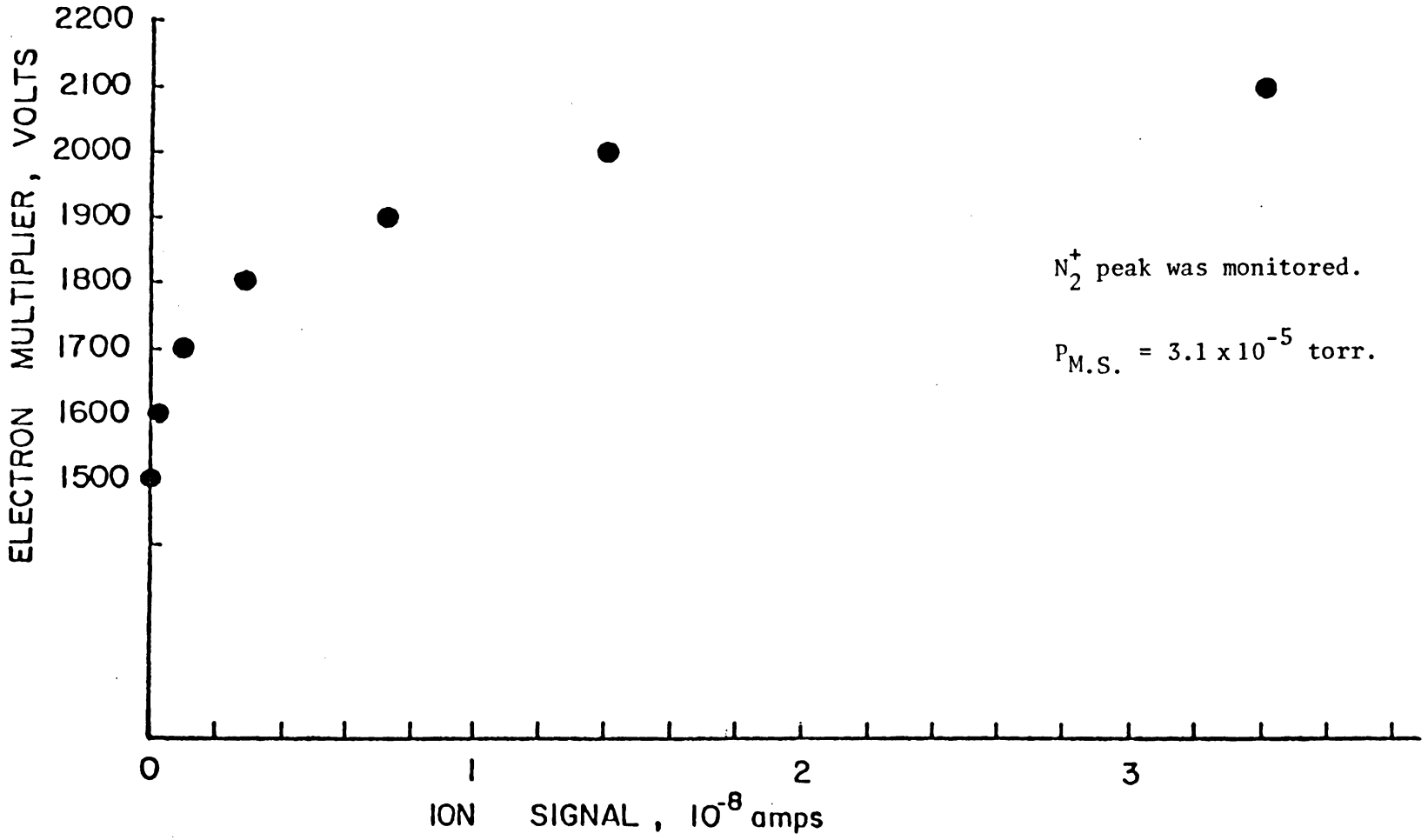

Figure 26. Electron Multiplier Voltages Vs. Ion Signal.

negative drawout pulses was then fed into the field strip output end to disrupt the field lines and interrupt the ion current. The current output from the anode was input to the chosen amplifier.

The results of such a measurement using the HP-450A amplifier is shown in Figure 28. It can be seen that the HP-450A model tracked the ion drawout pulse shape well. Similar testing of our homemade current amplifier using the 50-j chip ended when the chip was fried due to unknown causes.

b) Long term response

A typical non-reactive shot has a flat top of about 500 μsec duration. To test the ability of the HP - 450A amplifier to amplify the plateau of the signal without distortion or droop, the following experiment was done.

The input to the amplifier was the output ($\sim 10^{-8}$ amps) of a constant current source. When the source was switched on-off, and the resulting amplifier output viewed on the 565 oscilloscope, it was found that the amplifier output was a flat plateau > 500 μsec in duration.

c) Response to pulse-generator signals and bandwidth determination

Square signals from a commercial (Keithley) pulse generator were fed into the amplifier to see the frequency range over which the amplifier could give undistorted signals could be determined. The HP-450A amplifier gave undistorted output signals up to the frequency limit of our pulse generator, $\sim$1MHz. Using the 40 decibel switch, we obtained a gain of 100. The HP-450A amplifier is an inverting

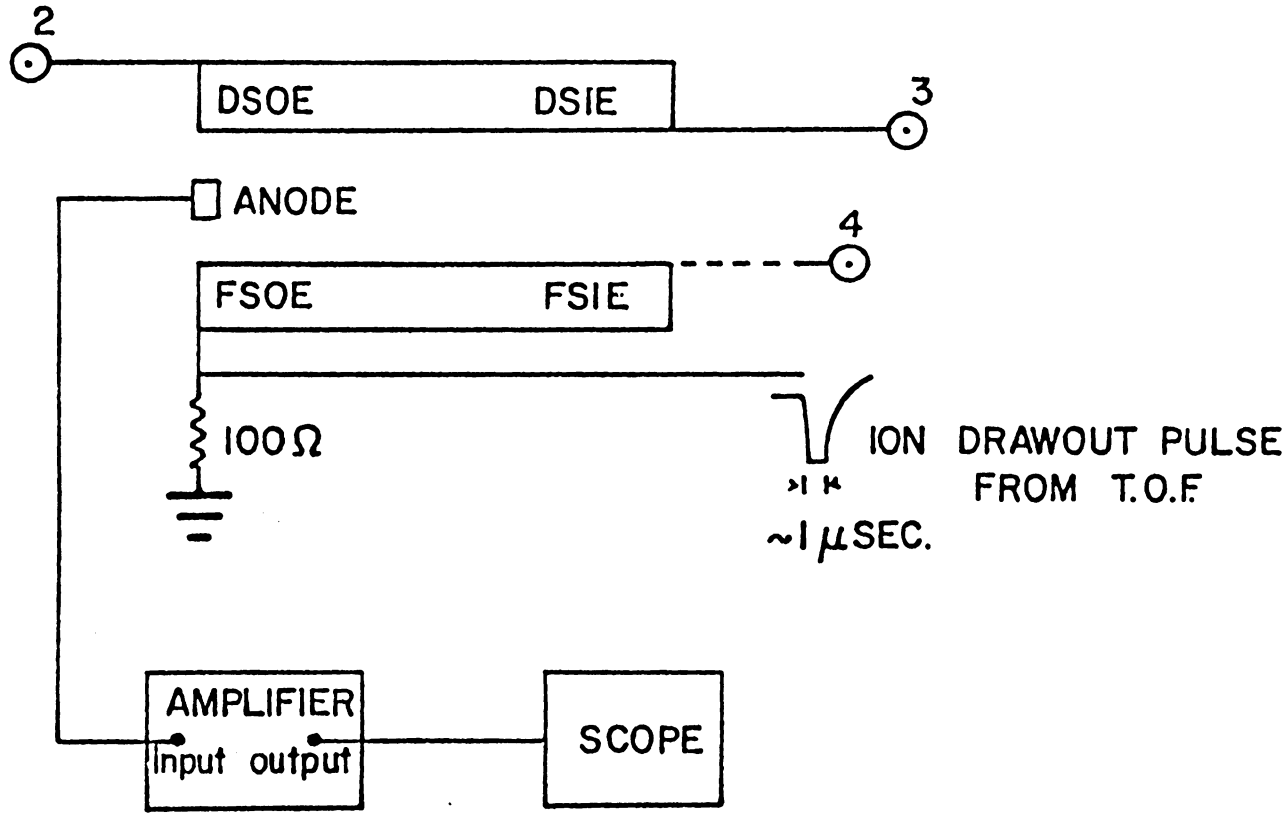

Figure 27. Experimental Set-up for Testing Short-Term Response of Ampliers for Dynamic Shots.

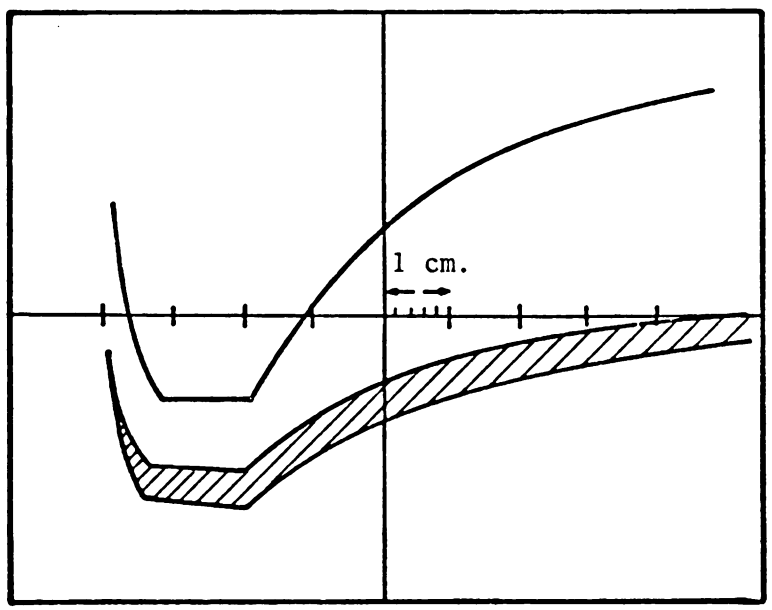

Top curve is the ion focus pulse from the T.O.F. Scope settings were 20 v./cm. and 1 usec./cm. Bottom curve is the response from the HP amplifier. Scope settings were 5 v./cm. and 1 usec./cm. Amplifier gain - 40 db.

Figure 28. Results of Testing HP-450A Amplifier for Short-term Response.

amplifier. Therefore, a signal picture, as it is removed from the Polaroid camera, shows an increasing time axis from left to right, and an increasing voltage axis in a downward direction from the baseline.

D. Non-reactive Studies

In order to test the capability of our apparatus to detect dynamic ion signals, argon shots at a P_1 = 5 torr were fired into the mass spectrometer chamber. Optimized static ion signals were first obtained by leaking argon into the mass-spectrometer chamber via the shock tube . The ion optics were focused by varying each respective lens potentiometer until the magnitude of the ion signal went through a maximum or remained flat. These lens settings were then kept fixed during the firing of shots.

Both the HP-450A amplifier and Galileo electron multiplier can be affected adversely by extreme electron currents. The linear operating range of the electron multiplier is up to about 10^{-7} amps of output current. The limiting value of allowed electron multiplier output current is set by the amplifier requirements. The amplifier, when terminated at the scope by 150 ohms, and operating with a voltage gain of 100, has a maximum output voltage of 5 volts. This corresponds to a maximum input current of about 5×10^{-8} amps, before saturation occurs. In the majority of our dynamic pictures, there was no saturation of either device and therefore the dynamic signals are correct representations of the mass-spectrometer ion current.

It was found that there was a wide variation in ion signal shape during the dynamic sampling. Figure 29a shows one typical shape. At

about t = 160 μsec. there is an abrupt increase in signal which is suggestive of the propagation of the re-reflected shock wave to the endwall. The additional compression and increased density of the gas caused by the re-reflected shock wave (called the "second shock" results in the ion signal change.

Figure 29b shows another non-reactive shot performed under a different ϕ_{EL} setting and resolution setting of the quadrupole. In this figure, the correct (approximately square) shape is obtained; the flat plateau characteristic of a non-reacting species extends over a time period of $\sim$ 150 μsec. This figure also shows an increase in ion signal obtained from the re-reflected shock at about 340 μsec. The leading edge of the signal was omitted by the triggering of the oscilloscope so the sharpness of the signal rise-time could not be verified.

Gutman, Hay, and Sanzone discussed in detail the criteria for judging the goodness of a non-reactive signal. Gutman[28] and Hay[20] judged the performance of their dynamic sampling by the signal risetime, the squareness of the signal, and the constancy of the final high value (signal flatness) obtained. They found that all three criteria could not be obtained simultaneously. At low P_1 (P_1 < 10 torr low T_5 shots, they found poor risetimes, poor squareness, and better leveling; at high P_1, high T_5 shots, they obtained steeper risetimes, better squareness, and poor leveling. Sanzone[4] added these criteria: observation of the "second shock" (i.e., the re-reflected shock wave) must be accompanied by an increase in ion

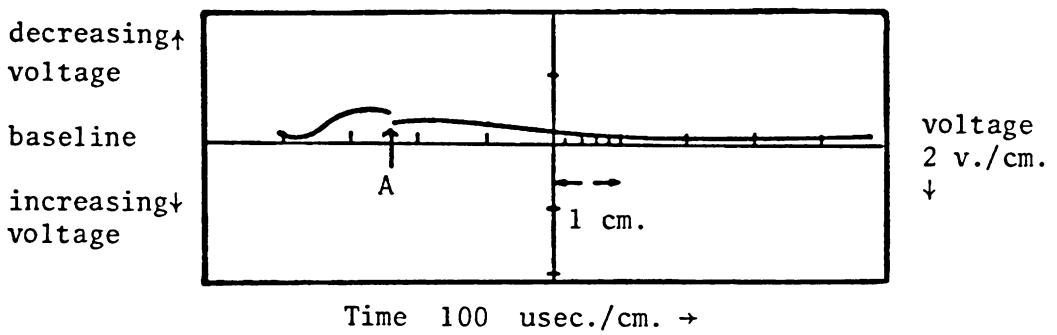

a) The direction of increasing voltage is downward with respect to the baseline. Therefore, an increase in signal height occurs with the appearance of the "second shock" at t ≈ 160 usec. This is labeled by the arrow A. ϕ_{EL} = 225 v.

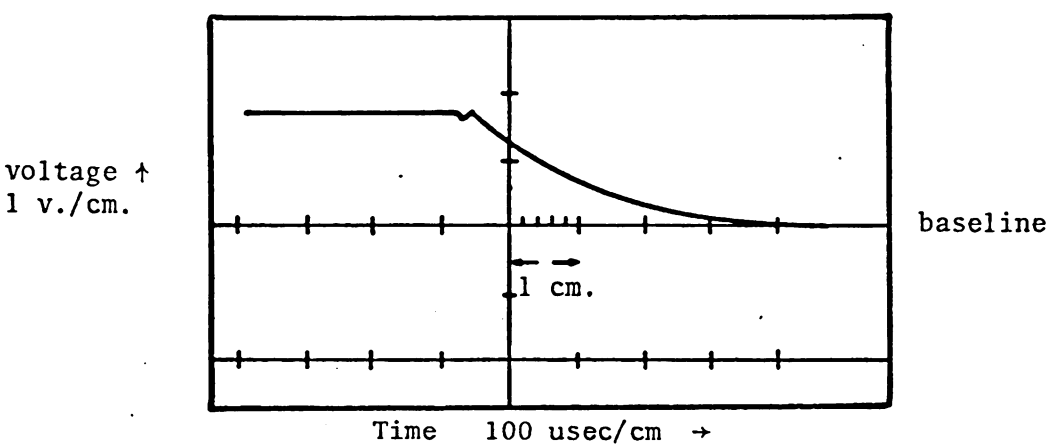

b) The direction of increasing voltage is upward from the baseline. ϕ_{EL} = 163 v.

Both pictures were taken at same settings of ϕ_{IR}, ϕ_{IC}, ϕ_{ER}, ϕ_{MULT} = 1600 volts)

Figure 29. Non-reactive Signal Shapes.

current, the signal risetime must compare favorably with the jet start up time, and the flatness of response should be consistent with non-ideal shock tube theory. Our inability to predict a shock velocity at the endwall and a uniform T_5 from our schlieren measurements made it impossible to compare the experimental flatness of response with that expected from theory. Also, our schlieren results meant that we could not compare the shapes of our ion signals on the basis of constant shock strength. All our non-reactive shots were done using helium as the driver gas; diaphragm breaking pressures were approximately 23 p.s.i. for full petal shots. However, many of our pictures show that the second shock is occurring at two different times even though both shots were carried out at what would appear to be identical flow conditions.

For most of our non-reactive shots, electron multiplier voltages of 1600-1800 volts provided sufficient gain for us to view the signal on the 565 oscilloscope. In addition, due to the limited linearity range of the quadrupole with $p_{\text{shock tube}}$, we could not do non-reactive shots above p_1 = 5 torr.

E. Electron Beam Width

In Gutman's studies[15,28] measurements of electron beam widths were not presented. The width of the electron beam relative to the jet is a crucial parameter for the feasibility of the proposed jet scanning study (this issue is discussed later in Section V of this work). Consequently, the beam width was measured (by two methods) in

this work.

a. The focused electron beam (ϕ_{IC} = 12v., ϕ_{IR} = -37v., ϕ_{ER} = 400v., ϕ_{EE} = 163v.) was passed through a small square of brass mesh mounted on a thin piece of glass. The glass was torr-sealed on the ion repeller at a position slightly before the spinneret leak. It was found that the mesh scattered the electrons so that no trap current was registered.

The experiment was repeated with the trap disconnected and the trap voltage ($\sim$ 40 v.) applied to the mesh. After a 1 1/2 hour exposure time, a dark purple spot of $\sim$0.1" in diameter was burned in the screen.

b. The focused electron beam was deflected by ϕ_{IC} against the shock tube endwall and the dark stripe left by the beam in the vicinity of the spinneret pinhole was measured. The beam width was found to be 0.12" by this method.

F. Jet Risetime Studies

The free jet starting time is a measure of the time for a steady equilibrium jet to be established after the incident shock wave reaches the nozzle throat. The following approximate equation holds at distances greater than four nozzle diameters downstream:

$$\Delta t_{jet} = \frac{0.0152D}{a_s \text{ Tan } \theta_{1/2}} \left(\frac{5.43}{\gamma}\right)^{5/2} \left(\frac{X}{D}\right)^{5(\gamma-1)/2}$$

X = distance of electron gun downstream from orifice

D = nozzle diameter

a_s = speed of sound in the stagnation region = $\left(\frac{\gamma RT_s}{M.W.}\right)^{1/2}$

$\text{Tan } \theta_{1/2} = \frac{D_B}{2X_B}$ D_B, X_B have been defined earlier and are shown in Figure 2.

For argon jets, $\gamma = 1.67$, $\text{Tan } \theta_{1/2} = .365$ and the above formula reduces to:

$$\Delta t_{jet} = .794 \frac{D}{a_s} \left(\frac{X}{D}\right)^{5/3}.$$

Using data from various shock tube-mass spectrometer experiments which used a .002" diameter orifice, a $T_s = T_5$ of 2200°K, and argon as the test gas, Sanzone found good agreement between the experimental starting times and the theoretical ones predicted by the above equation.

We decided to use a pulsed, collimated jet to further test the validity of the above equation for various values of the reduced variable $\frac{x}{D}$. The apparatus used was the Excimer Study Project molecular beam appartus; the design of this equipment is described in the E.S.P. notebooks.[27] Experimental values of Δt_{jet} values were taken for argon at T_s = 298°K, $D_{orifice}$ = .01", and at a x/D range from 34 to 134. Here, we considered x to be the nozzle to skimmer distance rather than the nozzle to electron beam distance.

Figure 30 shows a typical Ar^+ signal during a jet pulse. Δt jet was measured from the photo (#4 of Table 11) as indicated. Typical features of the jet photos are indicated on the photo by letters A-E.

Point A represents the time at which the scope is triggered. The scope

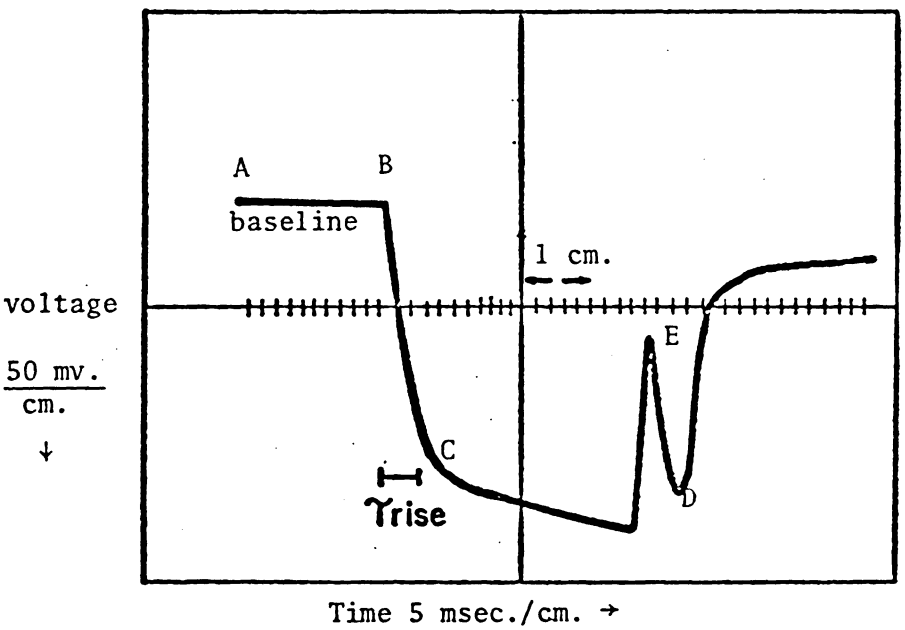

Δt_{jet} = 2.78 msec. A discussion of photo shape is presented in the text.

Figure 30. Ar^+ Signal - Picture 4 of Table 12.

is triggered by the opening of a valve which also controls the release of gas to form the jet. Point B is the time just before the argon reaches the mass spectrometer and is detected. Segment AB, the picture baseline, therefore represents the time of flight of the gas to the mass-spectrometer. Segment BCD, which ideally would be a step function, represents the signal increase as the jet grows and reaches equilibrium. An extrapolation of sigments BC and CD is used to obtain the experimental risetime as shown. Point D represents the ideal time at which the solenoid closes. In reality, a spike forms, and this is thought to be a result of the bounce of the solenoid. This interpretation is reinforced by the observation that slope BC (initial growth in signal intensity from jet formation) is very similar to slope E. Both slopes indicate similar signal increases which result from the initial formation of the jet and its reforming again after the closed valve bounces and reopens.

The experimental data obtained from a series of jet pulses performed at $P_{stagnation}$ = 30 and 55 psi is shown in Table 11, and a plot of the experimental values of Δt_{jet} vs. $\frac{x}{D}$ is presented in Figure 31. It is evident that there is large scatter in the data and that the experimental values do not agree with the theoretical values of Δt_{jet}.

In contrast to the shock tube-mass spectrometer apparatus, the molecular beam apparatus employs a skimmer; it is possible that there is interference of the jet flow by the skimmer and that this affects the formation time of the jet. In using the nozzle to skimmer distance

Table 11

Jet Risetime Data

Picture[a]	Distance nozzle-skimmer (inches)	$\frac{x}{D}$[b]	$\Delta t_{exp.}$ (msec.)	$\Delta t_{calc.}$ (msec.)
1	.654	65.4	3.33	.674
2	.654	65.4	3.11	.674
3	.713	71.3	2.89	.779
4	.713	71.3	2.78	.779
			.706	
5[c]	.83	83	.235	1.003
			.235	
6[c]	.93	93	.588	1.21
7	.93	93	2.12	1.21
8	.93	93	.471	1.21
9	1.029	102.9	.235	1.44
10	1.029	102.9	.353	1.44
11	1.029	102.9	.353	1.44
12	1.129	112.9	.353	1.68
13	1.293	129.3	.353	2.10
14	1.339	133.9	.353	2.23
			1.176	
15[c]	1.339	133.9	.588	2.23
16	----------	omitted	----------	
17	.339	33.9	3.53	.225
18	.539	53.9	3.06	.488
19	.539	53.9	2.12	.488
20	.639	63.9	1.76	.648
21	.739	73.9	.706	.827
22	.839	83.9	.471	1.02
23	.939	93.9	.471	1.23

[a] Pictures 1-17 were at $P_{stagnation}$ = 55 P.S.I.
18-23 were at $P_{stagnation}$ = 30 P.S.I.

[b] D_{nozzle} was .010" for all pictures

[c] Due to difficulties in analyzing a picture, two times were noted

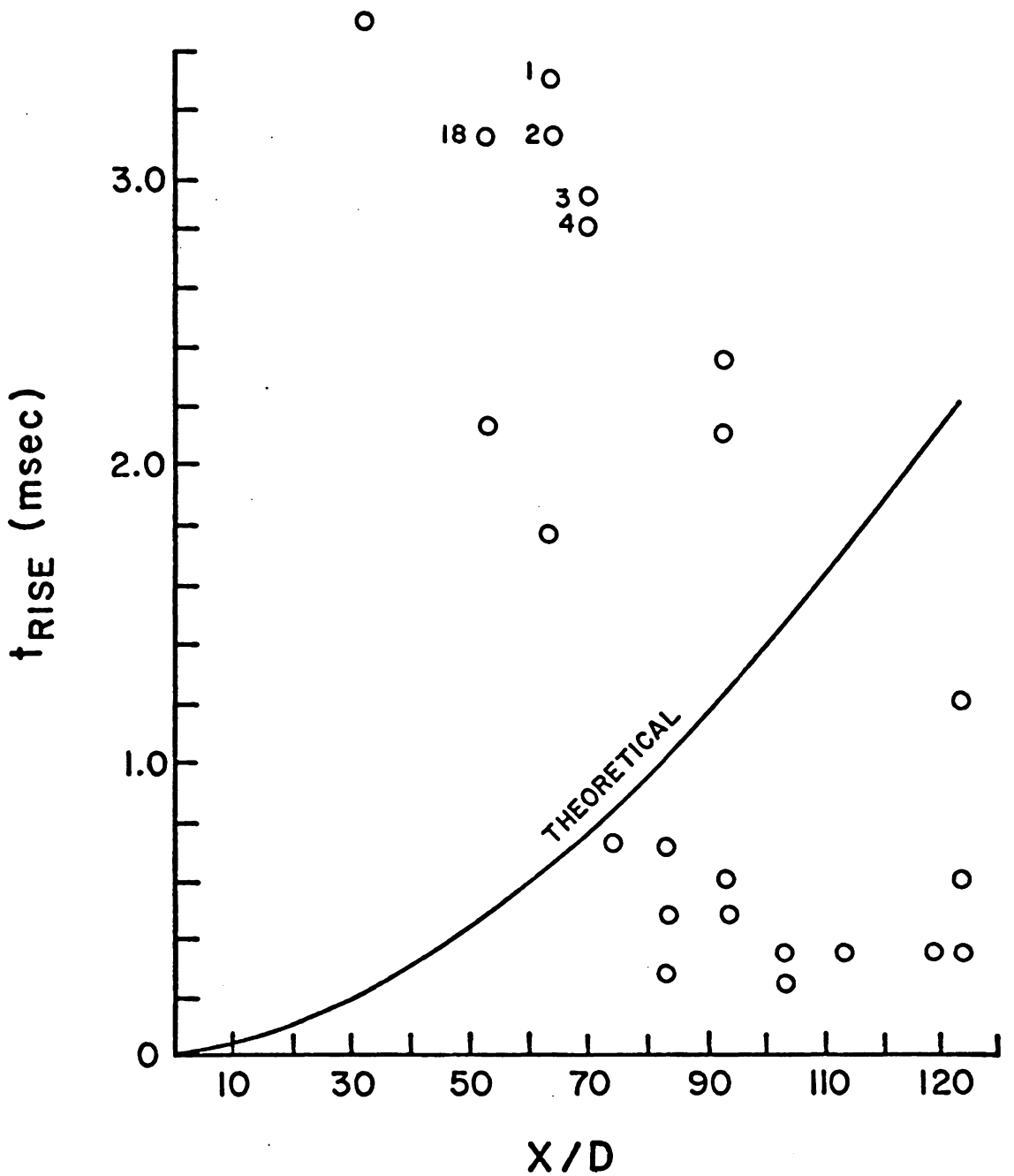

Figure 31. Plot of Jet Risetime Data.

as our x, we assumed that the jet became steady by the time it reached the skimmer; the electron gun on the beam apparatus is far downstream of the skimmer.

Pictures 1-4, 18 had signal shapes which were consistent with the mode of jet formation that was discussed earlier. These pictures were considered to be good and were analyzed further to see if any additional insight into the poor agreement we found between experimental and theoretical risetimes could be found. For pictures 1-4, 18, the ratio $\frac{\Delta t_{jet,experiment}}{\Delta t_{jet,calculated}}$ is:

1	4.9
2	4.6
3	3.7
4	3.6
18	6.3
average	4.6

If a new x is found, such that new x = 2.5 (old x), then $(\text{new } \frac{x}{D})^{5/3} = 4.6\ (\text{old } \frac{x}{D})^{5/3}$, and there would be good agreement between the observed and calculated argon jet risetimes. However, there is no physical significance in the distance 2.5 x (x = nozzle to skimmer distance). It only tells us that our original assumption concerning the choice of x was a faulty one.

Further risetime studies on the beam apparatus are in order to see if conditions exist for which pulsed, collimated jets give experimental risetimes in agreement with the given equation. It may not be

correct to assume that the formation of a pulsed jet is in fact similar to the growth of a jet obtained through orifice flow; in such a case, agreement between experiment and theory would not be expected.

IV. EXPERIMENTAL PROBLEMS WITH THE COUPLED SHOCK-TUBE/MASS-SPECTROMETER TECHNIQUE

Experiments involving the coupled mass-spectrometer/shock-tube system rely on the simultaneous operation of a number of subsystems, all of which must work properly. Some special notes and a few hints about experimental techniques are indicated here in the hope that other students will benefit from them.

A. Diaphragm Scribing

In using the precision scriber, it is essential to tighten all four bolts evenly so that both axes of the cross design are cut to the same depth. The hexagon should be placed in the scriber with the grain on the diagonal so that both cuts are identical. Any burrs on the inner surfaces of the scriber or metal chips trapped about the point can contribute to poor cuts. Occasionally, the scriber point may have to be sharpened on a lathe if (the Unimat lathe is useful for this) the diaphragms begin to break poorly.

B. Schlieren Measurements

The use of the centering tool (see Figure 32) facilitates finding the centerline of any (round) shock tube. In lining up the schlieren system, the photomultiplier box should be placed as far as possible from the last schlieren mirror; the longer the distance, the greater the deflection of the light across the aperature of the box. Therefore, signal blips of higher amplitude are obtained. During a series

Figure 32. Tool for Locating the Shock Tube Centerline for Adjustment of the Schlieren Mirrors.

of shots in which the shock wave is made weaker by having a greater proportion of the driver mixture composed of argon, it may be necessary to adjust the position of the light beam on the razor edge to compensate for the smaller deflections. Similarly, intermittent changes in noise levels from the output of the photomultiplier box may call for more or less light going into the box. Trigger levels of the scope should be checked prior to every shot.

C. The Electron Gun

For the sake of reproducibility, one would like to be able to keep the gap settings on the electron gun as they were before the filament needed to be changed. The easiest way to do this is to loosen the electron lens, slip the new filament into place, and reset the repeller-lens gap and the lens-housing gap with a feeler gauge. A hole bored into the chamber wall makes it easier to slip in an allen wrench to loosen the filament.

The problem of having the gun elements create shorts with the filament is always a problem and is aggravated when the gaps are small. Resistance checks can be made prior to the gun's insertion into the mass-spectrometer chamber; however, a lit filament may get hot enough to sag and cause shorts whereas the cold filament did not. Having shorts occur in the middle of an experiment is quite frustrating; usually it is difficult to repair the problem while the gun is still in the mass-spectrometer chamber; it is very easy to break the filament, particularly if it has been in use and is already somewhat

brittle.

It is also important to keep the gun elements clean. A dirty gun can cause the trap current to oscillate or can create unproducible levels of trap current (for the same power supply settings) over a period of time. In such a case, the gun parts can be put in an ultrasonic cleaner; the walls of the ionization chamber can be cleaned with a fiberglass pencil.

The alignment of the electron gun in the mass-spectrometer chamber is a rather crude operation. First, the gun's height must be aligned so that the axis formed by the electron beam is slightly below the spinneret hole. Second, the alignment of the electron gun to be parallel to the shock tube endwall requires adjustment by means of one large bolt, and it is difficult to get precision movement of the housing by such adjustment. Third, the ion optics must orient directly under the entrance ring to the quadrupole, and this requires careful torqueing of the brass plate to which the gun is attached. The plate can be first adjusted by finger-tightening of the bolts. All of the alignments mentioned above must be done by eye, and it is a tedious operation to insert the gun into and extract it out of the system during the alignment process.

D. The Quadrupole

Alignment of the quadrupole can in the chamber requires the trial and error adjustment of cams so that the entrance ring of the quadrupole is located parallel to the vertical centerline of the

shock tube endwall. This step can be made easier by inserting a thin rod in the entrance ring and then sighting its position relative to the shock tube endwall.

We found that trap current was affected adversely at various Fluke voltage levels; apparently the quadrupole voltages were interacting with the electron beam. To remedy this, a copper "doughnut" was put about the entrance ring of the quadrupole to shield the poles. The trap current then remained constant for a given set of electron gun power supplies and was independent of ϕ_{FLUKE}. The copper doughnut, which is at $\phi_{I.E.}$, must be kept away from the ion optics (lens 9 in particular) and the electron gun housing to prevent shorts from happening.

The pole faces of the quadrupole can be cleaned with a fiberglass pencil.

E. The Quadrupole Oscillator

The R.F. oscillator is an extremely tempermental piece of equipment. When mass-spectrometer work began in our lab, the oscillator was not functioning at all. We could not get balanced, undistored sine waves as signal outputs, nor was there sufficient ϕ_{AC} or ϕ_{DC} to do any mass scans of interest, in the mass range of 20-50. The instrument had to be virtually rebuilt to satisfy the electronics requirements needed to get spectra with apex resolution.

The electronics of the oscillator presents special problems:

a) The output of the oscillator is extremely sensitive to

capacitive loading. Anything affecting the equivalent capacitance of the poles (such as dirt) will also affect ϕ_{AC} and ϕ_{DC} adversely. The capacitance of the coax cables leading to the pole system is also important; the length of the cables was carefully matched so that the signals sent to each pair of poles remained matched and undistorted.

b) The amplitudes of ϕ_{AC} and ϕ_{DC} is affected by vacuum conditions. Any testing of the oscillator output (while signal is being applied to the poles) should be done under vacuum, at least under mechanical pump roughing. Otherwise, ionization of gas by the applied R.F. voltage may result in a collapse of the sine waves.

c) Any checking of ϕ_{AC} or ϕ_{DC} levels should be done with a volt-ohmmeter of relatively high impedance characteristics. Use of a conventional (20,000 ohm/volt) device (see Table 12) gives false (too low) readings.

Table 12. Calibration Data on ϕ_{DC} for Various Voltmeters

This data shows the discrepancies in measuring ϕ_{DC} using different voltmeters. In locating masses on a spectrum, one usually sets the ratio $R = \frac{2\phi_{DC}}{\phi_{DC}}$ by measuring ϕ_{AC}, ϕ_{DC} at a specific Fluke voltage (usually, R is set for apex resolution, about 0.33) and then dials in (with the Fluke power supply) the ϕ_{DC} needed to isolate a specified mass, M/q. Any errors in reading ϕ_{DC} can affect the reproducibility of pinpointing a specific peak. The error in reading ϕ_{DC} is more apparent at low ϕ_{DC} values, for the Simpson meter.

ϕ_{AC} peak to peak	ϕ_{DC}, Simpson meter[a]	ϕ_{DC} Digital meter	ϕ_{DC} high-impedance meter[b]
100	+ 3.7[c]	7.0	6.8[c]
200	14.0[c]	16.4	16.1[f]
300	22.5[c]	25.8	26.0[f]
400	30.0[c]	35.0	35.0[g]
500	39.0[c]	45.5	45.5[g]
600	57.0[d]	55.4	56.0[g]
700	67.0[d]	65.0	66.0[g]
800	77.0[d]	74.7	76.0[g]

[a] (20,000 ohm/volt)

[b] (1 megaohm/volt)

[c] Values read on 50 volt scale

[d] Values read on 250 volt scale

[e] Values read on 10 volt scale

[f] Values read on 30 volt scale

[g] Values read on 100 volt scale

V. CONCLUSIONS AND RECOMMENDATIONS

A. Technical Suitability of the Present Apparatus for Reactive Studies

1. Schlieren System

In any shock tube experiment, the interpretation of rate constants and calculation of activation energies is dependent upon an accurate determination of the gas temperature in the shocked region. The measured experimental parameter, the incident shock velocity, must consequently be obtained with reasonable accuracy which in this study had to be provided by schlieren measurements.

For our present experimental apparatus, a severe restriction upon the feasibility of reactive studies is that of our uncertain schlieren data. That is, the next phase of experimentation will require a more reliable velocity measurement. Our present data indicate variations in shock speed between successive mirror stations of greater than 50% in many cases. In fact, our data are so erratic that the shock wave velocity cannot be extrapolated to endwall conditions. A knowledge of the shock conditions at the endwall would be essential for determining the criteria for specifying the nature of the jet flow through the orifice. An acceptable error in the shock speed variation would be on the order of a few percent; typical data from another lab varied about 0.3% between mirror stations for a single shot.[29] In a sense, this is nothing but a trivial technical problem with the present apparatus, but I recommend that the next phase of work with this tube start with immediate attention to this problem.

For duplicate shots performed under identical operating conditions, an acceptable error bar in the temperature is about $\pm$ 100°K.[30] Here, the limiting factor is the variation in the breaking pressure.

For a representative shot of Mach # (M_1) = 3, and incident shocked gas temperature (T_2) of 1100° $\pm$ 100°K, the corresponding error in incident shock velocity would be found as follows:

$$T_2 = \frac{2\gamma M_1^2 - \gamma - 1}{\gamma + 1}\left[\frac{(\gamma-1)M_1^2 + 2}{(\gamma+1)M_1^2}\right] T_1$$ (Equation 2.31, 32, Greene and Toennies)

$$M_1 = \frac{u_{shock}}{\left[\frac{\gamma RT_1}{M.W.}\right]^{1/2}}$$

T_1 = temperature of unshocked gas = 300°K

$\gamma = c_p \backslash c_v$ = 1.67 for argon

$$\Delta T_2 = \left.\frac{\partial T_2}{\partial M_1}\right)_{\gamma, T_1} dM_1$$

$$\frac{\Delta T_2}{\left.\frac{\partial T_2}{\partial M_1}\right)_{\gamma, T_1}} = dM_1$$

$$dM_1 = \frac{\Delta T_2}{\left(\frac{4\gamma M_1}{\gamma+1}\right)(T_1)\left[\frac{(\gamma-1)M_1^2+2}{(\gamma+1)M_1^2}\right] + T_1\left[\frac{\partial \gamma M_1^2 - (\gamma-1)}{\gamma+1}\right]\left[-2\,\frac{2}{\gamma+1}\,M_1^{-3}\right]}$$

$$= \frac{100°K}{\left[\frac{4(1.67)(3)}{(2.67)}\right](300°K)\left[\frac{(0.67(9))+2}{2.67(9)}\right] + 300°K\left[\frac{(2(1.67)9)-.67}{2.67}\right] -2\left(\frac{2}{2.67}\right)\frac{1}{27}}$$

$$= 0.176$$

$$M_1 = u_{shock} / \left[\gamma RT_1/M.W.\right]^{1/2}, \quad \left[\gamma RT_1/M.W.\right]^{1/2} \text{ is a constant}$$

$$dM_1 = \frac{du_{shock}}{\left[\frac{\gamma RT_1}{M.W.}\right]^{1/2}} = 0.176$$

$$du_{shock} = 0.176 \left[\frac{\gamma RT_1}{M.W.}\right]^{1/2}$$

$$= 0.176 \left[\frac{1.67 \times \frac{2 \text{ cal}}{^\circ\text{Kmole}} \times 300^\circ\text{K} \times \frac{4.18 \times 10^7 \frac{\text{gcm}^2}{\text{sec}^2}}{1 \text{ cal}}}{40 \text{ g/mole}}\right]^{1/2}$$

$$= 0.176 \left[.324 \frac{\text{mm}}{\text{usec}}\right]$$

$$du_{shock} = \pm 0.057 \text{ mm/usec}$$

Therefore, an acceptable error bar in the measurement of incident shock velocity for duplicate shots is $\pm$ 0.057 mm/usec. This is about a 6% error for a typical Mach 3 shot. The errors are in our present velocity data (between stations) for a single shot is far greater than this error.

It is obvious that our schlieren system is in need of improvement to get shock speeds within the expected error ranges. Some modifications in the present design of our schlieren set-up are presented in Section B, with the expectation that the sources of our unreliable data can be eliminated.

2. Mass-Spectrometer

The signal-to-noise ratio in our dynamic shot pictures appears to be quite good. Any of our dynamic (non-reactive) signals could be

amplified more without the noise levels becoming unduly large.[30] For reactive experiments in which levels of reactant are highly diluted in the test gas mixture, there are several ways to improve the efficiency of ion collection in our system (this topic is discussed in the next section). The output current of our multiplier in such a case could be reduced by operating the multiplier power supply at very low gain ratings; it is likely that the multiplier could become saturated otherwise.[30]

Unfortunately, there are no reliable figures for the sensitivity (amps/torr) ratings of our instrument. As discussed in the next section, our present experimental set-up does not allow us to get a figure for the average pressure in the ion source. However, our dynamic (non-reactive) pictures support the viewpoint that the signal to noise ratio is adequate.

3. The Electron Gun

For any experiments involving the ionization of the jet emerging from the shock tube orifice, it is essential that the electron beam be of a specified diameter relative to the jet size. This implies that the beam should be placed at a position downstream from the orifice such that two opposing factors are optimized:

(1) The beam should be placed close enough to the orifice so that the jet risetime is small compared to the overall test time, (also, closer sampling positions favor high signal to noise ratios since the jet density falls off with increasing distance from the orifice) and (2) The beam should be far enough away from the orifice

so that large jet diameters can be expected. This consideration is essential for experiments (such as the original proposed study) in which scanning of the jet diameter is to be performed. In such a case, it is desirable that the electron beam width is less than the jet diameter at the sampling position. An alternative method of obtaining a larger jet diameter for a given sampling position is to increase the orifice diameter, but of course, this will affect the test time adversely due to the increased mass flow.

The size of our present electron beam (0.06" - .1" diameter) at a sampling position (x = 3.5 mm) which permits an acceptable jet risetime[a] of about 30 usec (test time of the experiment is ∿500 μsec.) to be obtained is adequate for studies which involve bulk ionization of the jet cross-sectional plane. These experiments would be similar in nature to the ones performed by Gutman[28] and Hay[20]. At the sampling position, the jet size is about the same as the beam width.[30] Consequently, there is little chance of scanning the jet structure <u>in detail</u>. (Some coarse features of the jet structure might, of course, be scanned with this sort of broad beam). It was for this reason that the present work became a characterization study of the shock tube-mass spectrometer apparatus.

---

[a] $\Delta t_{jet} = \frac{0.795D}{a_5} \left(\frac{x}{D}\right)^{5/3}$

D = leak diameter = 0.004"

$a_5 = \left(\frac{\gamma RT_5}{M.W.}\right)^{1/2}$

x = sampling position downstream from orifice = 3.5 mm

Some estimates regarding the gun design for obtaining more narrow beam widths are presented in Appendix H.

B. Recommendations for Improvements for Future Experimental Studies

If our apparatus is to be employed at some future time for experimental work, it may be helpful to point out some of the design changes that will have to be made (at some considerable expense) to improve the apparatus and its operation. For the benefit of future workers, I give here some recommendations.

1. Schlieren System

The schlieren system at present needs to be further tested to discover and eliminate the source(s) of the erratic shock wave behavior we observed. Failing this, a different kind of velocity probe must be employed.

a) Electronics

One problem occurring during the operation of the schlieren electronics was that of uncertain triggering. Instability of the oscilloscope could cause problems in triggering, especially since the size of the schlieren blips for most of the pictures obtained were small.[30]

Any unreliable triggering can create problems in interpreting a schlieren picture. If the assignment of first schlieren blip is uncertain, one cannot be certain if a measured time interval corresponds to the distance between mirrors 1 and 2 or some other mirror distance. An error in the calculation of shock speed will result,

particularly because in our system, the mirror intervals were not of the same length.

Our oscilloscope ought to be thoroughly checked and brought up to standard specifications by Tektronix, in the event that some electronic components deteriorated over a period of time.[30] In any event, I recommend that a separate external circuit, such as a Schmitt trigger box, be used to convert the first schlieren output signal to a trigger pulse of constant shape and size.[30] One type of Schmitt box is reported elsewhere [50] and might be tested on our system. Another method of triggering the scope would be to use a dual schlieren set-up. A single mirror station created by the addition of a separate pair of mirrors for triggering the scope would be used. In this design, the scope is triggered by a signal created by a separate laser, pair of mirrors, and photomultiplier box. The signals from mirror stations 2 and successive stations come from another schlieren set-up further downstream the tube which utilizes its own separate laser and photomultiplier box.

There are several advantages of using a single station for triggering purposes.[30] Initially, one could use the single station to determine what conditions are needed to obtain unambiguous triggering. One could also check if any non-uniform flow patterns (such as multiple waves) were set up after a shot was fired to cause multiple signals to appear on a schlieren picture. After the single station was found to work properly, the other stations could be added one at a time. With each addition, the signal output could be checked and the shock speed calculated. After the addition of three

or four intervals, one would know if the shock speeds were essentially constant.

In any schlieren experiment, the proper propagation of the shock wave is important; it is essential that the condition of limiting flow is reached. In this condition, the shock wave velocity becomes essentially constant and the gas properties in the shocked region are uniform. To check the performance of the shock tube, a good quality (Kistler, for example) pressure transducer could be fitted on a temporary endplate both at the usual endwall site and at a position at the end of the first glass section.[30] In such a way, any deviations from normal shock wave propagation can be isolated.

The use of pressure transducers in shock tube work is a standard method of checking flow properties. In the event that the diaphragms are breaking irregularly, the driver gas is channeled through a constantly widening nozzle. The slow opening of the diaphragm creates several pressure waves which may eventually coalesce with the shock wave, but which in the meantime create erratic shock velocities. A pressure transducer is able to detect any multiple pressure pulses occurring outside the shock speed measurement section; therefore a check on the diaphragm performance is obtained.

It should be noted that some experimentalists make use of transducers as another method of obtaining incident shock wave velocities. Skinner[31], for example, uses three SLM Model 603 transducers spaced 75 cm apart near the downstream end of a shock tube to permit measurements of shock attenuation. Kistler Instrument Corporation

makes a series of quartz "Quick Change" pressure transducers which are designed for use in shock tubes. One model, 211B5, would be suited for chemical shock tube work. It features a pressure response range up to 100 psi, with a sensitivity of 50 mv/psi with an output linearity of $\pm$ 1% and a 2 usec risetime. The transducer with accessory nuts and seals is currently sold for $390.00 each; the transducer is designed to be used with a coupler (model 549) at $140.00 each, and a cable at about $20.00 each.

b. Gas Mixtures

Another possible source of erratic shock wave velocity that we should check is that of the composition of the driver gas. In the past, our driver gases, argon and helium, have been mixed as they flow into the driver section with the lighter helium being admitted first. In the event that the driver gas was not completely and uniformly mixed, it is possible that erratic shock propagation could result[30]. The velocity of the shock wave is a function of γ (c_p/c_v) and molecular weight of the driver gas. In the case of a non-uniform mixture, γ and molecular weight would be time-dependent functions of the gas composition and therefore, variations in the shock speed would result.

Single-component driver gases should be used until all the sources of erratic shock velocity are checked out. However, our scribing method is such that the use of pre-mixed gases would be advisable. Our diaphragms are scribed to break at a constant value of pressure, about 23 p.s.i. Therefore, we vary the shock wave velocity range by varying the composition of driver gas; the higher the percentage of

helium, the faster the shock wave passes down the tube. The use of commercial pre-mixed gases could be used to check the constancy of the shock wave velocity over a wide range of values. Linde, Inc. for example, custom blends of argon in helium (0.1-50% argon) at prices ranging from \$77.00-132.00 per cylinder (309 ft^3) currently. However, we could possibly mix the gases in our sample tanks and use heating tape to heat the contents for thorough mixing.

As a last resort, the design of the shock tube itself might have to be evaluated. The interior of the tube is noticeably irregular and that this might induce undesirable turbulence in the flow.[30] Another item to check would be the uniformity of the tube diameter.[30] At the present time, our schlieren data is far too irregular to permit us to construct a wave diagram of the flow features, but when the sources of the schlieren measurement problems are eliminated, this could eventually be done. In such a way, one could gain some insight into any basic flaws in the shock tube design. For example, a too-short driver section could cause rarefaction waves to cause rapid deceleration of the shock wave to occur.

It cannot pinpoint any one source of error which is influencing the data. For an example, the zig-zag pattern of our plotted data could be attributed to a misassignment of the time intervals of a schlieren picture.[30] However, this would mean that a consistent variation in the ratio of shock speeds for successive intervals would be obtained; this is not true for our data. Similarly, a non-uniform driver gas mixture in itself would not lead to the large fluctuations

in shock speed that we observed.[30] Nevertheless, the problems with the schlieren data can be traced step by step.

c. Diaphragms

The development of proper scribing technique and proper choice of material is essential when testing diaphragm performance in shock tube work.[29]

The diaphragm scribing machine first should be checked for consistency of scoring the metal.[30] Inspection of the scored diaphragms under magnification would give insight into the quality of the cutting, i.e. whether the cuts are jagged, or of non-uniform thickness or depth. It is also suggested that another type of diaphragm material might be tested on our system.[30]

There have been a few recent studies of diaphragm bursting processes which give insight into the scribing techniques and the material properties which lead to successful diaphragm performance. Rothkopf et al.[32] made a detailed experimental study of the diaphragm opening process for various types of diaphragms. In addition, they performed experiments using two scoring methods to scribe the metal: (1) a press was used to stamp an "x" into the metal, using a constant force to press the x design into the metal, and (2) a crossed knife blade installed in the shock tube cut the diaphram automatically while a shot was fired.

Rothkopf et al.[32] found that aluminum metal (scored with the press) broke most ideally with little initial bulging into four

petals. Copper and brass diaphragms, on the other hand, tore along one slit first and consequently had diaphragm opening times which were far longer than the essentially instantaneous breaking of the aluminum material. In addition, the copper and brass bulged strongly before tearing occurred. The conclusions for the diaphragm materials was the same for the knife blade scribing technique. These results indicated that more ductile materials (e.g. brass, copper) produced less satisfactory opening time.

Rothkopf et al.[32] also found in carrying out duplicate sets of experiments on both round and rectangular shock tubes, that the square shock tube (45 mm hydraulic diameter) allowed faster diaphragm rupture. However, larger round tubes gave diaphragm opening times equivalent to square shock tubes of same hydraulic diameter $\frac{4A}{C}$ (A = area, C = circumference).

Wachli[33] made an extensive study of the diaphragm rupture process for three different materials. Mylar film (similar to cellophane) untempered aluminum, and Hycar (rubber-coated nylon) as a function of driver fill rate. His experiments utilized schlieren photography of the flow patterns which developed after rupture of the diaphragm occurred. By simultaneously analyzing the pressure distributions in the flow as a function of time, he was able to gain insight into the nature of the rupture for each type of material.

Mylar material of two thicknesses (0.002" and 0.004") were unscored when ruptured. The 0.002" thick material tore along a circle starting at the center and allowed more and more gas to escape as time progressed. Consequently, the rupture was very non-ideal (i.e.,

non-instantaneous). Using two driver fill rates of about 0.007 and 0.035 lbs. of nitrogen per second, it was found that a double pressure jump occurred at about 425 usec. after the diaphragm began to tear for the fast fill rate. The behavior of the 0.004" Mylar diaphragm (formed by sandwiching two 0.002" films together) was similar to that of the 0.002" thick film.

The rupture of the aluminum diaphragm (0.025" thick) was found to be a strong function of driver fill rate, probably because it is less elastic than Mylar and had been scored (depth .02") with an x pattern. The rupture occurred first at the central point of the x. As the center hole enlarged, more and more gas rushed through the opening. Consequently the higher the fill rate, the faster the central hole enlarged. Compared to the mylar diaphragm, the breaking of the aluminum diaphragm to a wide open position took longer; however, the Mylar film appeared to initially open quickly and continued to stretch open slowly.

The unscored Hycar material (0.016" thick), in contrast to the Mylar film, broke quickly through a large central hole and any residual material flapped easily aside after the break occurred. Consequently, there was an absence of turbulence and shock patterns which were induced by the more non-ideal Mylar rupture. Wachli concluded therefore that Hycar is a better choice of material than the standard Mylar and aluminum; Hycar appeared to perturb the flow field less upon rupture.

It is evident from these studies that the process of diaphragm rupture is a complex matter. If we were to further test different

diaphragm materials on our system, it would be interesting to try Hycar material and see if any improvement in shock wave behavior occurred. Alternately, we could attempt to break our present aluminum material at higher driver fill rates to see if the expected faster opening time would improve the shock wave characteristics. One obvious advantage of using unscored material, however, is that one extra variable, the uniformity of cut, is eliminated as a possible source of problems.

2. The Mass Spectrometer

There are several ways to improve the operation of our quadrupole mass spectrometer.

Good sensitivity of a quadrupole is attained by focusing the ions into the entrance of the quadrupole as close as possible to the central axis and to collect ions with small transverse velocities into the quadrupole entrance.[29] In our system, ions emerge through the ion source into a cylindrical lens system of substantial length (about 2") before they even reach the quadrupole entrance. Furthermore, any small misalignment of the ion source means that ions can be off-axis when they exit the last lens. This could cause an apparent lowering of ion signal. One way to remedy this situation would be to use a commercial quadrupole lens to aid in directing the ions near the quadrupole axis.[29] Another method, used by Hay,[20] involved the use of a larger diameter quadrupole entrance to improve sensitivity. It is also important to control the collection of ions which exit the quadrupole structure and enter the detector. Close placement of the

detector to the exit aperture aids in reducing the proportion of ions which miss the detector. The cyclic motions of the ions leaving the quadrupole (due to the changing phase of the R.F. voltage) would otherwise lead to a loss of sensitivity. Our electron multiplier has a high (>1000 V.D.C.) grid voltage which attracts ions and helps to prevent ion collection loss.

Due to the fact that the ionization chamber of our ion source is rather large, it is possible that a sizeable portion of ions are lost to the background and never reach the exit slit of the ion source for subsequent collection into the quadrupole. A possible improvement in the design of our ion source, that of creating a more well-defined ionization region, would isolate the location of the ions and permit them to be created closer relative to the mass-spectrometer entrance.

One course of uncertainty in the measurements of sensitivity that can be done for the present quadrupole set-up lies in the fact that only the bulk pressure of the mass-spectrometer chamber can be measured rather than the pressure within the ion source. Our chamber presently has one ion gauge located far above the ion source. For further measurementsof amps/torr ratings, it would be helpful to have an ion gauge located near the ion source, so that true ion source pressures, rather than background gas pressures could be obtained.

Some suggestions regarding the improvement of the resolution of the quadrupole can be outlined. The ion energy of 200 volts is rather large, particularly because the cylinder housing the

quadrupole is rather short (about one foot long).[30] Consequently, ions transit the pole structure fairly rapidly and a loss in resolution is obtained. Typical ion energies in mass spectrometer analysis are on the order of 50 volts. It might be worthwhile to see if any improvements in peak width and shape of spectra are obtained for lower ion energies.

3. The Electron Beam

For any proposed experiments in which ionization of a jet is performed by an electron beam, it is quite important to maintain a sufficiently well controlled and stable alignment of the beam.[29] In this way, a defined area of the jet can be ionized in a reproducible manner.

The buildup of stray charges inside the ion source can cause the beam's position to fluctuate. The presence of insulating surfaces created by organic deposits inside the ion source can cause a buildup of charge which affects the beam's alignment adversely.[29] It is essential, therefore, to remove any organic contaminants from the vacuum system.

Some sources of problems include traces of pump oil which can form polymerized layers on the metal surfaces of the course, metal oxide formation on the source itself, and possible contaminants from the degassing of O-rings which could be introduced into the system. At the present time, our mechanical pumps on the shock tube are untrapped. The use of molecular sieve foreline traps would greatly reduce the possible introduction of pump oil vapor into the vacuum

system.[30] One suitable model is the NRC 345 foreline trap. It features a molecular sieve of 10°A pore size and heating mantle for bakeout purposes. The trap, which is currently priced at $260.00, is designed so that the pumping speed is virtually unchanged by its addition to the vacuum system. The outgassing of O-rings could be reduced by using O-rings of inert material such as Viton; the less expensive buna-n rubber O-rings which are commonly used would not be as suitable a choice. The removal of metal oxide and other surface contaminants on the ion source itself could be checked by regular cleaning of the source (the use of an ultrasonicator and fiberglass pencil would be needed here.)

If more stringent precautions were necessary regarding the vacuum system, then cryopumping would be suitable for reducing the level of impurities. Beske, et al.[34] used a cryopump with liquid helium as the freezing agent to decrease the pressure in the vacuum chamber to less than 10^{-8} torr. In particular, the author sought to remove high partial pressures of O_2, N_2, and H_2 from the ion source chamber. Noller[36] discusses some of the general vacuum system design considerations when cryopumping is used for applications involving rarefied gas flow.

The design considerations involved in creating an electron gun with a narrow beam width for the proposed experiment we originally planned are not easily satisfied.

The use of magnetic collimation to reduce defocusing of an electron beam is commonly used in mass-spectrometer ion sources. If

charged particles have velocity components both parallel and perpendicular to the magnetic field in which the particles are moving, the net motion of the particles will be helical.[36] (The parallel velocity component will be unchanged by the magnetic field; this will cause a linear drift of the particles. The effect of the magnetic field upon the perpendicular velocity will result in circular motion). The electron beam which is emitted parallel to the field is thus prevented from diverging because any drift in motion perpendicular to the field results in circular motion about the beam axis.

However, the use of magnetic collimation in experiments involving a quadrupole mass spectrometer is a questionable one. The magnetic field can adversely affect the operation of the quadrupole by changing the ion paths at the quadrupole entrance or within the pole structure.[29] For this reason, Gutman[28] rejected magnetic collimation as a focusing aid in the design of his electron gun. (Care must also be taken that the ion source material is non-magnetic; any extraneous fields can affect the quadrupole operation).[29] In contrast, the use of magnetic collimation is a fairly common practice in time-of-flight mass spectrometers[37]. Consequently, it would be worthwhile to investigate the use of the T.O.F. instrument for a coupled shock tube/mass-spectrometer experiment in which a narrow electron beam would be needed. [In addition, the T.O.F. instrument has the added capability of being able to analyze several mass peaks simultaneously. This is a real advantage in reactive studies where it is desirable to follow the concentrations of several reactants and products with time.]

The use of high electron beam energies as a method of reducing space-charge defocusing also has inherent problems. It is difficult to handle high energy beams in a vacuum system. Robben[38], for example, using an electron energy of 27kv, found problems with arcing that made the operation of his gun highly tempermental. Our system has the added complication that the ion trajectories could be influenced adversely by the high electron energies. The use of high energy beams also increases fragment ion production and affects ionization cross sections.[29]

Therefore, the use of high energy beams has serious implications for reactive studies in which the concentration of a particular species is monitored.

In order to gain some insight into the design considerations needed to produce an electron gun for our proposed experiment, the following tentative specifications were sent to several manufacturers involved in mass-spectrometer work:

Pressure of mass-spectrometer (quadrupole) chamber during gun's operation:	10^{-5} - 10^{-6} torr
Electron beam width:	0.006 - 0.010"
Electron beam trap current:	10-20 microamps
Filament:	must withstand cycling to atmospheric pressure
Electron energy:	if possible, to avoid high-voltage effects in vacuum, it would be desirable to keep the electron energy at about 100 volts.

Varian[39] and Perkin-Elmer[40] did not have any commercial units in stock with the desired specifications, and Perkin-Elmer did not have the capability of designing a special gun with the above properties. Cliftronics[41] replied that magnetic collimation would be necessary, and that higher electron energies would also be needed.

It should also be mentioned here, that the design of an electron gun for use in our quadrupole chamber demands some other special requirements not listed above which are based on the geometry of our experimental set-up. The sampling of ions in our system is perpendicular to the jet flow. Therefore, any new gun design must require that the ions be repelled upwards into the quadrupole. The quadrupole entrance is presently located several inches above the centerline axis of the jet flow through the pinhole leak. Consequently, provisions must be made in any new gun's design for the ions to be accelerated through a fairly long distance into the quadrupole without substantial loss of ions.

C. Future Experiments for Sampling Jet Flow

Progress has been made in resolving some of the problems associated with the mass-spectrometric sampling of shock tube flows. A new technique for the continuous mass-spectrometer analysis of shocked gases has been recently reported by Krizanic et al.[42]. In this method, the shock tube and mass-spectrometer are coupled at right angles rather than in the usual linear configuration. The shocked gas flows through an orifice into a vacuum chamber and forms a free jet. The jet is skimmed and the jet core of hot, shocked-

treated gas forms a supersonic molecular beam in another evacuated chamber. A portion of the beam is then ionized and accelerated into the time of flight mass spectrometer.

This method has several advantages over the conventional coupled shock tube/mass spectrometer technique: (1) the use of a skimmed molecular beam helps to eliminate the sampling of gas which may have been affected by the thermal boundary layer. (2) Pressure buildup in the mass-spectrometer is lessened by allowing only a very small fraction of the beam to enter the mass-spectrometer. Therefore, one has the ability to sample shocked gas for longer time periods than in the conventional method.

Nevertheless, the formation of the thermal boundary layer and its contribution to jet formation poses some interesting questions. The nature of the jet structure has implications for other fields, such as rocket aerodynamics, in which the jet exhaust into space takes the shape of a free jet plume.[43] In chemical studies of jet sampling by the conventional method, the experimentalist is hindered by a lack of available data on the structure of the jet. Although there is a huge volume of engineering literature on free jet parameters (for example, x_B, jet height) for cases in which there is finite pressure on the downstream side of the orifice, there is a lack of corresponding data for cases in which the free jet expands into a vacuum. Such is the case for any experiment involving mass-spectrometric analysis of shock tube flows. At best, there exists information on centerline properties (for example, ρ centerline, Mach#) for the free jet

expansion into a vacuum. However, experimental data on free jet properties at off-centerline positions is virtually non-existent.

The lack of what seems to be very basic data on free jet expansions points the way to future experiments in the field. One useful jet parameter that could be obtained experimentally would be that of jet height. Optical reflection[43] has been used to study density differences in gas thermal boundary layers; in addition, electron beam fluorescence [38] has been used to obtain measurements of density in rarefied gas flow. It would be interesting to explore if either technique, by pinpointing density differences between background gas and jet gas, could be utilized to get jet height values for the pressure ratios, temperature ranges and orifice sizes used in shock tube-mass spectrometer work.

It would be interesting to study the effect of the thermal boundary layer upon jet structure by a method in which the difficulties of scanning specific portions of the jet would be avoided. A non-conducting shock tube endwall could be used in a series of experiments similar to Gutman's[15]. Any differences in rate constants and activation energies from performing a duplicate set of experiments with a non-conducting and a metal endwall would be explored. In such a way, the limitations of the conventional shock tube/mass spectrometer experiment could be further defined.

VI. APPENDIX

APPENDIX A

BOUSSINESQ'S EQUATION

The use of Boussinesq's equation as reported by Shames[45], enables one to predict the occurrence of fully developed laminar flow through a pipe. In fully developed flow, the velocity boundary layer thickens to such a degree that the mainstream flow is pinched off and boundary layer fills the entire tube diameter. Consequently, with fully developed flow, the core fluid vanishes at the transition point Z_T.

For any experiments involving the expansion of shock-treated gases through an orifice, it is important to know that the core gas can be sampled. Therefore, the transition point must not occur within the orifice channel (See Figure 8); otherwise, solely boundary layer would be sampled. This conclusion is valid for our present experimental set-up.

$z_T = 0.03 \text{ Rey } D$

$z_T = 0.03 \frac{\rho V D^2}{u}$

Rey= Reynold's number

ρ = gas density (g/cm^3)

V = gas velocity (cm/sec)

D = orifice diameter (cm) = 5.08×10^{-3} cm

μ = viscosity coefficient (poise = g/cm sec)

z_T = transition length for fully developed laminar flow to occur (cm) choosing a typical set of reflected shock conditions - subscripted by the number 5 - for argon:

$T_5 = 3000°K$

$\rho_5 = 160 \times 10^{-6}$ g/cm^3

V_5 = through orifice $\left(\frac{\gamma RT_5}{MW}\right)^{1/2} = \left[\frac{1.67 \times \frac{2 \text{ cal}}{°\text{Kmole}} \times 3000°\text{K} \times 4.184 \times 10^7 \frac{\text{gcm}^2}{\text{sec}^2\text{cal}}}{40\text{g/mole}}\right]^{1/2}$

$= 10.24 \times 10^4$ cm/sec

μ at 1100°K for argon = 5.63×10^{-6} poise

μ at 3000°K makes use of Sutherland's equation[47];

$$\mu_{new} = \mu_{old} \left(\frac{T_{old} + \text{constant}}{T_{new} + \text{constant}}\right) \left(\frac{T_{new}}{T_{old}}\right)^{3/2}$$

constant = 142 for argon

$$\therefore \quad \mu_{new} = 563 \times 10^{-6} \text{ poise} \left(\frac{1100 + 142}{3000 + 142}\right) \left(\frac{3000}{1100}\right)^{3/2}$$

$$\mu_{new} = 1001.5 \times 10^{-6} \text{ poise}$$

$$z_T = 0.03 \frac{\left(160 \times 10^{-6} \frac{g}{cm^3}\right)(10.24 \times 10^4 \text{ cm/sec})(5.08 \times 10^{-3})^2 cm^2}{1001.5 \times 10^{-6} \text{ g/cm sec}}$$

$$= 1.37 \times \frac{10^{-6}\ 10^4\ 10^{-6}}{10^{-6}} \text{ cm cm} = 1.27 \times 10^{-2} \text{ cm} = 0.013 \text{ cm.}$$

This result indicates that since the pipeline in our orifice is 0.025 mm, no boundary layer closure occurs within the orifice, (See Figure 8).

APPENDIX B

ELECTRON GUN FOCUSING

In order to focus the electron beam (at a given electron energy) to get a collimated stream of electrons, it is necessary to find the unique values of the vertical and horizontal deflection voltages (ϕ_{IR} and ϕ_{IC}) which yield a maximum trap current while the electron repeller and electron lens voltages (ϕ_{ER} and ϕ_{EL}) are simultaneously optimized. At the focus condition, small variations in the deflection voltage controls (ϕ_{IR}, ϕ_{IC}) or beam divergence controls (ϕ_{ER}, ϕ_{EL}) cause a large decrease in trap current to occur. The beam is deflected off the electron trap or becomes thickened to such an extent that a large fraction of particles miss the trap target after they exit the ionization chamber.

A sample electron gun map (October 23, 1975) is given below. The recorded numbers are microamps of trap current. The focus condition is ϕ_{ER} = 408 v., ϕ_{EL} = 228 v., ϕ_{IC} = 8 v., ϕ_{IR} = -37.5 v., ϕ_{EL} = 75 v.

Table 13. Electron Gun Map

ϕ_{IR} (volts)	-10	-5	0	+5	+10	+10 v.	ϕ_{IC} (volts)
-150 v.	1.0	0.9	1.0	1.0	1.0	1.0	
-125	1.0	0.9	0.9	1.0	1.0	1.0	
-100	1.0	0.9	0.9	1.0	1.0	1.0	
-75	1.0	0.9	1.3	1.0	1.0	1.0	
-50	1.0	0.9	2.6	1.0	2.0	1.0	
-37.5	1.0	1.5		16.0	15.5	1.0	
-25	1.0	6.0	1.0	8.5	5.5	1.0	
0	1.0	1.0	1.0	1.0	1.0	1.0	
+25	1.0	1.0	0.9	1.0	1.0	1.0	
+50	1.0	1.0	0.9	1.0	1.0	1.0	
+75	1.0	1.0	0.9	1.0	1.0	1.0	
+100	1.0	1.0	0.9	1.0	1.0	1.0	
+125	1.0	1.0	0.9	1.0	1.0	1.0	

The procedure to focus the beam is an iterative method which eventually converges the beam and yields a sharp maximum in trap current.

1. Choose a value of ϕ_{EE} (keeping it fixed), and choose a value of ϕ_{ER} and ϕ_{EL}. Make a plot of I_{Trap} by varying ϕ_{IR} and ϕ_{IC} in, for example 25 volts steps so that an I_{Trap}, maximum is found. Hold ϕ_{IR}, ϕ_{IC}, fixed at the values set to give I_{Trap}, maximum.
2. Vary ϕ_{ER} locally until an even higher I_{Trap} is found. Hold ϕ_{ER} fixed.
3. Vary ϕ_{EL} locally until a new, higher I_{Trap} is found. Hold ϕ_{EL} fixed.
4. Vary ϕ_{IR}, ϕ_{IC} locally to further maximize I_{Trap}. The values of ϕ_{ER}, ϕ_{EL}, ϕ_{IC}, ϕ_{IR} from steps 2-4 become the conditions for a focus. ϕ_{EE} has been fixed throughout.
5. To get a finer focus, another I_{Trap} plot made with the $\phi_{ER,EL}$ values obtained in steps 2-3 and more finely resolved values of $\phi_{IR,IC}$ (say, in 5 volt steps about the values obtained in step 4) can be done. The whole procedure can be repeated as many times as is needed to get a reasonably sensitive focus condition.

APPENDIX C

A. Operation of the Quadrupole Mass Filter

The theory and design of the quadrupole mass-spectrometer has been thoroughly discussed in many standard references on mass-spectrometry. The quadrupole has opposite poles connected as pairs which receive R.F. signals of the same magnitude but of opposite polarity. Similarly, one set of poles receives a positive D.C. voltage at the same time that the other set of poles obtains a D.C. voltage of the same magnitude but of negative sign.

The resolution of the instrument is controlled by varying the (D.C./ $A.C._{(peak)}$) ratio. Maximum resolution is theoretically obtained when this ratio equals 0.168. During operation of the quadrupole, the resolution ratio is kept constant. It is set by the "coarse" potentiometer shown in Figure 15b. The mass which is allowed to pass through the pole structure at maximum resolution is dictated by the following equation:

$$(M/q)_{max} = 4\phi AC_{(peak)}/r_o^2\omega^2 = 8\phi_{DC}/r_o^2\omega^2$$

where $\omega = 2\pi\nu$ = the angular frequency of the oscillator crystal, r_o = 1/2 (distance between opposite poles), and ϕ_{AC}, ϕ_{DC} are the values of those voltages at the apex of the Paul Stability Diagram.

If less than apex resolution is used, the following equation is

used to find the new values (subscripted 2) of $\phi_{A.C.}$ and $\phi_{D.C.}$ for scanning the mass peak at the new resolution ratio, $\frac{A_2}{Q_2} = R_2$.

$$\frac{M_1}{M_2} = \frac{\phi_{DC_1} A_2}{\phi_{DC_2} A_1} = \frac{\phi_{AC_1} Q_2}{\phi_{AC_2} Q_1} . \quad (\phi_{AC_{1,2}} \text{ are peak values})$$

Let A_1, Q_1 be the apex values from the Paul Stability Diagram[37], $A_1 = .237$ $Q_1 = .706$.

Let ϕ_{AC_1}, ϕ_{DC_1} be those values of voltages needed to locate the mass peak M_1 at apex conditions where $R_1 = \frac{2\phi_{DC_1}}{\phi AC_1} = \frac{A_1}{Q_1}$. Then Mass $M_2 = M_1$ is found at the new ratio setting R_2 and ϕ_{DC_2} ϕ_{AC_2} are found by:

$$\phi_{DC_2} = \phi_{DC_1} \frac{R_2}{R_1}.$$

Note that $\phi_{AC_2} = \phi_{AC_1}$; the setting of a new ratio only changes ϕ_{DC}; therefore at a new setting ϕ_{AC} is unchanged.

During the firing of shots, the protected (quadrupole and electron gun) electronics are turned on and about 5 torr of the gas under study is admitted to the test section of the shock tube. The amplitude of the R.F. voltage is set by adjusting the voltage output of the John Fluke supply and the resolution control is varied until maximum resolution is found. As the resolution increases, the ion current monitored on the Keithley electrometer decreases. One can verify that a mass peak has been located by recording it on a strip chart recorder. If the ion current is still variable by slightly changing

ϕ_{IR}, ϕ_{IC}, ϕ_{DP1}, ϕ_{DP2}, ϕ_{Fluke}, then the D.C. and R.F. signals have not drifted above their apex values. In practice, the resolution ratio is set slightly below the apex ratio of 0.168.

After a shot, the oscillator is checked to see if retuning of the tank circuit or rebalancing of the R.F. or D.C. voltages is needed. Tuning to resonance is done by obtaining minimum plate current on the 100 ma. meter through adjusting the trimmer control. The R.F. amplitudes on both sets of poles are adjusted by the balance pot; a similar control matches the amplitudes of the D.C. signal applied to each set of poles. In practice, retuning and rebalancing is seldom needed during a day's work. It is more common to drift off the maximum height of a mass peak, and adjustment of ϕ_{IR}, ϕ_{IC}, ϕ_{DP1}, ϕ_{DP2}, ϕ_{Fluke} is usually needed before every shot.

APPENDIX D

SUMMARY OF QUADRUPOLE OSCILLATOR OPERATION

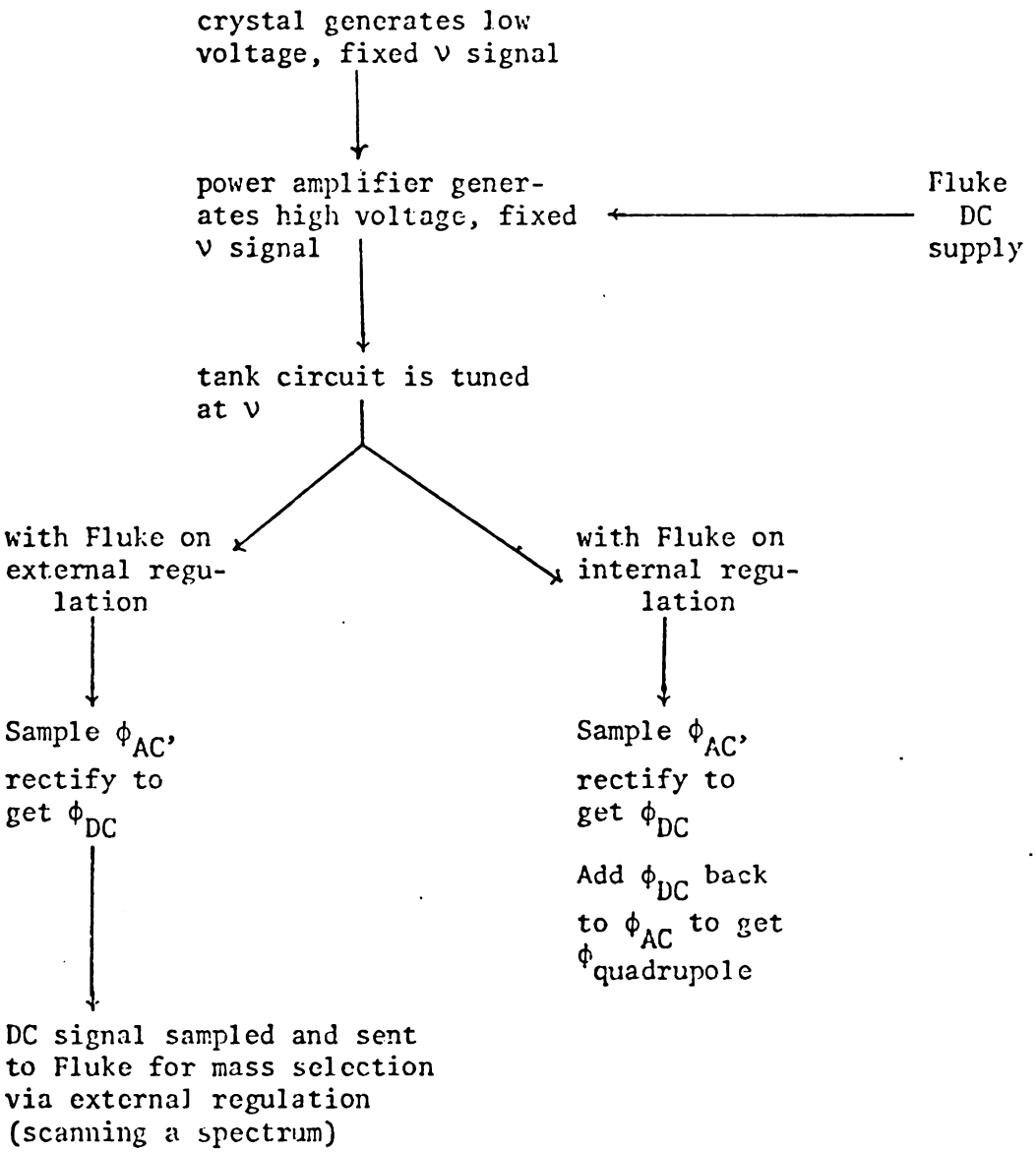

APPENDIX E

TURN-OFF PROCEDURE FOR THE ELECTRON GUN AND QUADRUPOLE ELECTRONICS

1. Shunt Weston-622 microammeter.
2. Turn ϕ_{FIL} to zero by dialing down voltage control.
3. Turn off protected and unprotected electronics switch.
4. Switch system to vacuum over-ride.[a]
5. Turn off ionization gauge; switch gauge controller[b] to warm-up.
6. Close gate valve of diffusion pump.
7. Switch gauge controller off.

[a] If there is a vacuum failure of sufficient magnitude to turn off the ion gauge, the activated vacuum switch will automatically turn off the diffusion pump, and protected (electron gun and quadrupole) electronics. This is useful when an experiment is in progress. During turn-off, the vacuum switch is put on "over-ride"; this allows the diffusion pump to stay hot for the next day's work.

[b] The ion gauge automatically turns off if a vacuum failure causes the pressure to increase 1.5 × full-scale deflection or more.

APPENDIX F

VACUUM SYSTEM TURN-ON

The conditions which must be met for turn-on of the vacuum system are summarized here. They are shown in the following illustration.

Unprotected electronics on:

1. circuit breaker is on
2. fuse is good
3. unprotected system is plugged in

Protected electronics on:

1. circuit breaker is on
2. 15 amp fuse is good
3. K_1 relay to Cooke controller is plugged in (brown plug)
4. ion gauge filament is on
5. protected system is plugged in

Diffusion pump is on:

1. circuit breaker is on
2. 15 amp fuse is good
3. rough pump switch is "on" or "over-ride"; if "on" -- "on" light will be lit; if "over-ride" -- "over-ride" light will be lit
4. cooling water switch is "on" (and make sure water is running)
5. $N_2(\ell)$ switch is "over-ride"

6. $N_2(\ell)$ trap-filler switch is "on" or "off"
7. vacuum switch is "on" or "over-ride"
8. diffusion pump overtemperature control is plugged in and the pump temperature is okay
9. diffusion pump heater is plugged in

Roughing pump is on:

1. circuit breaker is on
2. 15 amp slow blow fuse is good
3. roughing pump is plugged in

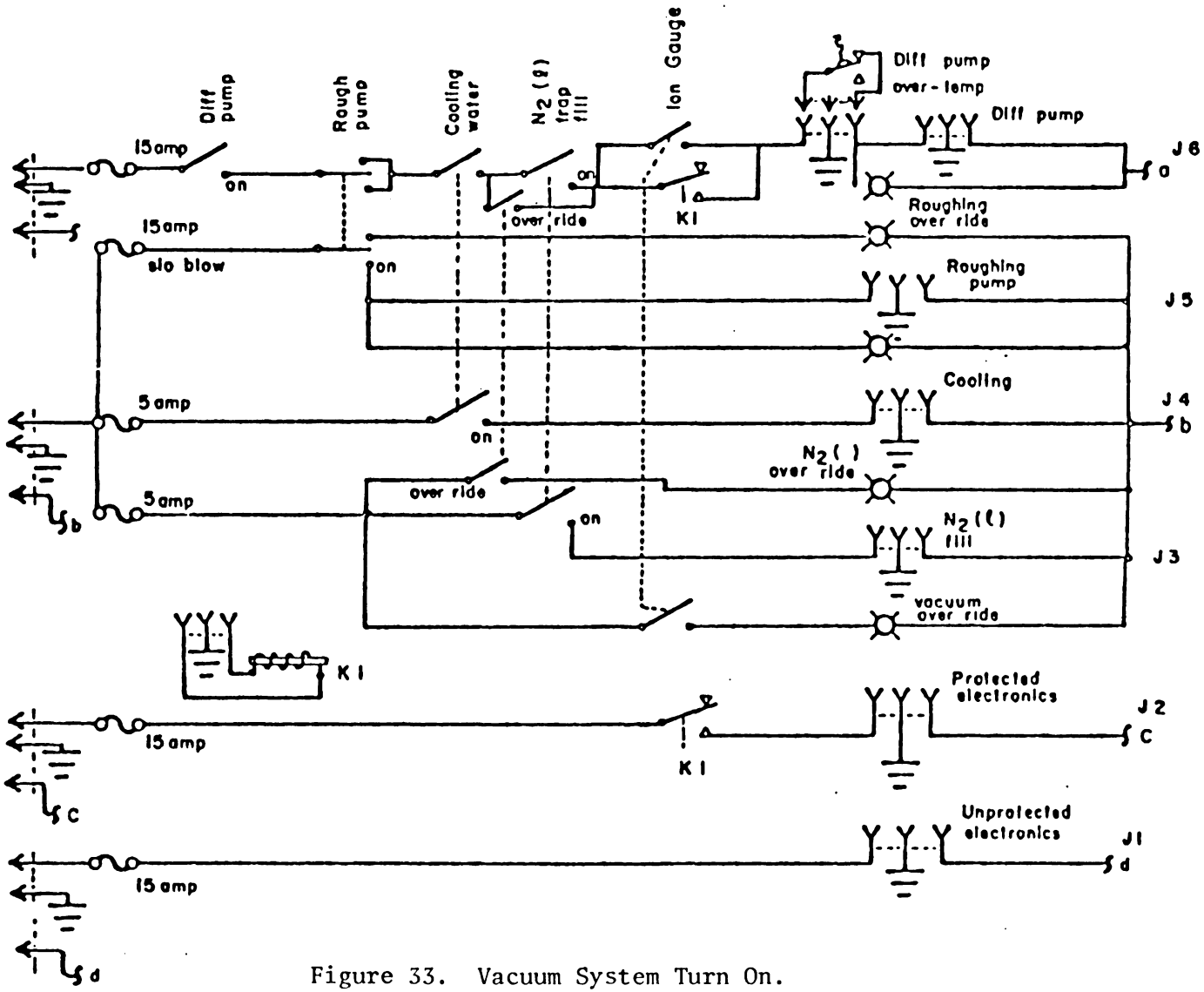

Figure 33. Vacuum System Turn On.

APPENDIX G

EFFECT OF $P_{M.S.}$ ON SPECTRA RECORDED UNDER STATIC CONDITIONS

The following spectral peaks (N_2+) shown in Figure 34, were monitored at $P_{M.S.} = 4.3 \times 10^{-5}$ torr, 6×10^{-5} torr and 7×10^{-5} torr respectively. The electron multiplier voltage was 2000 volts in each case.

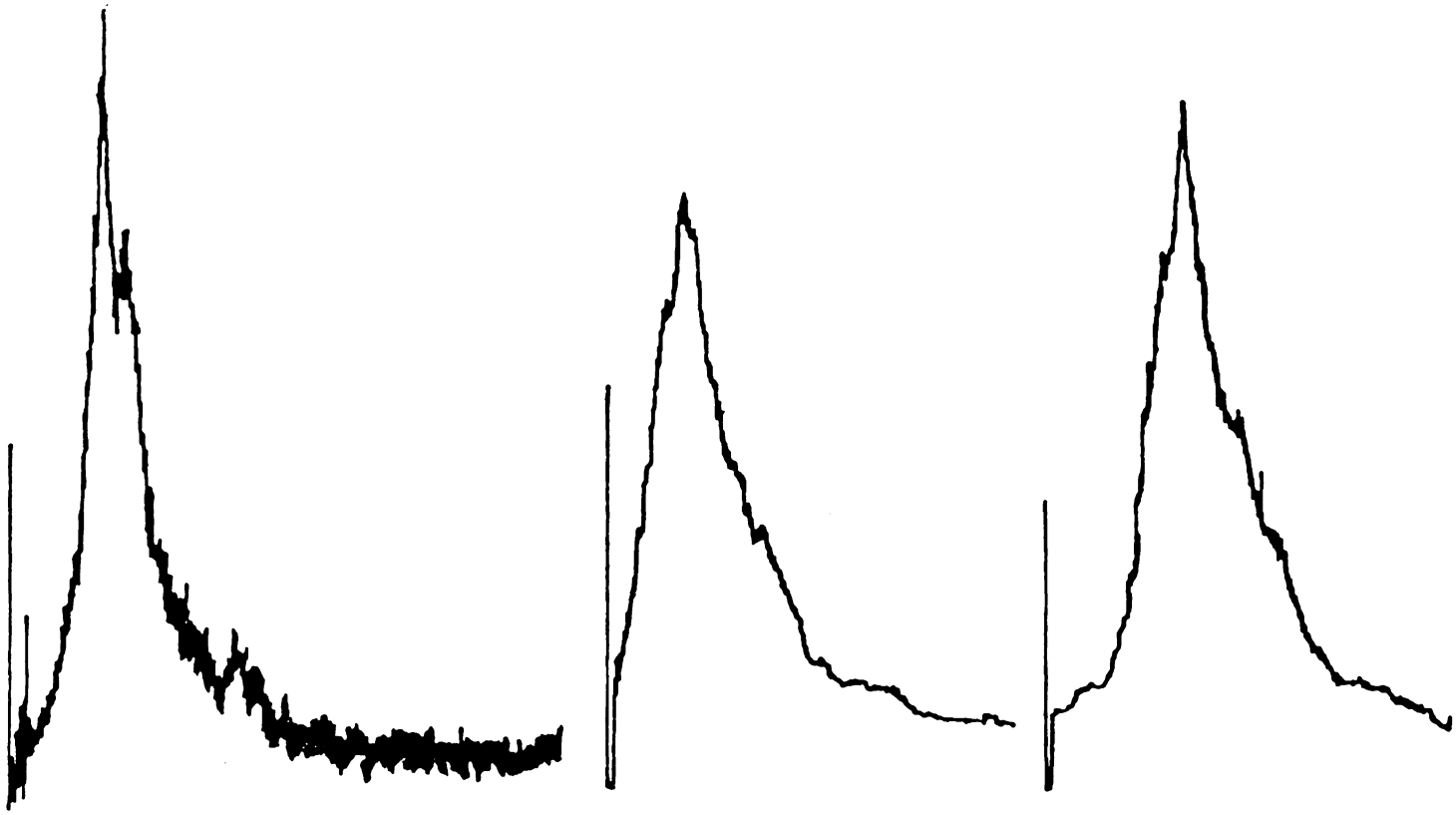

$P_{M.S.}$ = 4.3×10^{-5} torr	6×10^{-5} torr	7×10^{-5} torr
amps full scale = 3×10^{-8} amps	1×10^{-6} amps	1×10^{-6} amps

Figure 34. Effect of $P_{M.S.}$ on Spectra Recorded under Static Conditions.

APPENDIX H

SOME DESIGN REQUIREMENTS FOR NARROWING ELECTRON BEAM WIDTHS

In the absence of focusing, one force that can cause a gradual increase in the diameter of an electron beam is that of space-charge. The effect is most pronounced in high density beams.

In order to consider space-charge spreading in electron beams, the usual (ideal) model is that of an unconfined beam drifting between two plates forming a uniform electric field. Our present beam is not passing through an ideal drift chamber. The top surface of the ionization chamber, formed by a plate at the housing potential, perturbs the field created by the entrance and exit aperture plates to the ionization chamber. Nevertheless, the drift model provides figures of merit for estimating the effects which widen electron gun beams.

The spread of a round beam in a drift region is evaluated by solving the paraxial equation[47]

$$K_1 \frac{2}{r_o} = \int_0^R \exp u^2 \, du$$

$$\exp u^2 = r/r_o$$

$$K_1 \text{ (dimensionless)} = \left| \frac{p}{8\pi\epsilon_0 (2\eta)^{1/2}} \right|^{1/2} = (7.6 \times 10^{-3})^{1/2} \, p^{1/2}$$

where P = perveance = $(I/V^{3/2})$ $\left(\frac{\text{uamps}}{\text{volts}^{3/2}}\right)$

e_0 = permittivity constant (farad/meter)

n = q/m (coul/kg)

r_o = initial beam radius (m)

z = axial distance (m)

The universal beam spread curve is given by a plot of r/r_o vs. $\frac{K_1 z}{r_o}$ and is plotted in reference 47. In particular, the graph shows that a doubling of beam diameter occurs at a $z = \frac{1.1 r_o}{K_1}$. To get an estimate of the severity of space-charge effects for our present gun

$$z = \frac{1.1(0.03")}{(7.6\text{x}10^{-3})^{1/2}\frac{(100)^{1/2}}{(160)^{3/4}}} = 1.8".$$

Therefore, if we consider the present electron gun in terms of the ideal model, the beam would have to travel an additional 1.8" for the beam width to double. This distance is greater than the width of the present ionization chamber, and the result seems to show that in terms of the drift model, that space-charge effects are not very important in diverging the width of the present beam.

The other major contribution to beam spreading comes from the fact that electrons have a velocity distribution. The size of our present beam is probably dictated by thermal effects where $_0$, the image density = $\rho_{cathode} \left(\frac{eV}{kT} + 1\right) \sin^2\theta$, θ = half angle of arrival of electrons at the image. In order to increase the density ρ_0 of the beam, and thereby reduce the velocity spread, it would be necessary to increase V, increase the cathode emission density ρ_C by using a different emitter, or operate the cathode at a higher temperature T to increase ρ_C. (The problems with changing θ are discussed in reference 47 for real systems which are not aberration free).

The problem is increasing ρ_0 by any of these methods is simply that in increasing ρ_0, space-charge effects can again come into play. It is for this reason that magnetic collimation has been a practical method of confining divergent beams. In particular, the current obtained in a beam system focused by a series of magnets separated a distance L apart is:[48] $I = 1.451 \times 10^6 V^{1/2} r_o^2 \left(\frac{1}{L} \int_{z_1}^{z_2} B^2 dZ\right)$ where B is the average magnetic field strength on the axis. As an example, the design of a new gun which would differ from our present gun by simply applying a magnetic field for focusing could be evaluated. For some typical gun parameters, solving the above equation for ro,

$$r_o^2 = \frac{I}{1.451 \times 10^6 V^{1/2} \left(\frac{B^2}{L} (Z_2 - Z_1)\right)} \left[1.451 \times 10^6 = \varepsilon_0 \eta^{3/2}, \left(\frac{sec^2 coul^{3.5}}{Kg^{2.5} m^2}\right)\right]$$

$I = 2 \times 10^{-3}$ amps $\qquad$ V = 160 volts

L = 1/2" (the ionization chamber is about 1.2)

B = 200 gauss (typical magnetic field used in focusing T.O.F. beams)

$= 2 \times 10^{-2}$ Weber/m^2

Z_2-Z_1 = distance over which the focusing field extends = 1/2"

This gives an $r_o = 0.5 \times 10^{-3}$ meters = 0.5 mm or d = 1mm. The size of 1 mm. can be either a minimum spot size or maximum depending on whether the beam was magnetically expanded or compressed as it entered the magnetic field. The latter is dependent on the cathode flux density.

The value of r_o is proportional to $\frac{1}{V^{1/4}B}$. Therefore, it is the magnetic field strength which most strongly affects the beam width. The beam voltage would have to increase 16-fold to produce the same decrease in beam radius as caused by doubling the axial field strength B. In any event, the above result suggests that a marked improvement in beam width could be made by magnetic collimation.

2. THE PYROLYSIS OF NEOPENTANE BY ATOMIC RESONANCE ABSORPTION SPECTROPHOTOMETRY

I. INTRODUCTION

A. The Technique of Atomic Resonance Absorption Spectrophotometry (ARAS) and Its Application to Shock Tube Experiments

In shock tube experiments utilizing the technique of atomic resonance absorption spectrophotometry (ARAS), a light source produces the appropriate atomic resonance radiation. Light sent through the shock tube is partly absorbed by the atoms in the shock-heated test gas. The attenuated radiation leaving the shock tube is then passed by a monochromator or filter arrangement to a photomultiplier for detection. The ARAS technique relies on the principle that the concentration of atoms produced in the heated test gas is releated to the fractional absorption of the emitted light from the source. The intensity of resonance radiation emitted by the atoms in the shock tube is assumed negligible with respect to the transmitted lamp radiation.

In particular, the experiments presented in this work make use of the ARAS technique for the measurement of H atom concentrations. The atomic resonance radiation for H atom, termed Lyman-α, is measured at approximately 1215 Å and involves quantum transitions between the n=2 and n=1 levels of the hydrogen atom. The Lyman-α line, along with other selected hydrogen lines, is shown in Table 14.

The ARAS experiments in this work study the decomposition of neopentane to obtain the rate constant k_1 for the initiation step, $C_5H_{12} \xrightarrow{k_1} C_4H_9+CH_3$. The C_4H_9 radical is highly unstable and produces H atom by the reaction of $C_4H_9 \rightarrow i\text{-}C_4H_8+H$. Consequently, the

progress of reaction can be monitored by the appearance of H atoms, and the ARAS technique can be utilized. As such, the study in this work is the first shock tube investigation of the pyrolysis of neopentane using a spectroscopic technique, in which H atom is the reaction species of interest. Earlier single pulse studies[82,84], to be discussed in Section C, monitored the decomposition of neopentane via analysis of other reaction products, chiefly i-C_4H_8.

The ARAS technique has the advantage that low (ppm) amounts of reactant can be used in the test gas mixtures. This simplifies the reaction mechanism. Many side reactions (most of them being bimolecular) occur to a negligible extent when ppm concentrations of reactant are used, and can be eliminated from the reaction scheme. The analysis of the kinetics of neopentane, to be described in Section III, is simplified in this manner.

Some basic concepts involved in absorption experiments can now be introduced. In absorption experiments, the Beer's Law expression:

$$\ln(I_0/I) = \epsilon bc, \text{ where}$$

I_0 = initial intensity of light at time = 0 (measured)

I = intensity of transmitted light after absorption by atoms generated in the shock tube at times t > 0 (measured)

ϵ = absorption coefficient ($mole^{-1}cm^2$) (calculated)

b = optical path length in the shock tube (cm) (measured)

c = concentration of atomic species being monitored ($mole/cm^3$)

Table 14. The Hydrogen Spectrum[59]

Series	Quantum Number		Wavelength, Å
	j (lower state)	k (upper state)	
Lyman	1	2	1215
	1	3	1026
	1	4	970
	1	5	949
	1	6	940
	1	∞	912
Balmer	2	3	6563
	2	4	4861
	2	5	4341
	2	6	4102
	2	7	3970
	2	∞	3650
Paschen	3	4	18751
	3	5	12818
	3	6	10938
	3	7	10050
	3	8	9546
	3	∞	8220

applies if the emission line width from the light source is very small compared to the absorption line wideth of the atoms produced in the shock tube. Consequently, a plot of $\ln(I_0/I)$ versus c would yield a straight line. However, complications present in absorption work using the ARAS technique do not allow a direct, simple application of Beer's Law to relate measured values of $\ln(I_0/I)$ to atom concentrations c produced in the shock tube. In ARAS experiments, self-absorption is present to the extent that the lamp emission line width is no longer very small compared to the absorption line width. ϵ becomes a function of atom concentration, as well as temperature.

Self absorption[60] occurs when atoms in the lower state of a transition absorb the radiation emitted by other atoms of the same species. Since absorbance = $\ln(I_0/I)$, re-absorption occurs to a greater extent in those regions of the profile showing the greatest intensity. For example, if the original line profile is Gaussian, self-absorption causes the top of the profile, where I_0 is at a maximum, to flatten out. In fact, the line profile may broaden to such a degree that a minimum occurs and the resultant profile appears to have two humps.* Figure 35 taken from reference 66, shows such a profile in the descriptive manner. The large dip in the (calculated) self-absorbed profile lies in the range of greatest intensity of the original Gaussian profile.

In ARAS experiments, the presence of self absorption <u>in the lamp</u>

---

*such extreme self-absorption is also termed "self-reversal."

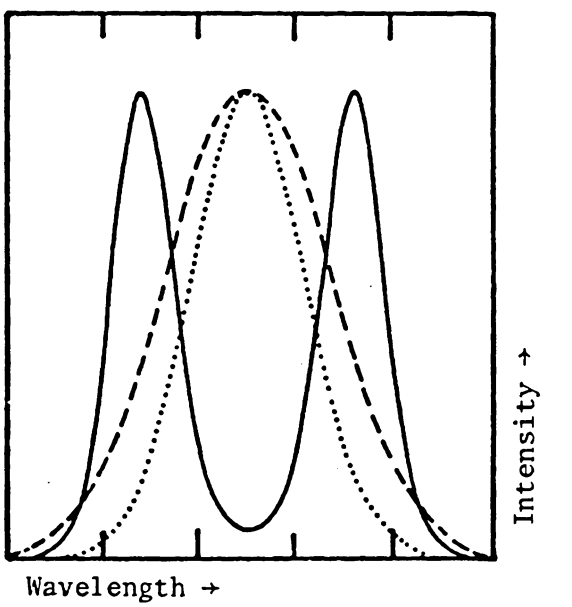

Figure 35. Extreme Self-absorption in a Gaussian Line.

modifies the shape of the lamp profile. As the emitted lamp radiation passes through the shock tube and is absorbed, further broadening occurs. Several workers in the field have attempted to formulate these multiple sources of broadening which occur in shock tube experiments.

Braun, et al.[61] employed a two-layer model for characterizing the emission lines generated by a Lyman-α lamp. The experimental source was a microwave discharge lamp; the source gas was a flowing mixture of D_2 in helium.* In their model, the source consists of two regions. Zone I contains emitting and absorbing atoms that are uniformly dispersed in the plasma. Zone II, in front of Zone I, is assumed to contain only absorbing atoms. In such a way, the two layer model attempts to simulate the actual experimental discharge lamp, which consists of a mixture of emitting and absorbing atoms at the plasma kinetic temperature. The concentration of emitters and absorbers in the real gas mixture, which are distributed in a non-uniform manner in the plasma due to temperature gradients between the center and edges of the lamp[62] cannot be determined experimentally. Figure 36, taken from reference 63, shows the two-layer lamp model, along with the additional absorbing layer due to shock tube atoms.

---

*Typically, discharge lamps used in ARAS measurements make use of flowing gas mixtures. The flow system helps to minimize the growth of impurities within the lamp so that the emission spectrum is less contaminated by the presence of extraneous lines. Impurity reactions are suppressed, and the emitted line intensity from the atomic species under study is higher.

The line profile of the light emitted from the first layer of the lamp shows self-absorption but not self-reversal. Passage of the light through the absorbing layer of the lamp leads to some self-reversal, which is increased after passing through the shock tube. The total intensity decreases from left to right in the figure.

Braun, et al.[61] obtained experimental measurements of the Lyman source emission line shape at high resolution to test their lamp model. Their model is a function of the optical depths (OD)* of Zones I and II, radiation frequencies, and Doppler width (same in Zones I and II). The length of Zones I and II was the only adjustable parameter.

Lifshitz, et al.[65] measured Lyman-α line profiles for H and D emitted from $H_2(D_2)$ - He lamp mixtures. These profiles were then matched by calculations patterned after the two-layer lamp model discussed above. Two absorption parameters, to take into account absorbance in the plasma (ABP) and absorbance in the second zone between the plasma and lamp window (ABO), were used to modify the line shapes for the effects of self-absorption. In these cases, a pure Doppler profile was assumed initially.

The modeling procedure developed above was further utilized by

---

*OD = $\sigma_0 n \ell$; σ_0 is the absorption cross section, n = number of density of absorbing atoms, ℓ = length of zone (I and II). The number of absorbers was calculated by assuming complete dissociation of the D_2 in the lamp mixture at a lamp pressure of .8 torr.

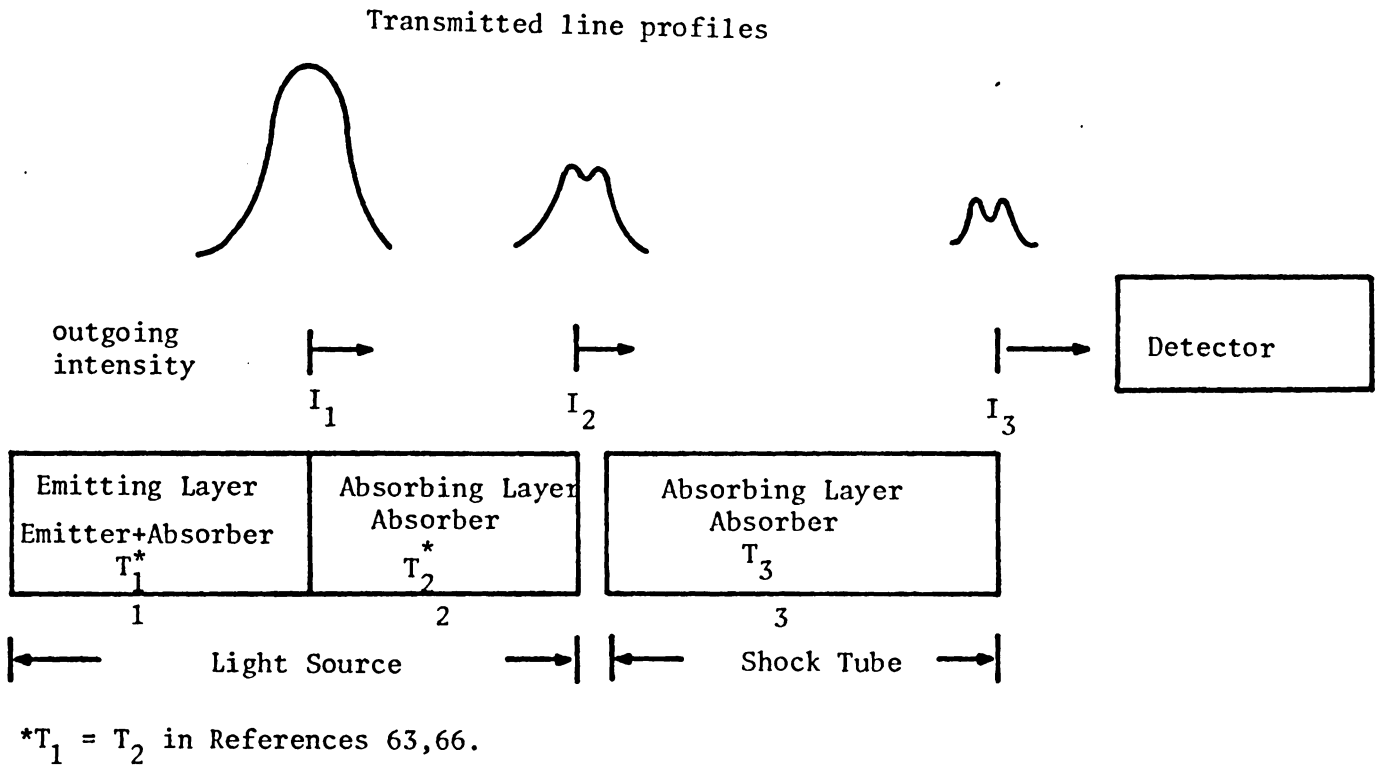

*T_1 = T_2 in References 63,66.

Figure 36. Model for Light Source and Absorbing Species in Shock Tube.

Chiang, et al.[66] when shock tube experiments on H and D atom were carried out. The line shape emitted by the discharge lamp (at a plasma temperature of 700°K) is assumed to be pure Doppler and is modified for the effects of self absorption by parameters ABP and ABO, the absorbances within the plasma and between the plasma and the shock tube window, respectively. The H (D) atom absorbers presented in the heated shocked gas at T_5 and P_5 are assumed to have a Gaussian (Doppler) profile. The resultant line shape which enters the detector, after having passed through the shock tube, is then calculated from known values of I_0/I obtained from absorption experiments. The values of ABP and ABO which bring the ratio $\frac{\epsilon \text{ (experimental)}}{\epsilon \text{ (calculated)}}$ to a value of one are chosen as the best values. One set of absorption parameters (ABP, ABO) is therefore used to fit absorption data over a wide range of atom concentrations produced in the shock tube, for example, 0 - 20 x 10^{-12} $\frac{\text{mol}}{\text{cc}}$ for D atom.

The relationship between emitter and absorber line widths, in a self reversed H Lyman-α line, as calculated by Chiang, et al.[66] is shown in Figure 37. Two Gaussian profiles, at shocked gas temperatures of 1000° and 2000°K, represent the absorber line shape. They are displayed against the lamp emission line profile. The emission line shape is wider than the Gaussian profile at 1000°K, and about the same width as the Gaussian profile at 2000°K. ϵ, under these circumstances, is no longer a simple function and, atom concentrations in the shock tube cannot be reliably found from Beer's Law, where $c = \frac{\ln I_0/I}{\epsilon \; b}$. The calibration techniques used in shock tube

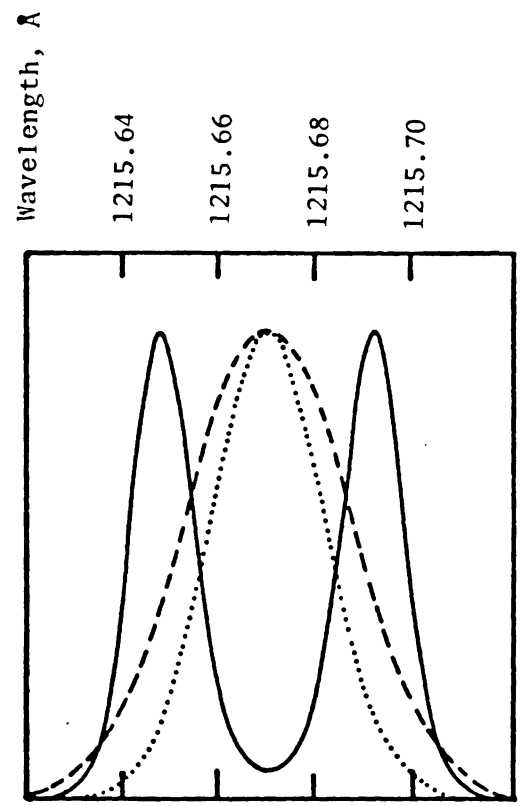

Figure 37. Emitter and Absorber Line Profiles.

experiments to relate the measured values of $\ln(I_0/I)$ with the corresponding atom concentrations produced at T_5 are discussed in the next section.

B. The Use of Atomic Resonance Absorption Spectrophotometry to Monitor H, D and D Atom Concentrations

Atomic resonance absorption spectroscopy has been applied to the measurement of H and D atoms and, most recently, to reaction systems which involve the production or depletion of O atoms. The recent literature (since 1968) which surveys the use of this technique will be presented here.

Myerson and Watt[67] measured the rate of the reaction $H_2 + Ar \rightarrow 2H + Ar$ by atomic resonance absorption spectrophotmetry at the Lyman-α line. First, they developed procedures to correlate the attenuation of the Lyman-α source radiation with known atomic concentrations produced during shock heating of gas mixture.

Two different techniques were utilized. First, a calibration procedure was developed in which deuterium was used as the emitting species in the source and the test gas mixture. The lamp mixture was 10% D_2 in He; the calibration test gas was a dilute (few ppm) mixture of D_2 in Ar. In order to obtain complete dissociation of the D_2, the test gas had to be shocked at about 4000°K. The use of deuterium for the calibration runs eliminated the problem of having hydrogen-containing impurities contributing to the attenuation of the source radiation during calibration experiments. For the actual experimental

runs, measurements on the H_2 + Ar reaction were carried out using a 10% H_2 in He gas mixture in the light source. Both H atoms and D atoms emit (absorb) at the Lyman-α line. The wave length for H Lyman-α is 1215.67Å, and for D Lyman-α is 1215.34 Å. H atoms in the shock tube will not absorb D radiation appreciably, or vice versa, unless the discharge lamp is operated under conditions that produce a very much broadened line. (An example of this is given later). By substituting hydrogen atoms for deuterium in the source, the Doppler linewidth for the H atom source is increased by a factor of $\sqrt{2}$. However, self-absorption effects in the source are less for H atoms; H atoms absorb H atom resonance radiation less strongly than D atoms absorb D atom resonance radiation, assuming that equal concentrations of H atom or D atom are present. Thus, self-broadening is reduced in the hydrogen source. Taking Doppler and self-broadening effects into account, Myerson and Watt found that the hydrogen source linewidth was essentially the same as the deuterium source linewidth at the assumed source temperature (600°K). The linewidth of the absorbing species produced in the shock tube is then determined by the shocked gas temperature and pressure. The use of the hydrogen light source permitted in the detection of small amounts of dissociation for the test gas, since the atomic absorption coefficient for hydrogen is relatively large. In this way, the rate constant for mixtures of .01%, .1% and 1% H_2 in Ar could be obtained, and was found to be $2.23 \times 10^{12} T^{1/2} \exp(-92600 \text{ cal./mole/RT}) \text{ cm}^3/\text{mol sec}$ for the temperature range 2290-3700°K.

In a second set of experiments, both the calibration experiments and experimental rate measurements were performed using deuterium as the emitting species in the source, and hydrogen atom formed by reaction of the test gas in the shock tube as the species which absorbed the source radiation. This approach could be called near-resonance absorption, since the central frequencies of the lamp and absorber are different, although close. Profiles of the emitted radiation and the absorber overlap only slightly, so the sensitivity is much lower than for ARAS.* First, calibration experiments were performed using the reaction $H_2 + Ar \rightarrow 2H + Ar$ (1% H_2 in Ar); equilibrium concentrations of H atoms could be produced by this reaction at 3000-4000°K. The deuterium source radiation could then be calibrated for these known quantities of H atoms produced in the shock tube. Experimental rate measurements were then carried out on the dissociation of H_2 in Ar (now 10% H_2 in Ar) using the same deuterium source.

The rate constants using this higher percentage of H_2 in the test gas were about 40% higher than in the more dilute mixtures. This difference was accounted for by allowing for the additional effectiveness of H_2-H_2 collisions (compared to that of H_2-Ar collisions) and the rate data were fitted by a rate constant which was a combination of the H_2-Ar rate constant and the rate constant for dissociation of H_2 with H_2 as the collision partner.

---

*An H atom line profile (reference 65) from ARAS experiments which shows self-absorption is presented in Figure 38. The broadened profile is 0.1 Å wide. In this example, the source gas mixture is 0.1% H_2 in He.

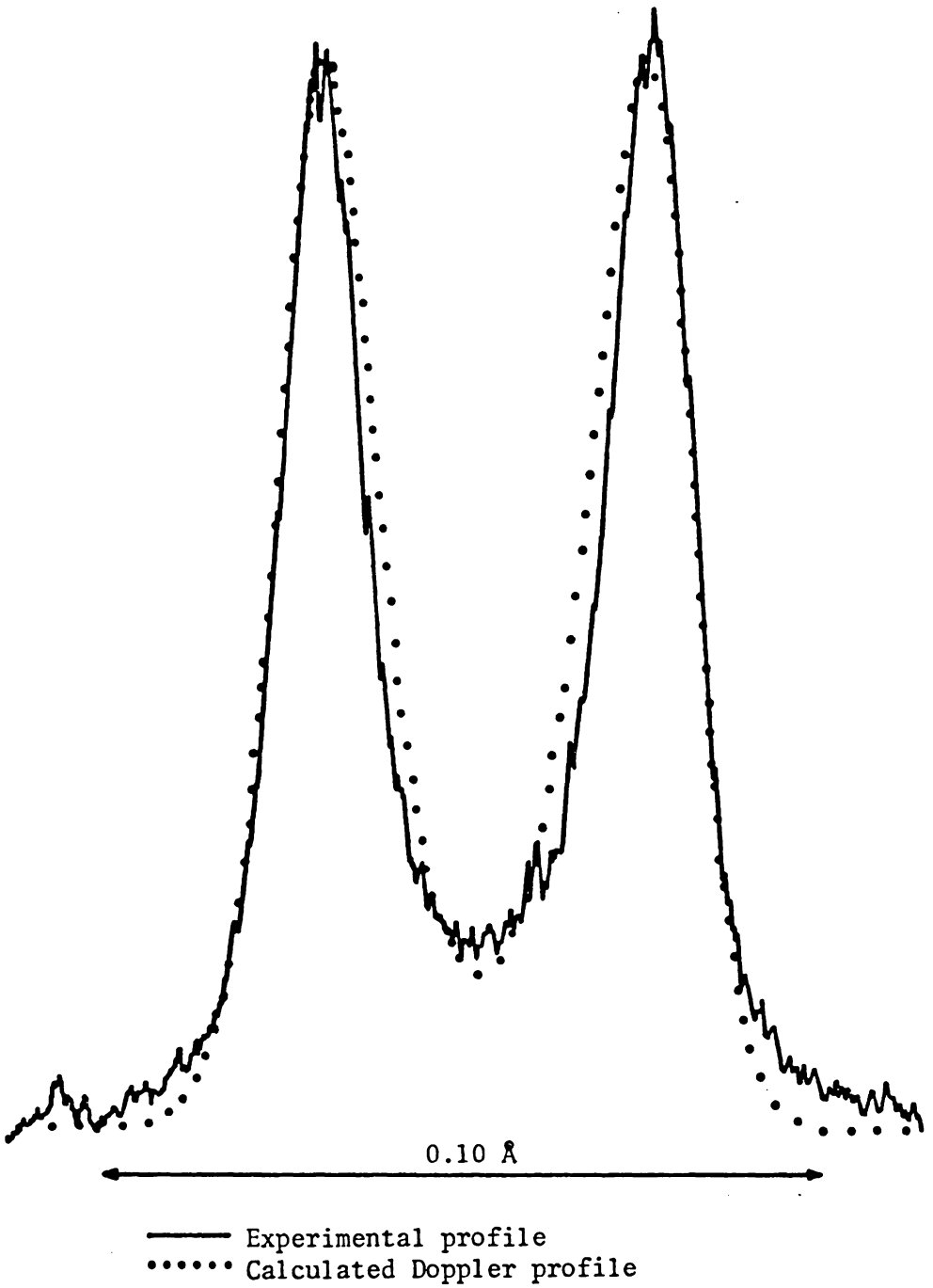

Figure 38. Lyman-α Profile for H atom, Obtained in Source B, 2.6 Torr of 0.1% H_2 in He.[65]

The disadvantage of using a deuterium source for absorption measurements is that the hydrogen atom has a relatively low absorption coefficient for deuterium radiation. In order to obtain measurable attenuation of the light source, Myerson and Watt[67] had to use a high concentration (10%) of H_2 in the test gas mixture. As a result, the enthalpy effects resulting from chemical reaction mixture caused non-isothermal conditions behind the shock wave to occur.

Myerson and Watt[67] relied on calibration procedures which employed very high temperatures (> 3000°K) to obtain equilibrium concentrations of H and D atom. However, many actual rate experiments are performed at lower shock temperatures. The reliability of extrapolating calibration data to a different range of shock gas temperature and pressure is questionable, particularly when line shape data are not available. The direct calibration technique of Appel and Appleton[68] attempted to circumvent these problems.

Appel and Appleton[68] used a novel reaction in their calibration procedure. D_2 diluted in Ar with added N_2O (0.2%) was heated over the temperature range 1800-2700°K. Reactions were:

$$N_2O \rightarrow N_2 + O, \qquad D_2 + O \rightarrow OD + D, \quad \text{and} \quad OD + O \rightarrow O_2 + D.$$

In this reaction sequence, the rapid decomposition of N_2O to form O atoms in excess ensures that all of the deuterium molecules are decomposed into atoms. Consequently, stoichiometric concentrations of D atoms can be produced at temperatures which are closer to those of interest for shock tube experiments.

Using a discharge lamp to produce deuterium atoms, Appel and Appleton first performed calibration experiments with test gas mixtures containing 0.3-50 ppm of D_2. The fractional absorption $(I_0-I)/I_0$ was plotted as a function of D atom concentration at three experimental reference temperatures, T_r = 2700°K, 2300°K, 1800°K. This model was then used to relate actual experimental shock temperatures and measured values of $(I_0-I)/I_0$ with the corresponding experimental D atom concentration produced in the shock tube for the reaction being studied. For experimental temperatures T and experimental D atom concentrations $[D]_T$, the equation which related $[D]_r$ and $[D]_T$ to $\frac{I_0-I}{I_0}$ was found to be:

$$[D]_r = [D]_T \exp\left\{(28A^{2.51} + 2](10^3/T_R-10^3/T)\right\} \text{ where } A = \frac{I_0-I}{I_0}.$$

In other words, this equation calculates the D atom concentration $[D]_r$ at the reference temperature T_r which gives the same $(I_0-I)I_0$ value as the actual experimental D concentration $[D]_T$ at the experimental temperature T.

Appel and Appleton used their technique to obtain a rate constant of $2.4 \times 10^{-10} \exp(-93400 \text{ cal./mole}/RT) \frac{\text{cm}^3}{\text{molecule sec}}$ for the reaction $D_2 + Ar \rightarrow 2D + Ar$ over the temperature range 1800-4000°K.

Just, et al.[69] studied the thermal decomposition of C_2H_4 and obtained a rate coonstant of $3.8 \pm 1.3 \times 10^{17} \exp\left(\frac{-49400 \pm 900}{T}\right) \frac{\text{cm}^3}{\text{mol sec}}$ for the reaction $C_2H_4 + Ar \rightarrow C_2H_3 + H + Ar$.

The experiments were performed at temperatures of 1700-2000°K (reflected shock) and the production of H atoms as monitored at

1215 Å. Calibration experiments were first performed at 1700-2900°K by obtaining absorption data on H atom via the reaction $H_2 + Ar \rightarrow 2H + Ar$ (50-10,000 ppm H_2 in Ar mixtures). The rate constant for this reaction, over the temperature range of interest, was taken from the literature (2.2×10^{14} exp(-48300/T)cm^3/mol sec) and used to obtain calibration curves.

An earlier paper on methane dissociation[70] provides additional background on the calibration technique used by Just and coworkers.

Lifshitz, et al.[71] designed an ultra-clean single pulse shock tube system to study the kinetics of reactions known to be catalyzed by H atom. In particular, the reaction $H_2 + D_2 \rightarrow 2HD$ was studied at 1375-1760°K for a mixture of 1% H_2-1% D_2 in argon.

Concentrations of HD and D_2 were analyzed by mass spectrometry from samples drawn from the shock tube. A comparison of the author's results with data on the H_2+D_2 reaction obtained in less clean systems suggested that the presence of H atom impurities in previous experiments was the critical factor causing the HD conversion rate, as reported in the literature, to be unexpectedly high. The authors' system made use of atomic resonance to monitor Lyman-α absorption created by the presence of H atoms during shock heating.

Ultra-pure argon (used as diluent in the test gas mixture) could be shock heated to 2500°K in their system without the detection of H atom absorption. In addition, stringent precautions were made in handling the test gas mixtures, and all gases, even if initially very pure, were further purified.

Lifshitz, et al.[71] observed that under reaction conditions where no Lyman-α absorption was detected ($\leq$ 1400°K), less than 1% HD was found from product analysis on a shocked mixture of 1% H_2-1% D_2. At higher temperatures, where Lyman-α absorption was observed, higher HD conversion was obtained.

A comparison of conventional studies on the exchange reaction indicated that for a given reaction temperature, the extent of reaction was a strong inverse function of the cleanliness of the tube. The chief source of H atoms in these studies, therefore, was very likely hydrocarbon (pump oil) impurities and impurities present in the argon diluent.

The recent study by Lifshitz, et al.[71] also provided evidence that a molecular mechanism cannot explain the bulk of experimental data on the H_2-D_2 reaction. In past experiments carried out at low temperatures (1100-1300°K), a molecular mechanism was invoked to explain the experimental observations. It was maintained that an atomic mechanism, as shown in the following reactions,

$$H + D_2 \rightarrow HD + D \qquad\qquad D + H_2 \rightarrow HD + H$$

could not explain the high yields of HD since much higher temperatures would be needed to convert H_2 to atomic H. Their conclusion here, in view of the recent study, is that an excess of H atom was indeed present in these earlier studies, but that the H atoms were generated by impurity reactions, such as those resulting from pump oil residue or diluent impurities. The virtually non-existent HD

yields found by Lifshitz, et al. under conditions in which no H atoms were detected support the idea that a molecular mechanism $H_2+D_2 \rightarrow 2HD$, proceeding via a 4 center transition state $\begin{matrix} H\text{-}H \\ \vdots \quad \vdots \\ D\text{-}D \end{matrix}$ is not likely.

Skinner and coworkers have studied several pyrolysis and oxidation reactions of hydrocarbons via atomic resonance absorption measurements on H and D atom; included are the pyrolysis of CD_4,[72] (C_3H_8 and C_3D_8)[73], and the H_2-O_2-Ar, D_2-O_2-Ar, and CD_4-O_2-Ar oxidation reactions.[74]

This group developed a novel procedure for calibrating three different lamp designs for the analysis of H or D atom.[66] (Specifically, lamp B*, with 0.1% H_2 or D_2 as the source gas, was used for the experiments mentioned above.) Their goal was to calibrate the Lyman-α source for H atom and D atom over a temperature range applicable to most shock tube experiments, about 1000-3000°K. The method of Appel and Appleton[68], which employed N_2O-D_2 mixtures to obtain stoichiometric amounts of D atom could not be used successfully for H atom work nor for temperatures much below 2000°K. Spurious H atom formation would be created by the presence of impurities (<1 ppm) at the relatively high temperatures needed to decompose N_2O for the calibration measurements.

Chiang, et al.[66] therefore decided to use the Appel and Appleton calibration technique at high temperatures and to develop calibration curves for H atoms at low temperatures (980-1140°K) by decomposing a

---

*The design of this lamp is discussed in greater detail in Section III.

mixture of 10 ppm 2,2,3,3-tetramethylbutane in Ar. The reactions involved in the formation of H atoms from C_8H_{18} have been well studied; Tsang[75] obtained rate data on $C_8H_{18} \rightarrow 2C_4H_9$ from single pulse work, Dickenson[76] studied the reactions $C_4H_9 \rightarrow C_4H_8+H$ and $C_4H_9 \rightarrow C_3H_6+CH_3$, and Clark, et al.[77] studied the recombination reaction $2\ CH_3 \rightarrow C_2H_6$. The six reactions responsible for H atom production are reported in reference 66. The concentration of H atoms produced by the reaction mechanism was calculated via numerical integration. Experimental calibration profiles which related measured values of $\ln(I_0/I)$ from absorption data with the calculated H concentrations (obtained as a function of T_5 and reaction time) were obtained. Additionally, calibration curves were calculated on the basis of previous line shape measurements and modeling of lamp parameters[78]. Good agreement was found between the calibration curves based on shock tube experiments and those calculated from measured line shapes.

The most recent application of atomic resonance absorption spectroscopy has been to characterize reactions which generate 0 atoms. Pamidimukkala, et al.[79] chose the N_2O dissociation reaction, $N_2O + Ar \rightleftarrows N_2 + O + Ar$, (1-20 ppm N_2O in Ar) to obtain 0 atoms for calibration purposes. At low (< 100) ppm concentrations of N_2O and at shocked gas pressures (1-5 atm.), the given reaction produces stoichiometric amounts of 0 atom over a wide temperature range, about 1950-2600°K. Other reactions, such as $N_2O + O \rightarrow 2NO$, $N_2O + O \rightarrow N_2 + O_2$, and $O + O + Ar \rightarrow O_2 + Ar$, are not important under these conditions.

The oxygen line profile is actually a triplet with lines centered at 1302.17, 1304.86, and 1306.03 Å. These lines, in the absence of self-absorption, have intensity ratios of 5:3:1 (i.e., proportional to the degeneracies of the J = 2,1,0 spin-orbit states) and are about the same width. Pamidimukkala, et al.[79] detected all three components by using a monochromator with 1 mm slits, centered at 1305 Å. In this way, they obtained good intensity of the transmitted lamp radiation (source gas mixture was .1% O_2 in He) during experimental runs. The radiation was detected by a solar blind photomultiplier with KBr photocathode.

Calibration curves relating O atom concentrations with measured values of ($\ln I_0/I$) were obtained for three lamp designs. Additionally, these absorption curves were calculated from line shape modeling procedures similar to the ones developed for H and D atom.[78] This involed calculating the pure Doppler profile of the line shape, and then modifying the line shape by the use of lamp absorption coefficients. In a second paper, Padmidimukkala and Skinner[80] used their procedure to study the generation of O atom in mixtures of H_2-O_2-Ar and D_2-O_2-Ar. Rate data was obtained for the following reactions:

(3) $H + O_2 \rightarrow OH + O$

(5) $H + O_2 + Ar \rightarrow HO_2 + Ar$

(3D) $D + O_2 \rightarrow OD + O$

(5D) $D + O_2 + Ar \rightarrow DO_2 + Ar$

(4) $O + H_2 \rightarrow OH + H$

(4D) $O + D_2 \rightarrow OD + D$

The substitution of D atom for H atom for reactions (3), (4), and (5) enabled isotope effects to be detected and compared with earlier work which studied these effects from H and D atom measurements.

Roth and Lohr[81] analyzed for both H and O atom to obtain kinetic data on two reaction systems,

$$\text{HCN} + \text{O} \xrightarrow{(1a)} \text{OCN} + \text{H}$$

$$\xrightarrow{(1b)} \text{CN} + \text{OH} \qquad T = 1700\text{-}2500^\circ\text{K},$$

and

$$\text{C}_2\text{H}_2 + \text{O} \xrightarrow{(2a)} \text{C}_2\text{HO} + \text{H}$$

$$\xrightarrow{(2b)} \text{CH}_2 + \text{CO} \qquad T = 1500\text{-}2575^\circ\text{K}.$$

Roth and Lohr's work is the first high temperature study of these two reaction schemes. O atom was generated by doping the HCN and C_2H_2 mixtures with small (ppm) amounts of N_2O. The H atom and O atom absorption measurements were carried out independently. The H atom measurements were done at the lower end of the given temperature range.

Kinetic modeling was performed to compare calculated atom concentrations with experimental H and O atom concentration-time profiles. In both reaction schemes, additional reactions led to better agreement of calculated and experimental data at late times (> 800 μsec). However, good agreement was found for a simple kinetic scheme based on the reactions presented above, in which both HCN + O and C_2H_2 + O systems react via a two channel mechanism.

C. The Pyrolysis of Neopentane - Single Pulse Shock Tube Experiments

To date, the pyrolysis of neopentane has been studied in single pulse shock tube experiments. Tsang[82] studied the decomposition with a shocked mixture of 0.025% neopentane in argon with 1% toluene. Comparative rate measurements were performed, in which the formation of propylene (C_3H_6) from 2,3 dimethylbutane[83] was used as the standard reaction. This standard reaction is: $C_6H_{14} \xrightarrow{k_D} 2i\text{-}C_3H_7 \rightarrow 2C_3H_6 + 2H.$

Experiments were carried out by shocking mixtures of neopentane in argon with 1% toluene* and then repeating these experiments with 0.02% of 2,3 dimethylbutane added to the reaction mixture. The main reaction product from the neopentane was isobutene ($i\text{-}C_4H_8$) and its rate of formation was calculated from the equation:

$$\log k_N(i\text{-}C_4H_8) = (1.024\pm.004) \log k_D(C_3H_6) - (.0429\pm.0005)$$

where

$$k_D(C_3H_6) = 10^{16.13} \exp\left(\frac{-76200 \frac{cal}{mole}}{RT}\right) sec^{-1}.$$

In this way, a rate constant of $10^{16.1} \exp\left(\frac{-78200 \text{ cal./mole}}{RT}\right) sec^{-1}$ for the process $C_5H_{12} \rightarrow C_4H_9+CH_3 \rightarrow i\text{-}C_4H_8+H+CH_3$ was determined. In addition, about 10% of the neopentane reacted by the process $C_5H_{12} \pm C_4H_9+CH_3 \rightarrow C_3H_6+2CH_3$. The extent of reaction for the neopentane + 2,3 dimethylbutane runs was kept low.

---

*The toluene was added to tie up highly reactive H atoms via the reaction $H + C_7H_8 \rightarrow H_2 + C_7H_7$.

Bradley[84] studied the pyrolysis of neopentane at 1030-1300°K and in addition, modeled the reaction mechanism to obtain the given rate constants for the reactions:

$$C_5H_{12} \rightarrow C_4H_9 + CH_3 \qquad k = 3.3 \times 10^{16} \exp(-336 kJmol^{-1}/RT) sec^{-1}$$

$$CH_3 + C_5H_{12} \rightarrow CH_4 + C_5H_{11} \qquad k = 6.6 \times 10^{11} \exp(-90 kJmol^{-1}/RT) dm^3 mol^{-1} sec^{-1}$$

$$H + C_4H_8 \rightarrow C_4H_9 \qquad k = 1.6 \times 10^{10} \exp(-6.3 kJmol^{-1}/RT) dm^3 mol^{-1} sec^{-1}.$$

Experiments were performed in mixtures of 0.1%, 0.5% and 1.0% neopentane. Some additional runs were performed with 1.0% neopentane plus 100, 500 and 1000 ppm O_2; the presence of O_2 did not affect the experimental results. The reaction products were analyzed by gas chromatography and were found to be comprised chiefly of isobutene, ethane, and methane.

In modeling the reaction mechanism, Bradley considered a series of 28 reactions. He attempted to match the computed yields of major products with the experimental yields by varying critical rate constants; however, he found it impossible to duplicate the experimental ethylene yield without considering an additional reaction, one of the so-called "forbidden isomerizations" reactions, namely $C_4H_9 \rightarrow C_2H_4 + C_2H_5$.

II. EQUIPMENT AND APPARATUS

A. The Shock Tube System

The shock tube consists of an aluminum driver section, 3.3 m long with 6.3 cm inner diameter and a stainless steel test section, which is 4.5 m long with an inner diameter of 7.5 cm. At the site at which diaphragms were inserted, a 6.3 cm square cross section was constructed which made a transition to round on either size. A plunger, which extended the length of the driver section, allowed the diaphragms to break at a constant pressure (60 psi) for our experiments.

The window mount sites on both sides of the shock tube, and transducer mounting plates are sealed with gold wire gaskets. Other seals use Viton 0 rings. The test section is wrapped with heating tape and can be baked out to about 100°C while under vacuum.

B. The Gas Handling System

The shock tube gas handling system and manifold are shown in Figures 39 and 40. The shock tube is evacuated by a Leybold-Heraus turbomolecular pump and a Welch Duo-Seal mechanical pump equipped with a foreline trap. The driver pressure is monitored by a USG gauge, 0-200 psi. The test section pressures are monitored via a Penning gauge (P_2 in Figure 39) mounted below the gate valve on the turbomolecular pump. A CVC (model 6PH-320B) controller permitted the monitoring of pressures ranging from 25×10^{-3} to 1.0×10^{-6} torr for the tube and manifold. During normal operation, it is usual to evacuate the shock tube to a pressure of 2×10^{-5} torr. A Validyne AP-10-42 pressure transducer

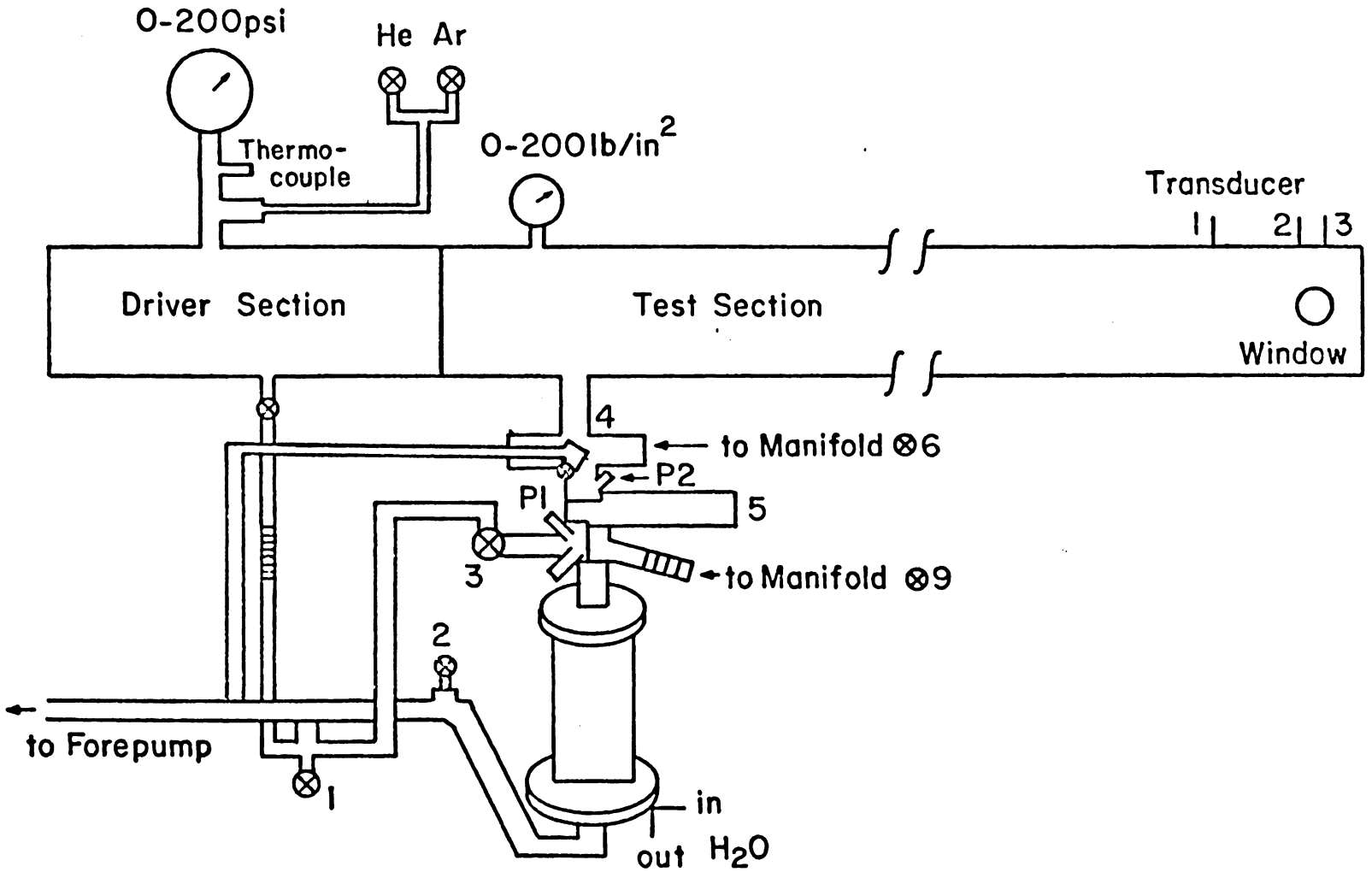

Figure 39. The Gas Handling System.

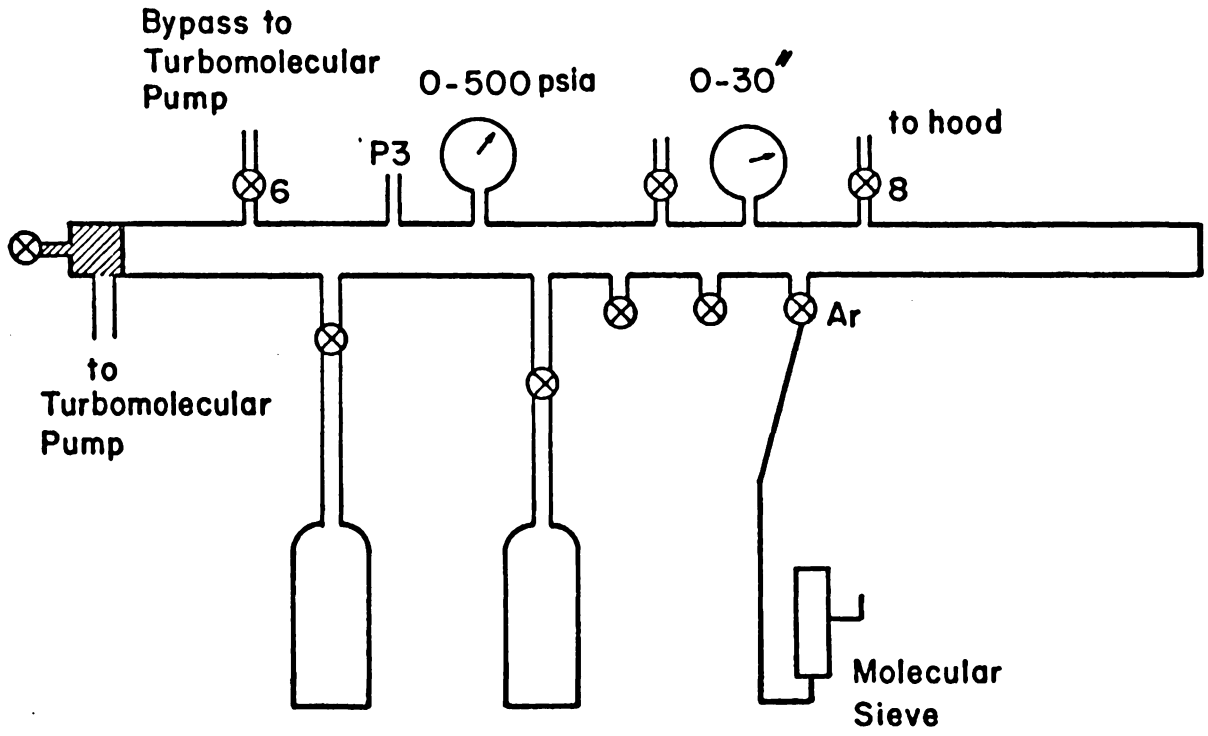

Figure 40. The Gas Mixing Manifold.

mounted on the end of the test section is used to measure the test gas pressure P_1 before a shot is fired.

The stainless steel manifold used to make up gas mixtures is evacuated by the turbomolecular pump. A Penning gauge (P_3 on Figure 39) monitors the manifold pressure. The manifold is equipped with a Heise model C gauge (0-500 psi) and a USG gauge (0-30") to monitor gas pressures when gas mixtures are made up.

C. Diaphragms

Aluminum diaphragms (.5 mm thick) are stamped with an X cut to a depth of 0.2 mm. The center of the X makes contact with the plunger tip when a shot is performed, and the diaphragm breaks into four petals which then face the test section. The diaphragm station with a broken diaphragm is depicted in Figure 41.

D. System for Shock Speed Measurement

The test section of the shock tube is fitted with three Kistler 603-A piezoelectric transducers. The first two are located 38.1 cm apart, with the second located 7.0 and the last 2.0 cm from the end of the test section. The voltage signal from each transducer is amplified by a Kistler charge amplifier. The amplified signals from the first and second transducers are used to stop and start an HP 5233 L Electronic Counter. In this way, the time of shock wave passage between the two markers is monitored. The third transducer is used to monitor the shocked gas pressures P_2 and P_5. The pressure

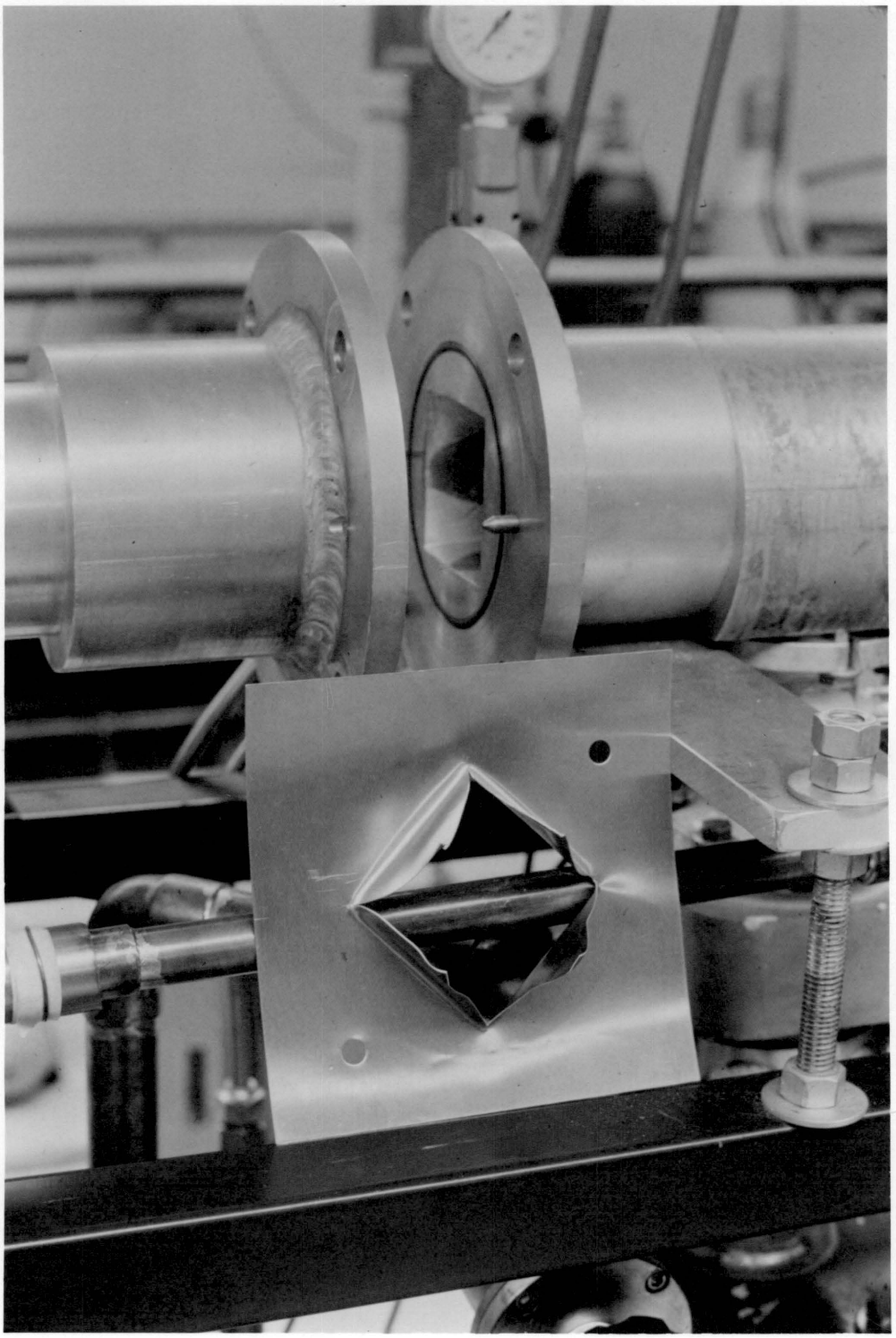

Figure 41. The Diaphragm Station.

trace is then recorded on a strip charge recorder.

E. Optical and Detection System

In this experiments presented in this work, discharge lamp B is used. It is shown in position against the shock tube in Figure 42, and is drawn schematically in Figure 43. The lamp is constructed of an 8 cm long piece of fused quartz tubing (1.3 cm o.d., .7 mm i.d.). Metal flanges are attached using Torr-Seal (Varian) to each end of the tube. An MgF_2 window (Harshaw Chemical Company, 2 mm thick) was sealed into one end of the tube for insertion into the side wall of the shock tube. In lamp B, the Evenson-Broida microwave cavity (Opthos Instrument Company) is located 3.5 cm from the window. The cavity is powered by a Scintillonics HV15A microwave generator.

Gas mixtures for the lamp flow into the quartz tube via a side hole in the metal flange near the window. The gas pressure, typically 2.5 mm, is measured by a Wallace and Tiernan gauge (model FA-160, 0-50 mm). A tie joint connects the lamp tube and guage to a roughing pump. A valve between the lamp gas sample cylinder and the metal flange near the shock tube window controls the gas pressure.

The Lyman-α radiation created in the discharge lamp leaves the shock tube through another MgF_2 window; the optical path is consequently perpendicular to the shock tube. The light then enters the housing of a GCA McPherson Scanning Monochromator (model 218). The entrance port of the monochromator, as shown in Figure 44, fits against the exit window of the shock tube so that the collection of

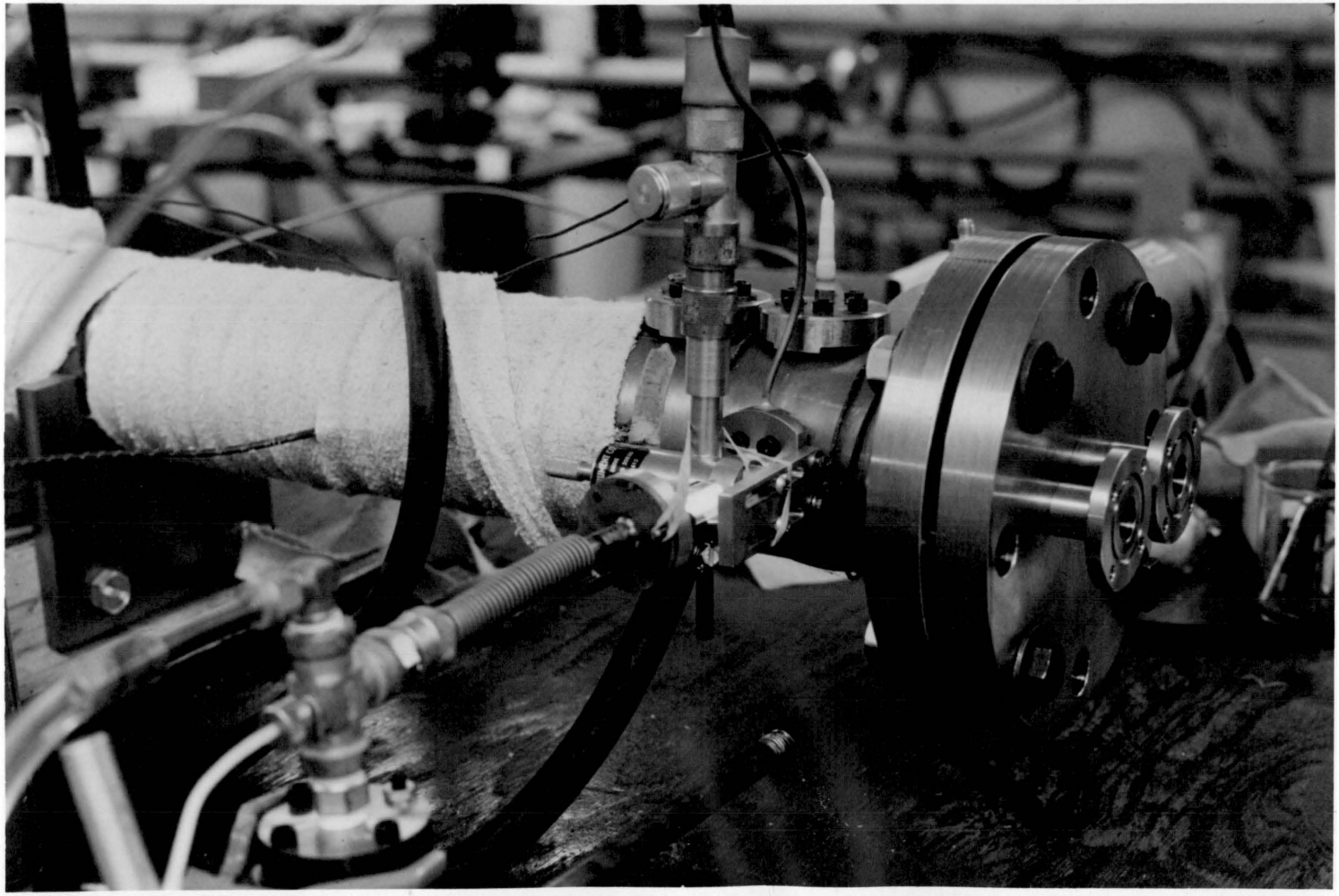

Figure 42. The Lyman-α Source.

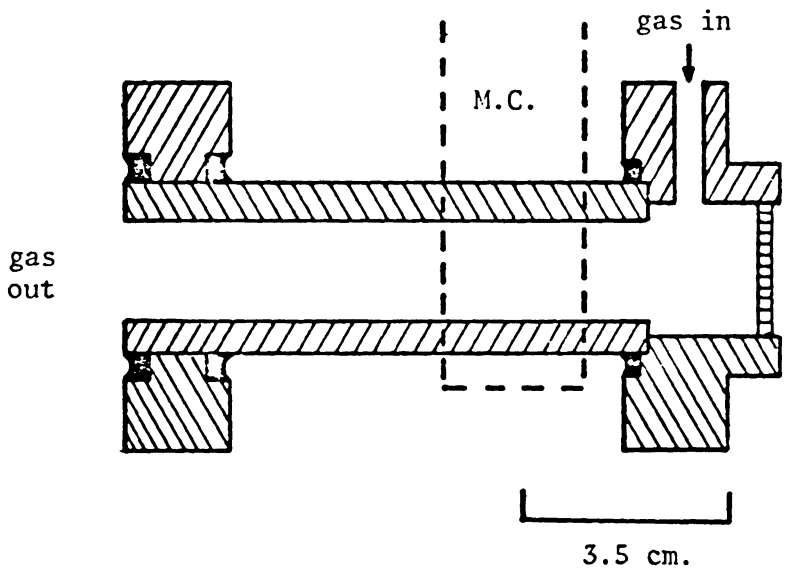

M.C. is the microwave cavity

Figure 43. Schematic of Lyman-α Source B.

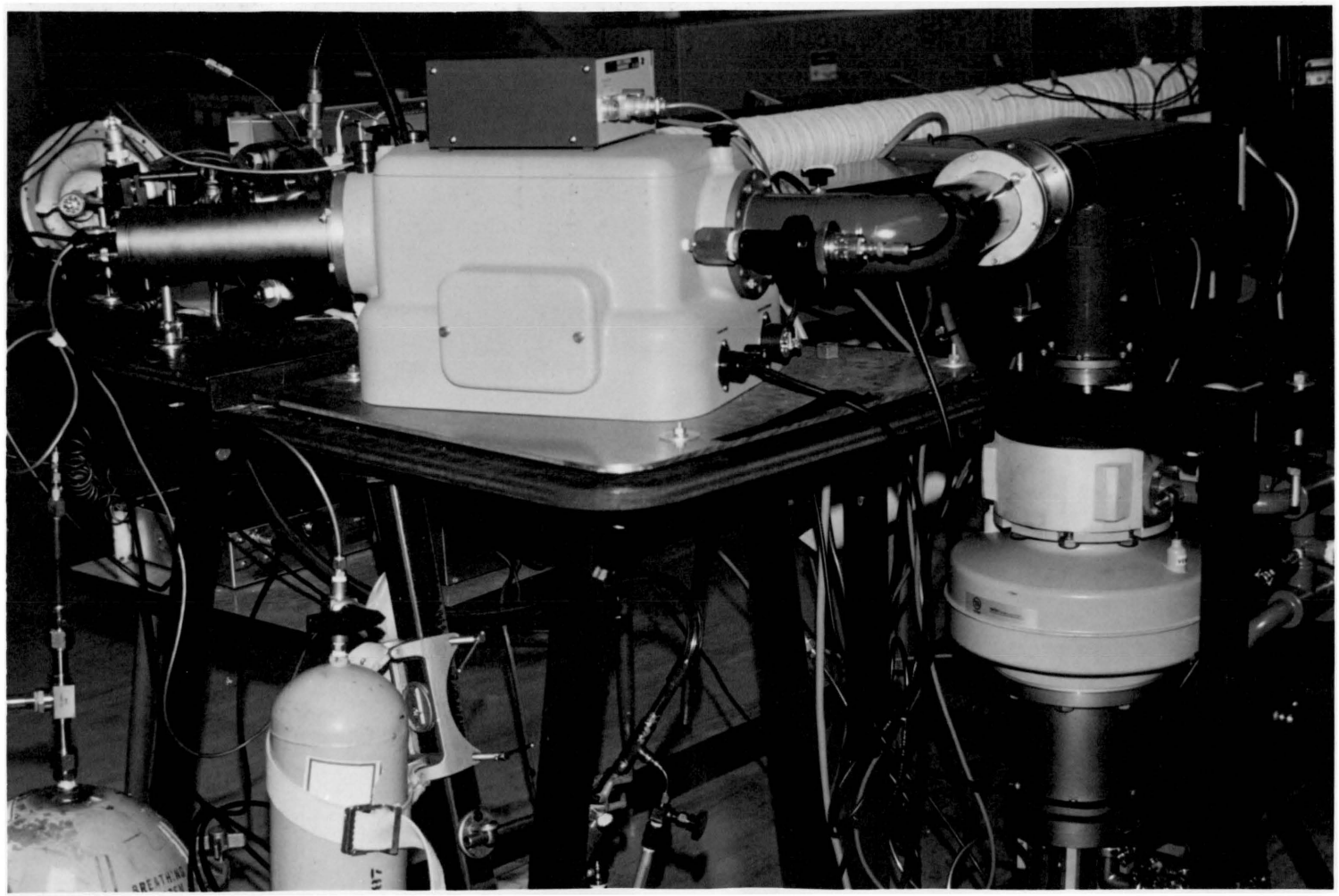

Figure 44. The Monochromator.

light is optimized. With a grating blazed at 5000 Å, the monochromator is set at 4868 Å, the setting of highest intensity for the Lyman-α radiation when a scan of intensity versus wavelength is performed. Therefore, it is the 4th order spectral maximum (1215.6 Å x 4) which is monitored. The slit width was 1 mm, corresponding to a dispersion of $\frac{7Å}{mm}$ in the 4th order.

A solar blind photomultiplier (EMI-Gencom Inc. Type 6-262315) was used to detect the light signal. An EMI-Gencom high voltage supply (model 205A-25R) was used over a range of 2000-2600 volts to vary the magnitude of output current. In this way, a voltage signal of reasonable magnitude could be viewed on the storage oscilloscope (Gould, model 205A-05R). Typically, the intensity traces were viewed on channel 2 of the scope. Time constant settings of 10 or 20 μsec, controlled by an external filtering circuit, were used to smooth the current signal before it was sent to channel 2.

For some experiments, the monochromator was replaced by a commercial Lyman-α filter (Acton Research, Inc., having 13% transmission at 1215 Å). Light exiting the shock tube window passes through the filter into the photomultiplier housing. Additional extraneous radiation near Lyman-α was removed by a gas filter consisting of 8 cm of dry air at atmospheric pressure; this is described in greater detail in Section IIIB.

III. EXPERIMENTAL

A. Prepartion of Gas Mixtures

1. General Procedure

In preparing any gas mixture, the gas cylinders for the mixture are attached to the manifold and evacuated by the turbomolecular pump to about 10^{-5} torr. Gas cylinders which are suspected to contain traces of vapor from previous experiments are flushed with argon prior to their use. Additionally the cylinders can be heated with a heat gun while they are being evacuated on the manifold.

It is very important, especially when very dilute (3-10 ppm) mixtures are being made, to ensure that the manifold system is free from impurities. The manifold was generally baked out for about two hours, and then allowed to pump down further with the gas cylinder (to be used for the mixture) open. The manifold itself would be baked again, and then the entire system (manifold and gas cylinder) would be evacuated to pressures $\sim 10^{-5}$ torr. Argon is used to initially flush out the baked manifold prior to any mixing.

A few torr of the diluent gas (for example, Ar or He) is allowed into the evacuated gas cylinder prior to the addition of any compound. In this way, the inert gas absorbs onto the active sites of the inner wall of the gas cylinder and reduces sticking and readsorption of the compound vapor. Argon is purified before use by allowing it to flow through a small container of Type 4A and 5A molecular sieve material (Linde, Inc.), which has been mixed in equal parts. The container of molecular sieve is surrounded by a

dewar of crushed dry ice.

Sample is then admitted to the cylinder. Argon is used to clean the manifold of traces of compound vapor after its addition to the gas cylinder. Additional argon is used to bring the mixture to a total pressure of 100 psi. The concentrations are based on pressures, as read on the two manifold gauges depicted in Figure 40. Dilute mixtures are made by diluting more concentrated mixtures; in general, two dilutions are performed to obtain the final mixture. The maximum dilution factor is 200.

2. Preparation of 2,2,3,3 Tetramethylbutane for Calibration Runs

0.333 g tetramethylbutane (Pfalz and Bauer, Inc.) was weighed in a test tube, connected to the gas manifold by means of a Manolok connector, and frozen in a liquid N_2 bath for about two hours. The dewar of N_2 was then removed and the tube was allowed to come to room temperature.

4.1 torr of vapor was obtained by heating the tube very gently with a heat gun. The vapor pressure was monitored by a pressure transducer attached to a manifold line. Ultra pure argon (< .5 ppm hydrocarbons), which had been purified in the dry ice bath, was added to the gas cylinder until a total pressure of 100 psi was obtained. The final concentration of mixture was therefore,

$$\frac{4.1 \text{ torr}}{100 \text{ psi}} = \frac{.079 \text{ psi}}{100 \text{ psi}} = .079\%.$$

The 10 ppm and 5 ppm mixtures of 2,2,3,3 tetramethylbutane were made by appropriate dilutions of the 0.079% mixture.

3. Preparation of Lamp Mixtures - 0.1% H_2 in He

Ultra pure H_2 (Matheson, hydrocarbons < .5 ppm) and grade 5 He are used for the preparation of source mixtures. Typically, a mixture of 2% H_2 in He is first prepared, and then this mixture is diluted to .1% H_2 in He.

For example, a 2% mixture would be $\frac{2 \text{ psi } H_2}{100 \text{ psi total}}$. Five psi of the 2% mixture, diluted to 100 psi total pressure with He, makes a .1% mixture of H_2 in He.

4. Preparation of Neopentane Mixtures

Neopentane (Matheson Co.) contained 2.1% n-butane as the major impurity as determined by gas chromatography. The next largest impurity was cis-2-butene. A 1% mixture of neopentane in Ar was first prepared. Successive dilutions from 1% neopentane in Ar → 500 or 200 ppm neopentane in Ar → 20, 10, 5 ppm. neopentane in Ar were performed.

B. Shock Tube Experiments

1. General Procedure

In order to obtain shock tube data over the desired temperature reange, the tailored interface method[16] is used with our apparatus. This technique ensures that the reflected shock, as it moves back into the heated gas after reflection from the endwall, will pass through the contact front with minimal interaction. The test time is extended until the rarefaction wave arrives from the driver end of the shock tube, to approximately 1.5 milliseconds. Otherwise, the

time for uniform conditions of temperature and pressure to be maintained would be less, and the interaction of the reflected shock wave with the contact front would create re-reflected waves, with charges in shocked gas temperature and pressure.

Typically, a constant driver composition (generally ∿10 psi. Ar diluted to a total of 60 psi with He) is maintained while P_1 is varied shot-by-shot by increasing or decreasing the amount of sample gas in the test section. In this way, the shocked gas temperature obtained is a function of P_1; as P_1 increases, T_5 (reflected shocked gas temperature) decreases.

The basic experimental procedure for firing a shot involved evacuating the monchromator* (to $\sim 10^{-5}$ torr) and evacuating the shock tube and associated sample lines to about 2×10^{-5} torr via the turbomolecular pumps. The electronics were turned on and warmed up for about 30 minutes prior to any experimental runs. The driver section of the shock tube was partially filled (to about 40 psi) with the desired amount of Ar diluted up to 40 psi with He.

The Lyman-α source was then activated by arcing the lamp, which contained a flowing mixture of .1% H_2 in He, at 2.5 torr pressure, with a Tesla coil. The source operates at 40 watts microwave power.

---

*in later experiments (described in Section III) which utilized the 10% quantum efficiency photomultiplier tube, use of the monochromator decreased the detected light signal to the extent that the signal to noise ratios of recorded pictures were poor. Consequently, we later substituted a Lyman-α filter for the monochromator to allow higher emission intensities to reach the photomultiplier.

Ions and electrons must be present within the source gas before the microwave radiation can be absorbed to create the Lyman-α emission. Thus, the Tesla coil arc starts the process, and collisions of ions and electrons with the H_2 create the excited H atoms. This procedure, in which the lamp is lit for a few minutes prior to firing a shot, allows it to stabilize.

The photomultiplier voltage is then adjusted and the storage scope is armed in preparation to firing the shot. Additional helium is added to the driver to give 60 psi total pressure. While this latter step is carried out, the shock tube is closed off via the turbomolecular pump gate valve. Sample gas is then introduced into the test section through the endplate. To fire the shot, the diaphragm is pricked by pushing the driver plunger forward. After the shot is performed, both the pressure trace and absorption intensity trace, as stored by the oscilloscope, are recorded onto strip chart paper. Scope baselines for the pressure and intensity traces are then made for the next shot.

Prior to actually doing reactive experiments, the cleanliness of the tube, with respect to H atom-producing impurities, was checked by shocking argon to the highest temperature at which the reactive studies were to be performed. Also, argon shots were sometimes done after a series of reactive experiments to check whether there was build-up of impurities on the shock tube walls. A good argon shot showed a flat (constant) intensity trace, without any absorption of lamp emission due to spurious sources of H atom.

Additionally, for the neopentane runs, the shock tube was baked out every few days to aid in the removal of deposits from the walls and endplate. After a day's work was completed, the shock tube was evacuated and sealed off. This allowed faster evacuation for the next day's work than when argon was permitted to fill the tube and remain in the tube overnight.

2. Calculation of Shock Parameters

The T_5 and P_5 values obtained for all shock experiments in this work were calculated from an iterative shock program based (refer to Part I, page 14) on the conservation equations, ideal gas relations, and enthalpy data for the components of the mixture in question. The basic program does the following:

1. The experimentally obtained shock speed is used to calculate PRESS = $U_1 \times U_1 \times 0.745$ (empirical equation). The value 0.745 is an empirical constant that is approximately correct for the types of gas mixtures we are using. This equation is used to start the iteration process.

2. RHO, U_2, DHC1 (a function of U_1 and U_2), TEMP = PRESS/RHO and T_2 are thereby obtained.

3. DHC2 is calculated via T_2 and the enthalpy equation $A + BT_2 + CT_2^2 + D = H(T) - H(298)$ for the compositions of gas mixture under study.

4. DELHC is obtained as DHC1 - DHC2. The absolute value of DELHC

must be <.001 for the calculation to be good; if so, reflected shock parameters P_5 and T_5 are calculated from the incident shock parameters. If DELHC is not <.001, it is used to obtain a new PRESS, and the incident shock calculations are repeated until DHC1-DHC2 < .001.

Here, PRESS = P_1/P_2, RHO = $\frac{\rho_2}{\rho_1}$, U_2 = dimensionless particle velocity in incident shock region, DHC1 and DHC2 are dimensionless heat content, $\frac{H_2-H_1}{RT_1}$.

3. Absorption Data

A typical shock picture, shown in Figure 45, has the following features. Region B shows the increase in absorption of Lyman-α radiation by the molecule under study, as compression of the gas to reflected shock conditions occurs. Time = 0 for the reflected shock is indicated on the picture. At t = 0 the concentration of molecule = $\frac{P_5 \text{fract}}{RT_5}$, where fract is the mole fraction of molecule in the original test gas mixture. Region C shows the absorption of radiation by H atoms, which absorb Lyman-α emission.

The scope baseline, which shows the voltage level obtained when no light from the source reaches the detector, would be reached if there was complete absorption of the source radiation by the heated test gas mixture. In reality, we find that the intensity signal never reaches the baseline, even when high concentrations of test gas mixture are shocked at high temperatures, to produce very large concentrations of H. A residual amount of stray light is always detected. Consequently, in data analysis, the chart baseline is corrected (moved up) for this

residual radiation. High temperature shots are used to determine the amount of baseline correction.

4. Calibration Experiments

One of the largest sources of error in our experimental data is due to uncertainties in the calibration curves. Experiments similar to those of Chiang (reference 66) were carried out at two compositions of C_8H_{18} in Ar (5 ppm and 10 ppm) to check the reproducibility of the data reported in reference 66. The experimental results are tabulated in Table 16. Figure 45 is a typical calibration picture.

The calibration data were taken with a photomultiplier tube having a high (20%) quantum efficiency. Therefore, the majority of these pictures showed good signal to noise ratios, and the time = 0 point could be located directly on the picture, as shown. I_0 (H atom) and I (at t = 0.164 msec) are indicated on the picture. The noise of the absorption curve has been smoothed by the use of a french curve. In order to plot the calibration data, the absorbances taken at various times t were correlated with their respective values of H atom concentration [H] (see Table 16). The H atom concentrations were obtained via computer simulation of the reaction mechanism as indicated in Table 15, which in turn is based mainly on the work of Tsang[75]. Actually, only reactions 1, 2 and 5 affected the H concentrations significantly, the others being included mainly to check on their importance. The pictures that were selected from the original batch for subsequent data analysis are tabulated in Table 15 and plotted in

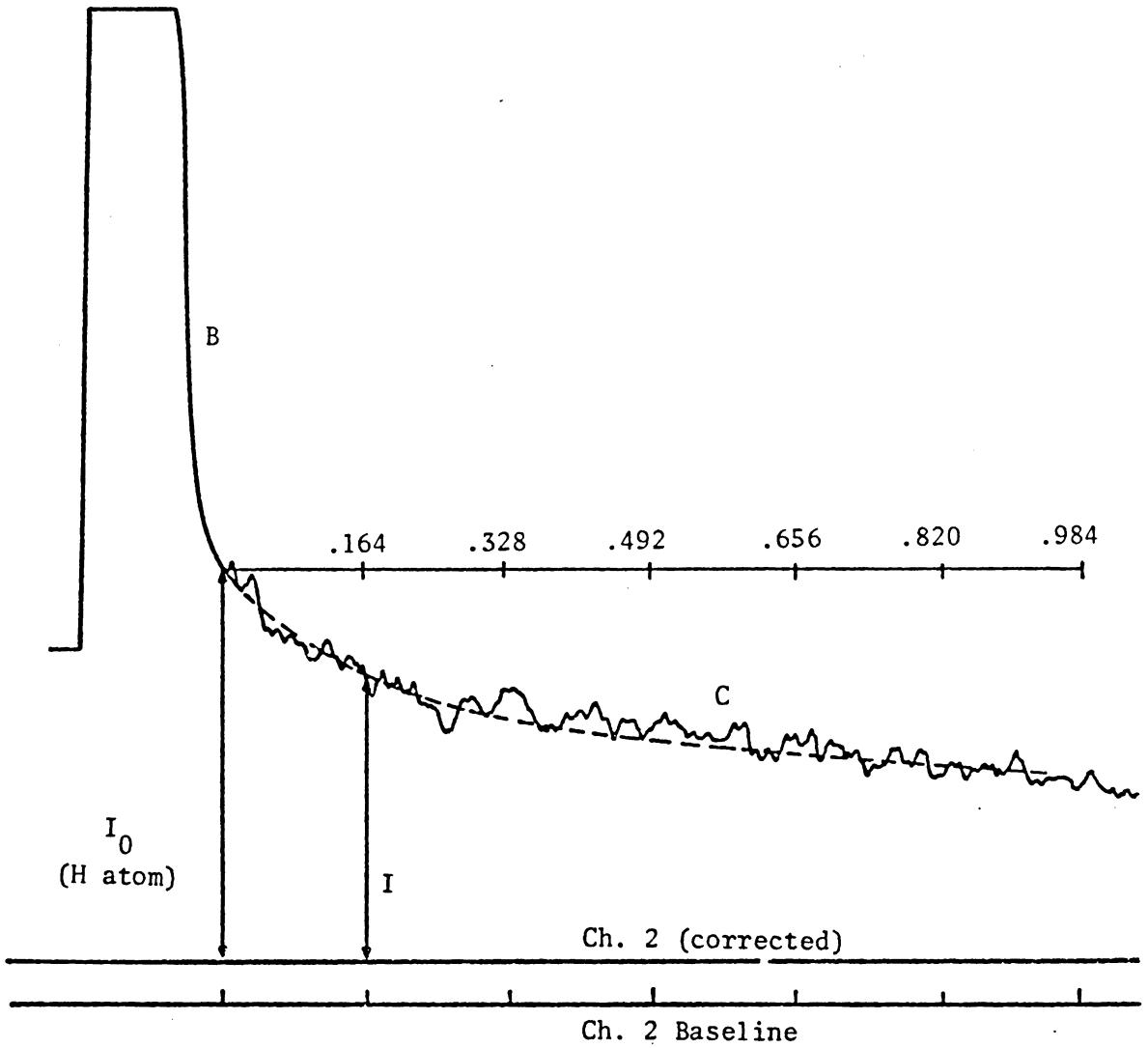

time axis = .164 msec/inch, time constant = 20. The scope baseline is shown as corrected for stray light.

Figure 45. Calibration Run: Aug. 4, #8, T_5 = 1014.4°K.

Table 15. Rate Constants Used in Computer Simulation of C_8H_{18} Decomposition Mechanism.[66]

Reaction	Rate Constant A*	E_a (kcal./mole)
1. $C_8H_{18} \rightarrow 2C_4H_9$	2.0×10^{16}	68.5
2. $C_4H_9 \rightarrow C_4H_8 + H$	1.0×10^{15}	43.6
3. $2CH_3 \rightarrow C_2H_6$	8.4×10^{12}	0.0
4. $C_4H_9 \rightarrow C_3H_5 + CH_3$	2.0×10^{14}	46.3
5. $H + C_6H_{18} \rightarrow C_8H_{17} + H_2$	1.0×10^{14}	7.8
6. $C_8H_{17} \rightarrow C_4H_8 + C_4H_9$	2.0×10^{16}	58.5

*sec^{-1} for first order reactions, $\frac{cm^3}{mol\ sec}$ for second order reactions

Table 16. Selected Calibration Data

Run	Temp (°K)	Time (msec)	$\ln(I_0/I)$	$[H]^* \times 10^{12}$ $(\frac{mole}{cm^3})$
10 ppm C_8H_{18} in Ar				
Aug. 4, #5	1014.4	.164	.33	3.04
Aug. 4, #6	1023.3	.164	.47	4.01
		.328	.74	7.75
Aug. 4, #7	1041.5	.328	.58	13.8
		.492	.73	20.3
Aug. 4, #8	1014.4	.164	.36	3.04
Aug. 5, #3	1038.1	.164	.30	6.47
		.328	.50	12.6
5 ppm C_8H_{18} in Ar				
Aug. 10 #2	995.7	.656	.39	3.25
		.82	.49	4.01
Aug. 10 #4	1021.9	.492	.52	5.8
		.656	.70	7.65
		.820	.91	9.47
		.984	1.11	11.27
Aug. 10 #6	1004.3	.492	.31	3.18
		.656	.41	4.18
		.820	.56	5.17
Aug. 10 #7	1010.4	.328	.26	2.59
		.492	.41	3.82
		.656	.56	5.04
		.820	.74	6.24
Aug. 10 #8	1010.7	.492	.41	3.79
		.656	.62	4.99
		.820	.85	6.18
		.984	1.02	7.36
Aug. 10 #9	1040.8	.328	.41	6.82
		.492	.62	10.10
		.656	.85	13.31
		.820	1.02	16.44
Aug. 10 #10	1043.9	.246	.614	5.73
		.328	.780	7.58
		.410	.907	9.41
		.492	1.08	11.21
		.656	1.39	14.76

*H atom concentrations were calculated via the reaction mechanism of Table 14.

Table 16, continued

Run	Temp (°K)	Time (msec)	$\ln(I_0/I)$	$[H]^* \times 10^{12}$ $(\frac{mole}{cm^3})$
Aug. 10 #11	1019.6	.492	.55	5.29
		.656	.73	6.98
		.820	.89	8.65
		.984	1.08	10.29

*H atom concentrations were calculated via the reaction mechanism of Table 14.

Figure 46. The values of $\ln(I_0/I)$ versus H atom concentration agree well with the data of reference 66 at the lower concentrations. By a statistical test, it was shown that the two sets of data agreed within their standard deviations. Figure 46 also shows the calibration curve for H atom at 1000°K.

5. Neopentane Experiments

These experiments can be divided into two sets of data. The first set of runs, using a test gas mixture of 20 ppm neopentane in Ar, were performed with the monochromator and photomultiplier tube set-up. The second set of runs (20, 10, 5 ppm neopentane in Ar) were performed with a Lyman-α filter instead of the monochromator; the same photomultiplier was utilized.

The Lyman-α filter provided several advantages over the monochromator for the latter experiments. The photomultiplier tube previously used for the calibration runs (20% quantum efficiency) cracked and was replaced by a tube having a quantum efficiency of 10%. The resulting pictures showed more noise. We were also faced with the problem that in using the monochromator, photomultiplier voltages ∿2200 volts were needed to get sufficient voltage gain for the intensity trace. The probability of arcing is higher at these elevated voltages. Consequently, the second set of experimental runs was performed with a commerical Lyman-α filter used in conjunction with an 0_2 molecular filter.[68]

In the 0_2 technique, a stream of dry air is allowed to flow

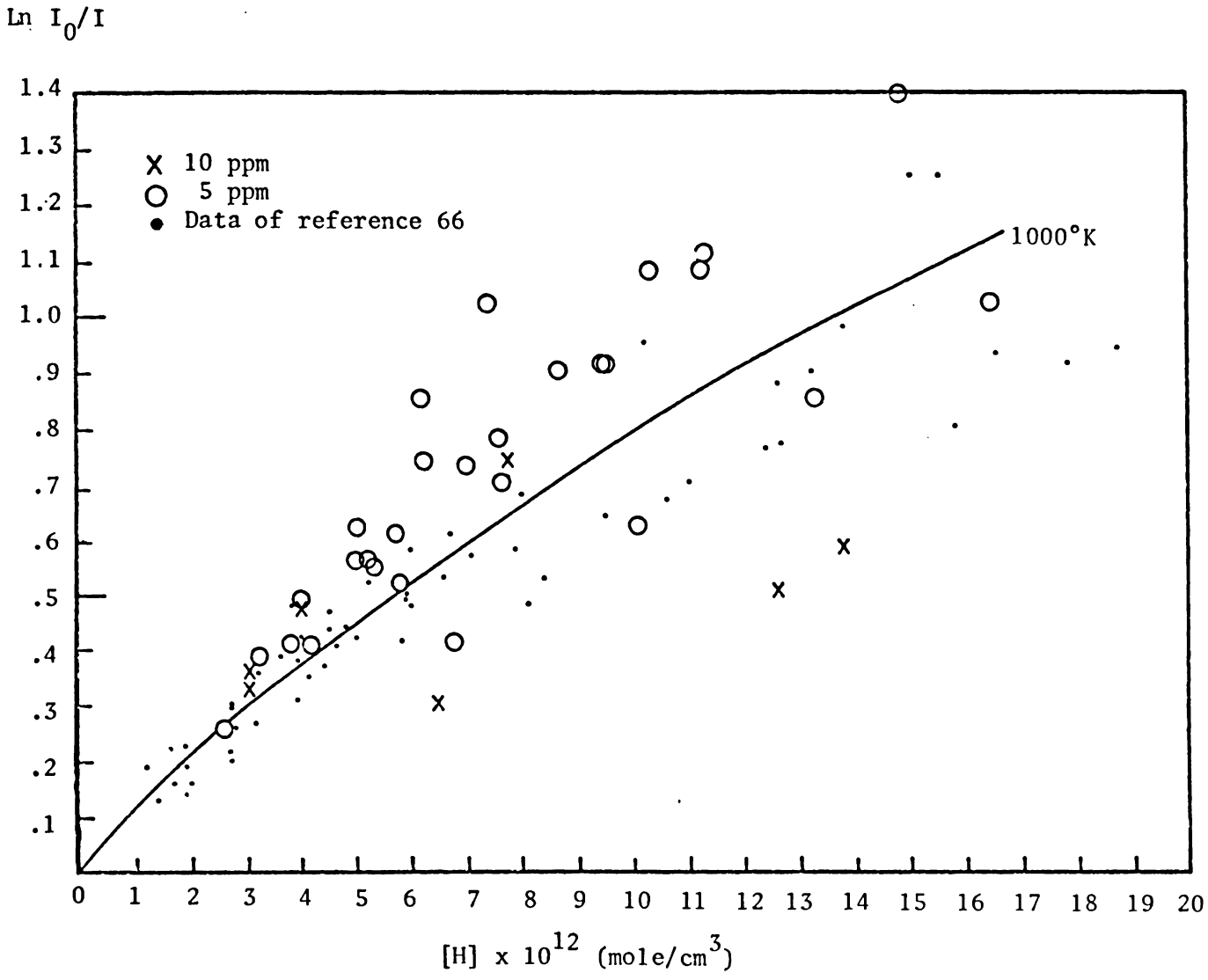

Figure 46. C_8H_{18} Calibration Data.

through a tube 8 cm long between the shock tube and the photomultiplier. The O_2 component absorbs much of the extraneous radiation produced by the discharge lamp below 1800 Å. The total emission spectrum from the lamp is over a wide wavelength range, including the visible, where the Balmer lines of H can easily be seen. There is a great deal of emitted radiation other than Lyman-α from the various chemical species (ions and molecules) produced in the discharge. Figure 47 shows the transmission of the Lyman-α peak (at 1215 Å), which lies at a minimum in the absorption spectrum of O_2. The only other major peak not absorbed in the range 1100-2000 Å is at about 1600 Å. The additional use of a commerical Lyman-α filter on our system further prevented other potential sources of radiation from passing through to the detector. In fact, the baseline corrections for the Lyman-α filter set up were less (about 10%) than similar corrections for data using the monochromator as a filtering device. Figures 48a and 48b show graphs of the Lyman-α filter transmittance and the photomultiplier sensitivity for our KBr cathode.

The double filter arrangement still allowed higher intensities of source radiation to pass through and this compensated for the lower quantum efficiency of the new photomultiplier tube. Good voltage gain and traces of good signal-to-noise ratio could still be obtained. Additionally, we could operate the photomultiplier tube at lower voltages, on the order of 1400-1600 volts, and thereby greatly lessened the potential of the tube to arc. The tube lifetime is a function of operating voltage and therefore, these lower voltage

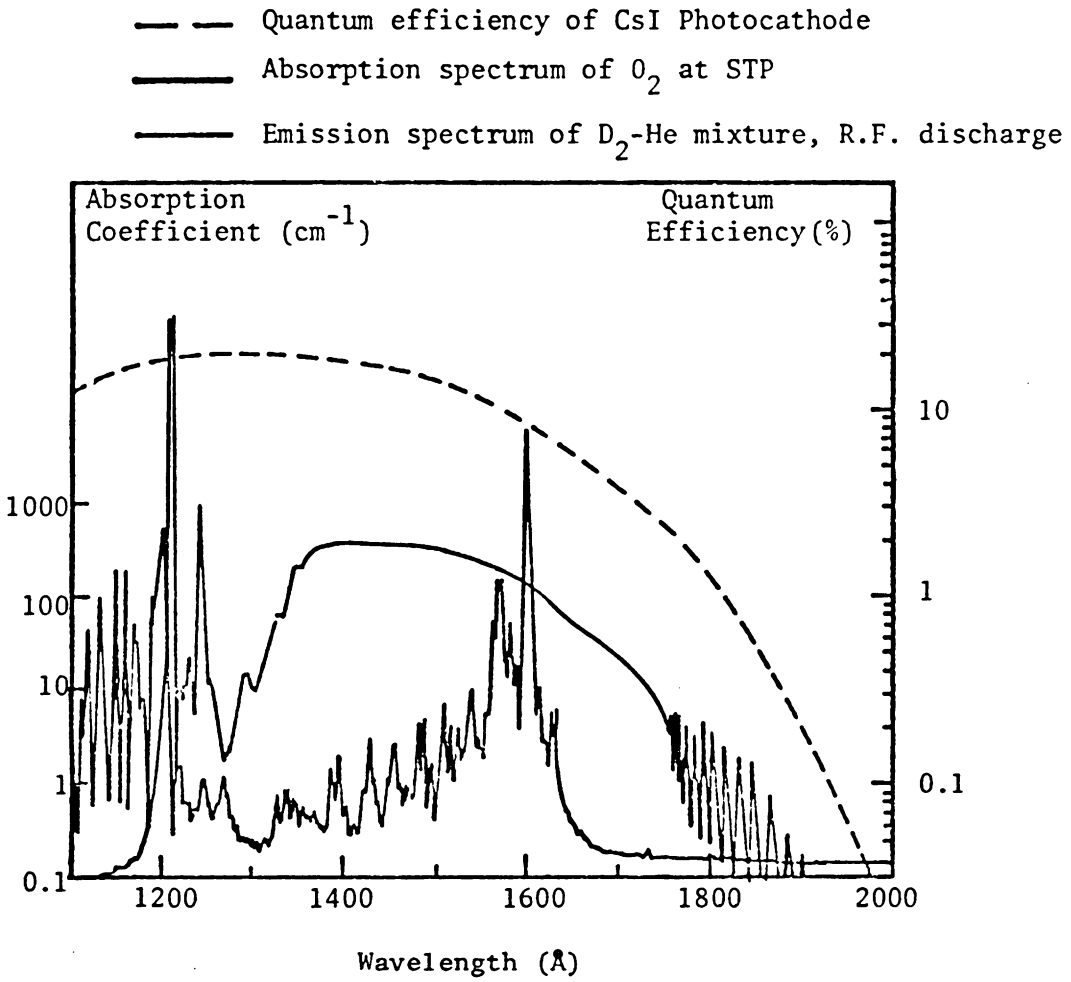

Figure 47. Isolation of Lyman-α Radiation by the O_2 Molecular Filter.

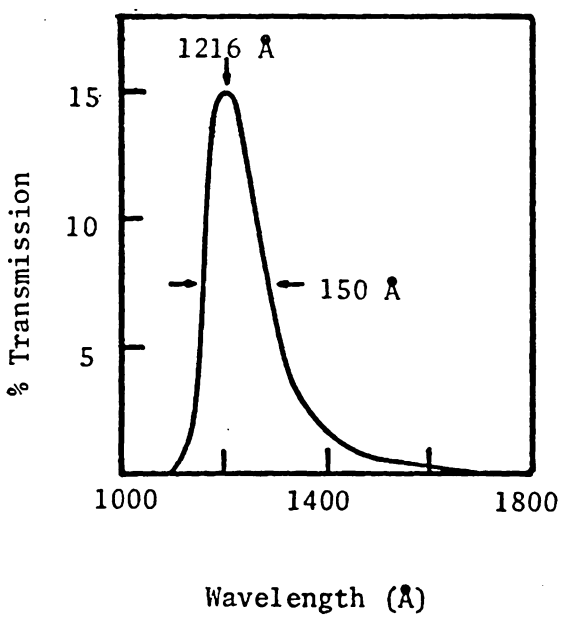

Figure 48a. Lyman-α Filter Transmittance.

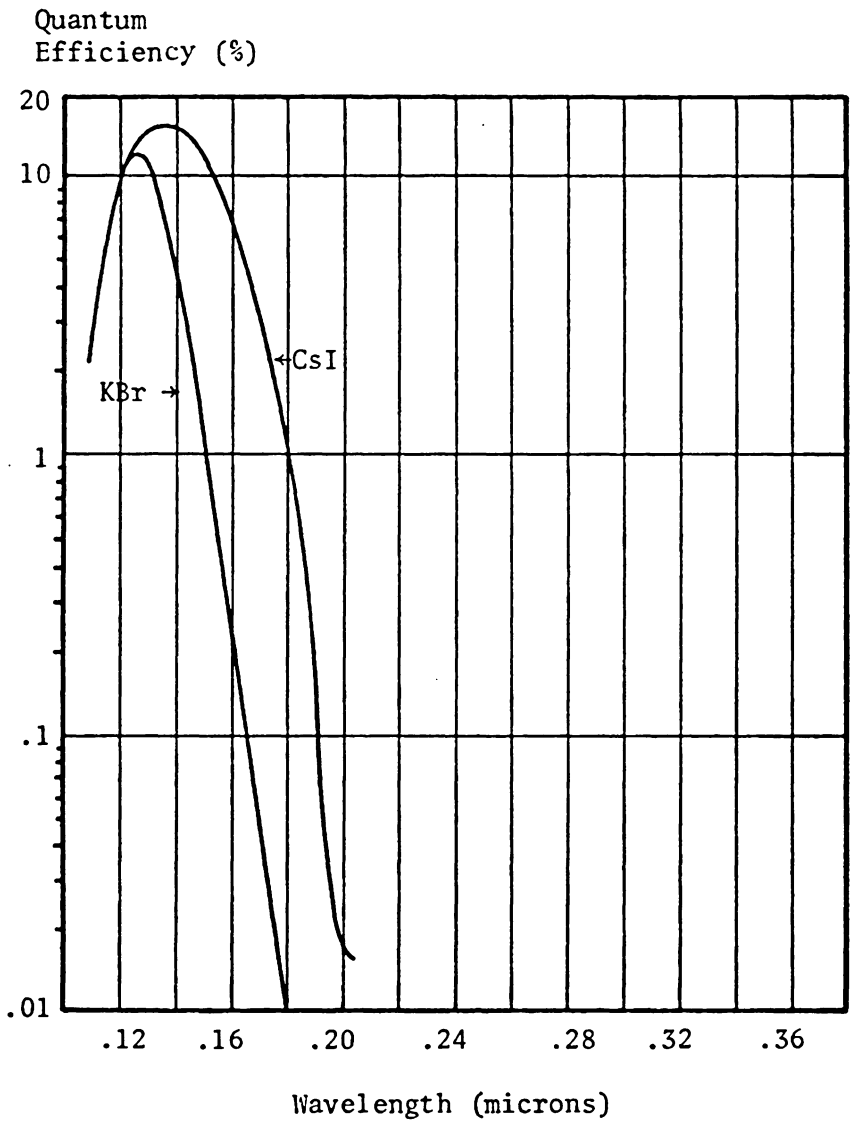

Figure 48b. Photomultiplier Sensitivity, Spectral Response Vs. Wavelength.

ranges are desirable.

5.1 Data Analysis

For the complete analysis of a kinetic shot, the following basic procedures were necessary:

5.1a) Determination of ϵ (molecular) from low temperature runs

5.1b) Determination of baseline correction from high temperature data. A separate correction was determined from the monochromator and filter pictures.

5.1c) Use of ϵ (molecular) to locate time = 0 on the kinetic pictures for H atom analysis.

These procedures will be discussed in greater detail.

For both sets of data (monochromator and Lyman-α filter data), it was necessary to locate the time = 0 point for the reflected shock by making use of the total molecular absorption. Even with the improved signal/noise levels obtained with the use of the Lyman-α filter, the neopentane pictures did not show a clear-cut transition in noise between the molecular absorption curve and the beginning of the H atom absorption curve, as shown in Figure 45, for a C_8H_{18} picture.

5.1.a Determination of ϵ (molecular)

The data analysis was performed in the following way. First, ϵ (molecular) was obtained by analyzing data from low temperature experiments. A typical cold shot, drawn for descriptive purposes is shown

in Figure 49a.

For total molecular absorption, $\Delta 1 = I_0$ and $\Delta 2 = I$ as shown on the figure. ϵ is calculated from $\epsilon = \frac{(\ln I_0/I)}{bc_5}$, where b = 7.5 cm and $c_5 = \frac{p_{5fract}}{RT_5}$. In this way, an average ϵ from several low temperature runs per mixture could be obtained. These results are shown in Table 17 and indicate good agreement between the values of ϵ obtained for the three mixtures. These were 7.2×10^7 cm^2/mol (20 ppm mixture), 6.9×10^7 $\frac{cm^2}{mol}$ (10 ppm mixture) and 7.4×10^7 cm^2/mol (5 ppm mixture). No noticeable trend of ϵ with temperature was found in these experiments, so the average of these values was assumed to apply at the (slightly) higher temperatures of the kinetics runs.

5.1.b Baseline Correction

The method of correcting the scope baseline for stray light is shown in Figure 50. A high temperature run normally shows an absorption curve which levels off to a nearly horizontal line at long time values. This portion of the picture, shown in Figure 50, is marked A. The scope baseline is marked B, and the resulting baseline correction is expressed as a percent of I_0. For the neopentane runs, baseline data was taken from 20 ppm runs at high T_5 values. These are presented in Table 18.

5.1.c Determination of Intensity at Time Zero

The absorption coefficient e for total molecular absorption was

Table 17. Low-Temperature Neopentane Experiments Used to Calculate ε (molecular)

20 ppm Neopentane in Ar*

Run	Shock Time (μsec)	P_1 (torr)	T_5 (°K)	P_5 (atm)	c_5** $(\frac{mol}{cm^3})$ x 10^{10}	ln I_0/I	ε $(\frac{cm^2}{mol})x10^{-7}$
Dec 17 #4	590	116.4	1081.4	2.54	5.61	.314	7.46
Dec 18 #2	589	100.2	1084.6	2.20	4.85	.268	7.37
Dec 18 #4	577	99.4	1125.4	2.33	4.95	.285	7.68
Dec 18 #6	578	99.1	1121.9	2.31	4.92	.208	5.64
Dec 22 #1	585	101.6	1098.0	2.28	4.96	.344	9.25
Dec 22 #2	583	100.3	1104.7	2.27	4.91	.187	5.08
Dec 23 #4	587	105.9	1091.3	2.35	5.15	2.78	7.20
Jan 4 #4	587	108.3	1091.3	2.40	5.26	.285	7.22
Jan 4 #7	587	107.9	1091.3	2.39	5.24	.321	8.17

ε average= $7.23x10^7$ cm^2/mol

10 ppm Neopentane in Ar**

#6	571	110.1	1146.8	2.66	2.77	.171	8.23
#7	573	113.4	1139.6	2.71	2.84	.132	6.20
#22	578	116.0	1121.9	2.70	2.88	.149	6.98
#30	591	102.0	1078.1	2.22	2.46	.079	4.28
#31	584	101.1	1101.4	2.28	2.47	.111	6.00
#34	590	103.9	1081.4	2.27	2.51	.186	9.89

ε average= $6.93x10^7$ cm^2/mol

5 ppm Neopentane in Ar***

#45	578	117.1	1122.0	2.72	1.45	.096	8.83
#47	599	136.5	1052.5	2.85	1.62	.076	6.26
#54	609	139.2	1021.8	2.75	1.61	.085	7.04

ε average= $7.38x10^7$ cm^2/mol

*Lyman-α radication detected by the monochromator and photomultiplier tube having a 10% quantum efficiency.

**c_5 = concentration of neopentane at time = 0 under reflected shock conditions = $P_5 fract/RT_5$. Fract = $19.6x10^{-6}$, $9.8x10^{-6}$, $4.9x10^{-6}$ for the three respective mixtures, corrected for the presence of butane in the neopentane.

***Lyman-α radiation was detected by the Lyman-α filter and photomultiplier tube having a 10% quantum efficiency.

then used to obtain the intensity at time zero for the kinetic experiments. If, initially, the baseline correction is disregarded, the procedure is, with reference to Figure 49, as follows:

1. Calculate ln I_0/I for each kinetic picture: ln $I_0/I = \epsilon\, b\, c_5$, where $\epsilon = \epsilon$ (molecular) has been obtained from low temperature data for the mixture under study.

   $b = 7.5$ cm

   $c_5 = \frac{P_5 \text{fract}}{RT_5}$, fract = 19.6×10^{-6}, 9.8×10^{-6}, 4.9×10^{-6} for the three mixtures (20, 10, 5 ppm neopentane in Ar)

2. Calculate I/I_0 ratio for each kinetic picture $I/I_0 = \frac{1}{\exp(\epsilon\, b\, c_5)}$.

3. Therefore $\Delta 2$ = I molecular = $(\frac{I}{I_0})\Delta 1 = (\frac{I}{I_0})\ (I_0)$.

The location of time = 0, as shown on Figure 49b, is determined by that point on the absorption curve equal to ($\Delta 2$ + scope baseline). It is convenient to measure $\Delta 2$ and the baseline in inches, since the chart paper is marked from 0-10 inches, with 0.1 inch scale divisions.

The procedure must be modified (Figure 49c) to account for the baseline correction which is due to light other than Lyman-α . One question that arises is the interaction between the molecular absorption and the baseline correction. The molecular absorption coefficient is a measure of the total reduction of energy by the molecules, but it is not clear whether the Lyman-α light and the light of other frequencies are absorbed to the same extent. If they are, then the baseline correction should be a certain fraction of $\Delta 2$, whereas if only the Lyman-α is absorbed, the correction should be the same

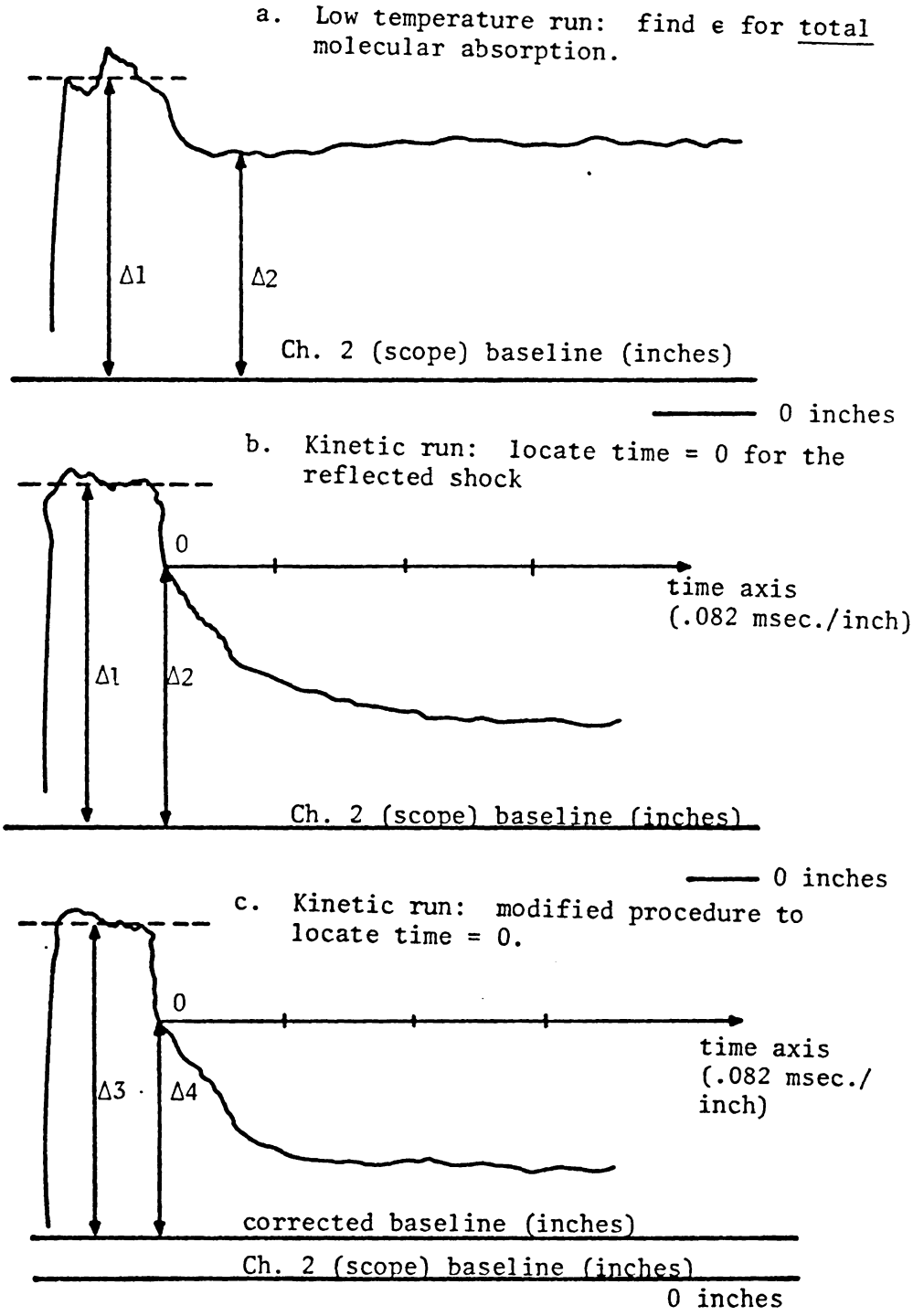

Figure 49. Use of Absorption Coefficient ε (molecular) to Obtain Time = 0. (Data analysis was performed on kinetic runs marked as in c. Δ4 is I_0 for H atom absorption).

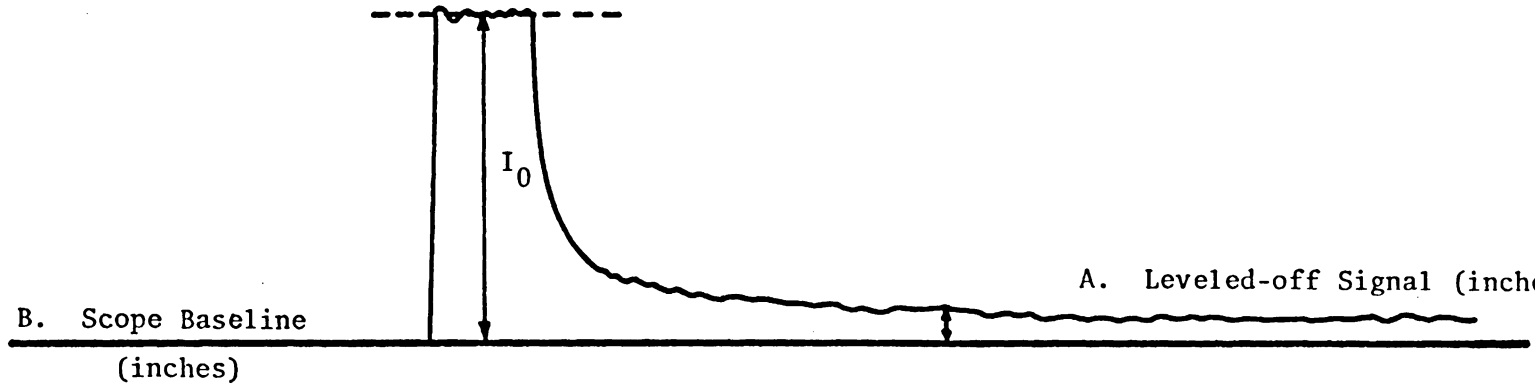

Baseline correction = $A-B/I_0$

The monochromator pictures: 14%
The filter pictures: 10%

Figure 50. High Temperature Run for Baseline Correction, Calculated as a Fraction of I_0.

Table 18. High Temperature Experiments for Baseline Correction

(20 ppm neopentane in Ar)

Run*	Shock Time (μsec)	P_1 (torr)	T_5 (°K)	P_5 (atm.)	$\frac{\Delta(A-B)}{I_0}$
Dec 17, 1981 #5	535	98.1	1289.8	2.88	.12
Dec 18, 1981 #1	543	104.3	1255.6	2.93	.15
Dec 18, 1981 #3	546	95.6	1243.1	2.64	.13
Dec 23, 1981 #1	545	99.3	1247.2	2.76	.15
Dec 23, 1981 #2	547	101.0	1239.0	2.78	.15
					.14 Average

Run **					
#55	541	95.2	1264.0	2.70	.083
#66	547	101.2	1239.0	2.78	.133
					.108 Average

*monochromator pictures

**Lyman-α filter pictures

fraction of ΔI. Since it is probable that the non Lyman-α light is of longer frequency than 1215 Å, and therefore, would not tend to be so strongly absorbed by hydrocarbon molecules, we have adopted the second approach, while realizing that the actual situation probably lies between these extremes. Fortunately, the two approaches lead to H atom concentrations which seldom differ by more than 3%.

$\Delta 4$ is consequently obtained by the equation $\Delta 4 = (\Delta 2/\Delta 1)\Delta 3$. $\Delta 4$ becomes I_0 for H atom measurements, and initial conditions for the reflected shock are thereby obtained from the absorption curve point ($\Delta 4$ + corrected baseline). Recorded data that is hard to read directly because of noise can be analyzed in a consistent manner by this method.

5.2 Calculation of k_1 for $C_5H_{12} \rightarrow C_4H_9 + CH_3$

After values of $\ln(I_0/I)$ as a function of time were obtained for each kinetic picture, H atom concentrations were determined from the calibration curves of Chiang, et al.[66]. The program LSQUARE, which fits a value of $\ln I_0/I$, obtained at T_5, to the calibration curves, was used.

In treating these data we initially obtained first-order rate constants for the formation of H atoms from neopentane, assuming an overall relationship

$$C_5H_{12} \rightarrow H + \text{other products},$$

and also assuming that one H was formed from each C_5H_{12} decomposed.

The approach was to either plot a graph of ln(a/(a-x)) versus time, where a is the initial concentration of neopentane and x the atom concentration, or else to calculate a least-squares line through these quantities. A typical graph is shown in Figure 51, indicating that good first-order dependence was found. Results of these calculations are shown in Table 20.

The rate constants of Table 20 have been used to calculate the parameters of an Arrhenius equation

$$k = Ae^{-E_a/RT} \qquad \ln k = \ln A - \frac{E_a}{R}\left(\frac{1}{T}\right).$$

By linear least squares, I obtain the equation

$$k = 2.65 \times 10^{17}\, e^{\frac{-86{,}270 \text{ cal/mole}}{RT}} \text{ sec}^{-1}$$

by using all of the 61 data points in Table 19. The standard deviation of the individual rate constants from the calculated line, in terms of log k, is 0.13, corresponding to a scatter in k of 35%. These points and the line given by the above equation are shown in Figure 52.

Such first-order dependence is to be expected from computer modeling of the reaction. The reactions listed in Table 19 taken mainly from Bradley's work[84], were considered those most likely to affect the H atom concentration. Rate constants shown are the most recent literature values. Numerical integration of this series of

Table 19. Rate Constants used in Computer Simulation of the Neopentane Pyrolysis Reaction Mechanism

	Reaction	A*	E_a (kcal/mol)	Reference
1.	$C_5H_{12} \rightarrow C_4H_9 + CH_3$	$.33 \times 10^{11}$	80.3	Bradley, 84
2.	$CH_3+C_5H_{12} \rightarrow CH_4+C_5H_{11}$	$.1 \times 10^{13}$	10.3	estimate**
3.	$H+C_5H_{12} \rightarrow H_2+C_5H_{11}$	$.27 \times 10^{14}$	9.7	Baker, et al., 91
4.	$C_4H_9 \rightarrow C_4H_8+H$	$.4 \times 10^{15}$	43.0	Bradley, 84
5.	$C_4H_9 \rightarrow C_3H_6+CH_3$	$.16 \times 10^{15}$	46.34	Bradley, 84
6.	$C_2H_6 \rightarrow 2CH_3$	$.5 \times 10^{17}$	88.39	Benson, 85
7.	$C_5H_{11} \rightarrow C_4H_8+CH_3$	$.1 \times 10^{13}$	34.0	Benson, 85
8.	$C_2H_5 \rightarrow C_2H_4+H$	$.3 \times 10^{14}$	40.61	Bradley, 84
9.	$CH_3+C_4H_8 \rightarrow CH_4+C_4H_7$	$.1 \times 10^{13}$	10.3	estimate**
10.	$C_4H_7 \rightarrow C_3H_4+CH_3$	$.1 \times 10^{15}$	48.49	Bradley, 84
11.	$CH_3+C_2H_5 \rightarrow CH_4+C_2H_5$	$.1 \times 10^{13}$	10.30	estimate**
12.	$2CH_3 \rightarrow C_2H_6$	$.84 \times 10^{13}$	0.0	Chiang, et al., 66
13A.	$C_5H_{12} \rightarrow C_4H_8+H+CH_3$	rate expression is a function of rate constants 1,4,5		
13B.	$C_5H_{12} \rightarrow C_3H_6+2CH_3$			
14†.	$C_4H_{10} \rightarrow 2C_2H_4+2H$	$.2 \times 10^{17}$	81.4	Cathonnet, et al., 86
15.	$H+C_2H_6 \rightarrow H_2+C_2H_4+H$	$.1 \times 10^{15}$	9.7	Bradley, 84
16.	$H+C_4H_8 \rightarrow H_2+C_4H_7$	$.5 \times 10^{14}$	3.9	Bradley, 84

*sec^{-1} for first order reactions; cm^3/mol sec for second order reactions

**Refer to Appendix I for explanation

† reaction to account for presence of 2% butane in the pure neopentane

Table 20. Rate Constants for Neopentane Kinetic Experiments

20 ppm Neopentane in Ar

ϵ (molecular) = 7.23×10^7 $cm^2/mol.$

Run	Shock Time (μsec)	T_5(°K)	P_5(atm)	P_1(torr)	k(sec^{-1})
Dec 28 #4	558	1195.3	2.76	106.5	49.21
Dec 28 #2	557	1199.2	2.74	105.4	66.29
Jan 4 #2	557	1199.2	2.80	107.4	43.88
Dec 21 #1	552	1218.8	2.67	99.8	89.11
Dec 23 #3	552	1218.8	2.77	103.5	60.85
Dec 23 #9	552	1218.8	2.81	105.1	70.02
Dec 21 #2	550	1226.8	2.69	99.6	159.81
Dec 23 #2	547	1239.0	2.78	101.0	149.76
Dec 18 #3	546	1243.1	2.64	95.6	193.49
Dec 23 #6	546	1243.1	2.79	100.9	129.72
Dec 23 #1	545	1246.2	2.76	99.3	268.91
Dec 17 #6	572	1143.1	2.45	101.8	21.38
Dec 22 #3	571	1146.7	2.38	98.7	7.53
Dec 22 #5	571	1146.7	2.36	97.8	6.13
Dec 17 #7	567	1161.3	2.49	100.9	26.07
Jan 4 #12	566	1165.0	2.70	109.0	12.82
Jan 4 #10	564	1172.5	2.73	108.9	16.46
Jan 4 #1	562	1180.0	2.71	107.1	28.01
Jan 4 #5	560	1187.6	2.76	107.7	27.60
Jan 4 #8	560	1187.6	2.76	107.7	24.83
Jan 4 #3	559	1191.4	2.77	107.6	22.16
Jan 4 #6	559	1191.4	2.77	107.7	30.48
Dec 28 #3	558	1195.3	2.73	105.5	35.33

5 ppm Neopentane in Ar

ϵ (molecular) = 7.38×10^7 $cm^2/mol.$

44	542	1259.9	2.73	96.5	353.62
48	558	1195.4	2.58	99.6	66.57
49	564	1172.6	2.67	106.6	26.18
50	547	1239.1	2.75	100.2	208.58
51	554	1211.0	2.55	96.3	109.42
53	550	1226.9	2.76	102.1	138.78

Table 20, continued

Run	Shock Time (μsec)	T_5(°K)	P_5(atm.)	P_1(torr)	k(sec^{-1})
10 ppm Neopentane in Ar					
ϵ (molecular) = 6.93 x 10^7 cm^2/mol					
1	556	1203.1	2.71	103.6	70.26
2	551	1222.8	2.75	102.2	124.59
3	544	1251.5	2.73	97.6	275.16
4	555	1207.1	2.78	105.7	50.25
5	565	1168.8	2.62	105.2	26.45
8	554	1211.0	2.57	97.2	74.13
11	561	1183.9	2.60	102.2	30.01
12	569	1154.0	2.64	108.0	12.98
13	550	1226.9	2.70	99.9	100.59
14	533	1298.7	2.63	88.6	1140.21
15	546	1243.2	2.72	98.5	140.07
19	565	1168.8	2.66	106.5	23.18
20	546	1243.2	2.75	99.7	141.64
21	550	1226.9	2.75	101.8	81.27
23	564	1172.5	2.59	103.4	23.62
24	548	1235.0	2.76	100.8	150.95
25	567	1161.4	2.63	106.8	18.43
26	542	1259.9	2.68	94.9	352.93
27	561	1183.9	2.65	104.1	33.79
32	547	1239.1	2.80	101.8	140.90
35	563	1176.3	2.62	103.8	30.67
36	555	1207.1	2.74	104.3	73.40
37	556	1203.1	2.78	106.2	56.59
38	556	1203.1	2.83	108.3	46.96
39	563	1176.3	2.82	111.7	24.85
40	556	1203.1	2.83	108.1	51.85
41	559	1191.5	2.81	109.3	39.99
42	550	1226.9	2.76	102.0	151.83
43	551	1222.8	2.78	103.3	101.32
20 ppm Neopentane in Ar					
ϵ (molecular) = 7.23 x 10^7 cm^2/mol.					
60	559	1191.4	2.63	102.1	28.90
62	556	1203.1	2.58	98.7	54.20
63	552	1218.8	2.56	95.6	106.92

of reactions indicated that Reactions 1 and 4, which together can be written $C_5H_{12} \rightarrow C_4H_8 + H + CH_3$, are the most important reactions influencing both the decomposition of C_5H_{12} and the formation of H atoms.

Of the other reactions, Reaction 5 causes about 10% of the t-butyl radicals to decompose to form CH_3 rather than H, so that the rate constant for the formation of H atoms from neopentane is 0.9 k_1 rather than simply k_1. Second, there is some loss of H atoms by Reaction 3. The reaction of neopentane with H atoms was studied by Baker, Baldwin and Walker[91], who compared the rate to that of H atoms with O_2. Using their recommended value of 9.7 kcal/mole for the activation energy of an H atom with a primary hydrogen, the equation

$$k_3 = 2.7 \times 10^{13} \exp(-9{,}700/RT) \text{ mole}^{-1}\text{cm}^3\text{s}^{-1}$$

is obtained. The rate constants of Table 19 lead to the conclusion that formation of H atoms from butane (Reaction 14) occurs with a rate constant close to that for formation of H atoms from neopentane, so that it is not necessary to make a correction for the presence of the butane.

In summary, the rate of appearance of H atoms can be written so

$$\frac{d[H]}{dt} = k[C_5H_{12}] = 0.9\ k_1\ [C_5H_{12}] - k_3[H]\ [C_5H_{12}]$$

from which

$$k = 0.1\ k_1 - k_3[H]$$

or

$$k_1 = (k + k_3[H]) / 0.9.$$

This equation has been used to evaluate k_1 from each of the values of k in Table 20. The values of k_1 range from 1.19 k at the lowest temperatures to 1.12 k at the highest temperatures. An Arrhenius equation for k_1 is

$$k_1 = 1.7 \times 10^{17} \exp(-84{,}000 \text{ cal/mole/RT}) \text{ s}^{-1}.$$

The standard deviation of the individual values of k_1 from the least-squares line, in terms of log k, is 0.11, corresponding to a scatter in k_1 of 30%. Consideration of possible uncertainty in the temperature (± 20K) and in the correction terms for obtaining k_1 from k lead to a total uncertainty in k_1 of about a factor of 2.

One other question that should be considered is the possible role of unimolecular fall-off of the first-order rate constant for Reaction 1. Since neopentane is a fairly large molecule, the experimental pressures are from two to three atmospheres, and the temperatures are not very high; it is to be expected from general chemical considerations[89,90] that the reaction will be close to, although not completely in, the first-order region. Probably $k_1/k_{1,\infty}$ will be at least 0.9, where k_1 is the observed rate constant and $k_{1,\infty}$ is the limiting high-pressure value.

In principle, this point may be tested by doing experiments at different pressures. In practice, since the pressure dependence is so small under our experimental conditions, we would not vary the

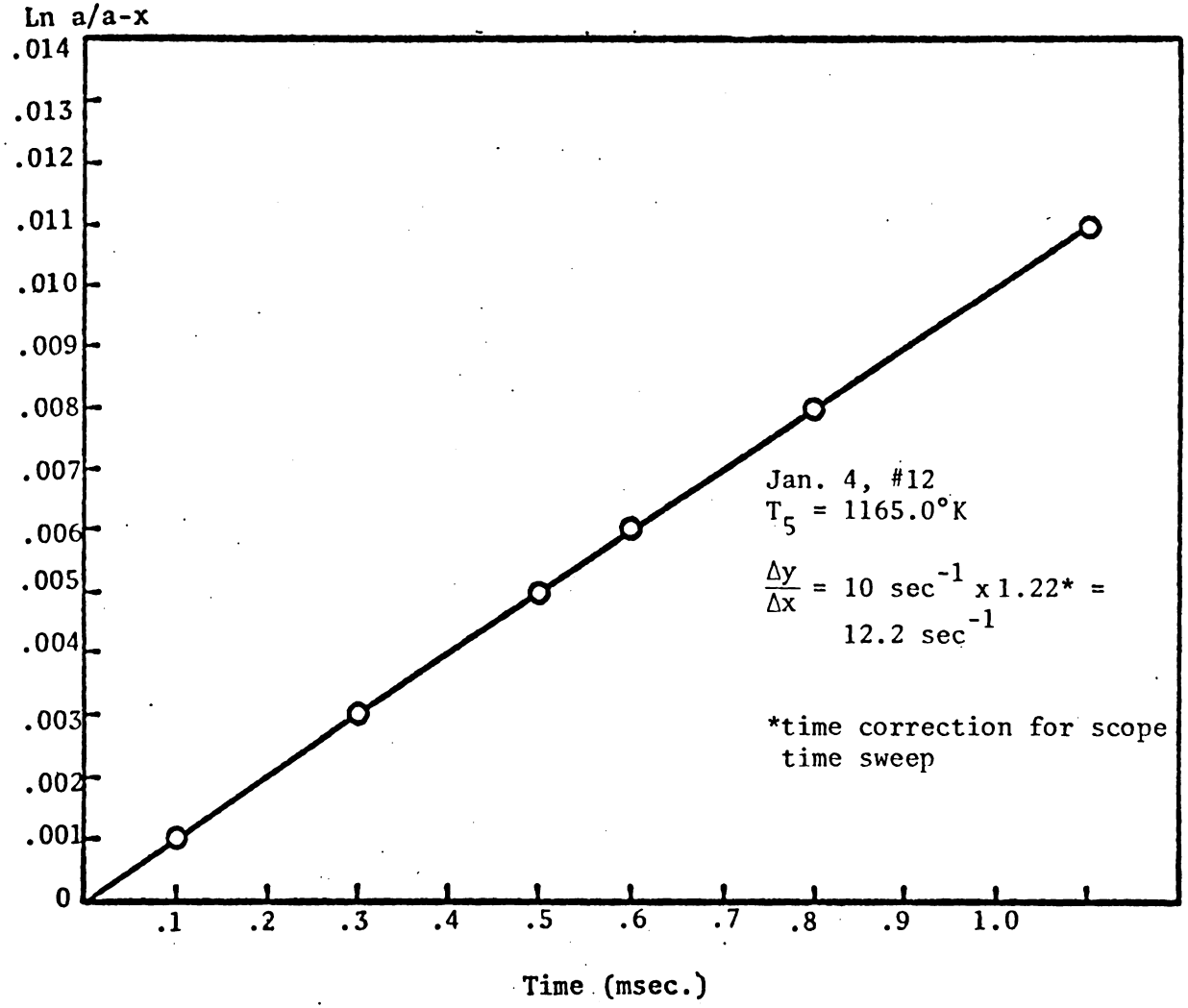

Figure 51. First Order Plot of Neopentane Data

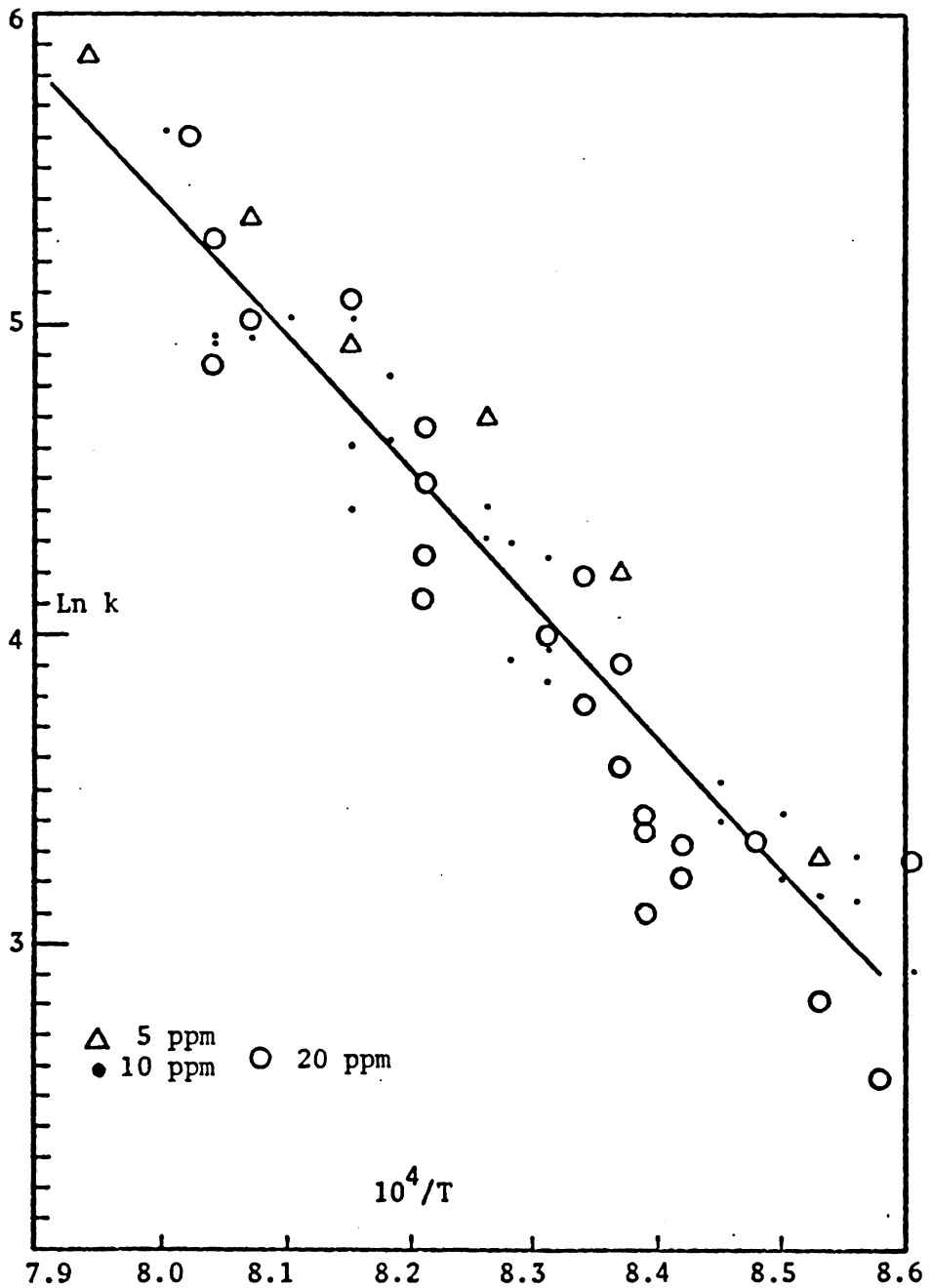

Figure 52. Arrhenius Plot of Neopentane Data.

pressure sufficiently to bring about measurable changes in rate constant. Accordingly, we can simply state that our value for k_1 is close to the $k_{1,\infty}$ value, and that the experimental scatter of the data of 30% is greater than the expected deviation due to fall-off.

IV. CONCLUSIONS

The rate constant k_1 from the present work is in good agreement with the results of Tsang[82] and Bradley[84]. A comparison of the rate constants over the experimental temperature range is shown in Table 21. The agreement between the three studies is gratifying, particularly because the studies were based on analyses of different reaction species, and because two different shock tube methods, the single pulse and conventional techniques, were utilized.

In the present study using the ARAS technique, the reaction scheme was simplified by using ppm amounts of reactant. The complex mechanism reduced to essentially one channel for neopentane decomposition. It would be interesting to monitor the reaction of a double ARAS technique. Another potential means of analysis would be via CH_3 radical, which absorbs at 2164 Å.

Table 21. Comparison of Rate Constants** for $C_5H_{12} \rightarrow C_4H_9+CH_3$ at 1100-1300°K.

Temp°K	Tsang*	Bradley*	This Work
1100	3.6	3.7	2.4
1150	17.2	18.1	13.0
1200	71.4	78.1	61.0
1250	265.0	300.0	252.8
1300	889.6	1041.0	939.9

*single pulse experiments

**$k(\text{Tsang}) = 1.26 \times 10^{16} \exp\left(\frac{-78200 \frac{\text{cal.}}{\text{mole}}}{RT}\right) \text{sec}^{-1}$

$k(\text{Bradley}) = 3.3 \times 10^{16} \exp\left(\frac{-80300 \frac{\text{cal.}}{\text{mole}}}{RT}\right) \text{sec}^{-1}$

$k(\text{this work}) = 1.7 \times 10^{17} \exp\left(\frac{-84800 \frac{\text{cal.}}{\text{mole}}}{RT}\right) \text{sec}^{-1}$

V. BIBLIOGRAPHY

1. A. N. Hayhurst and R. N. Telford, Combustion and Flame, 28, 67 (1977).

2. A. N. Hayhurst, et al., Combustion and Flame, 28, 123 (1977).

3. A. N. Hayhurst, et al., Combustion and Flame, 28, 137 (1977).

4. G. Sanzone, Ph.D. Dissertation, University of Illinois, Urbana, Illinois (1969).

5. P. Wegener, Ed., "Molecular Beams and Low Density Gasdynamics," Marcel Dekker, Inc., New York (1974).

6. J. N. Bradley and G. B. Kistiakowsky, J. Chem. Phys., 35, 256 (1961).

7. I. D. Gay, et al., J. Chem. Phys., 43, 1720 (1965).

8. A. A. Borisov, Kin. i. Kat., 9, 482 (1968).

9. S. C. Barton and J. E. Dove, Can. J. Chem., 47, 521 (1969).

10. S. H. Garnett, et al., J. Chem. Phys., 51, 84 (1969).

11. T. C. Clark, et al., J. Chem. Phys., 52, 4692 (1970).

12. A. Modica, J. Phys. Chem., 69, 2111 (1965).

13. R. W. Diesen, J. Chem. Phys., 39, 2121 (1963).

14. R. D. Kern and Nika, G., J. Phys. Chem., 75, 171 (1971), and other studies by Kern.

15. D. Gutman, et al., J. Phys. Chem., 70, 1793 (1966).

16. E. F. Greene and J. P. Toennies, "Chemical Reactions in Shock Waves," Academic Press, New York (1964). See also A.6. Gaydon and I. R. Hurle, "The Shock Tube in High Temperature Chemical Physics," Reinhold Publishing Corporation, New York (1963).

17. G. Skinner, J. Chem. Phys., 31, 268 (1959).

18. F. A. Goldsworthy, J. Fluid Mech., 5, 164 (1959).

19. D. L. Baulch, Ed., et al., "Evaluated Kinetic Data for High Temperature Reactions," V. 2, Butterworths, London (1973).

20. A. Hay, Ph.D. Dissertation, University of Illinois, Urbana, Illinois (1966).

21. W. Trafton, Ph.D. Dissertation, University of Illinois, Urbana, Illinois (1973).

22. A. Hay and R. L. Belford, J. Chem, Phys., 47, 3944 (1967).

23. E. R. Eckert and R. M. Drake, "Heat and Mass Transfer," McGraw-Hill, New York (1959).

24. R. Strehlow and R. L. Belford, Ann. Rev. Phys. Chem., 20, 247 (1969).

25. J. E. Dove and D. McL. Moulton, Proc. Roy. Soc. Lond., A283, 216 (1965).

26. C. P. Wang, Phys. Fluids, 11, 1865 (1965).

27. E.S.P. Notebooks. Property of the Sanzone group.

28. D. Gutman, Ph.D. Dissertation, University of Illinois, Urbana, Illinois (1965).

29. J. Dove, personal communication of November 9, 1979 to Diane Bernfeld.

30. J. Dove, personal communication of March 26, 1980 to Dr. A. Clifford.

31. G. Skinner, et al., J. Phys. Chem., 75, 1 (1971).

32. E. Rothkopf, et al., Phys. Fluids, 17, 1169 (1974).

33. L. Wachli, Technical Report AFFDL-TR-72-62 (1972).

34. H. Beske, et al., J. Mass. Spectrometer and Ion Physics, 7, 111 (1971).

35. H. Noller, "Rarefied Gas Dynamics," (Ninth International Symposium) V. 1, paper B-2, DFVLR-Press, Porz-Wahn (1974).

36. G. Sanzone, "Mass Spectrometry Notes" (Unpublished) (1974).

37. D. Price, et al., "T.O.F. Mass Spectrometry," Pergamon Press, Oxford (1969).

38. F. Robben, "Rarefied Gas Dynamics", (Ninth International Symposium) V. 2, paper C-2, DFVLR-Press, Porz-Wahn (1974)

39. Letter of July 9, 1980 to Diane Bernfeld from Varion, Inc.

40. Letter of August 14, 1980 to Diane Bernfeld from Perkin-Elmer Company.

41. Letter of February 21, 1980 to Diane Bernfeld from Cliftronics, Inc.

42. I. Krizancic, et al., Rev. Sci. Instrum. 50, 909 (1979).

43. T. Greenwood, et al., J. Spacecraft 8, 123 (1971).

44. M. Von Dongen, et al., "Rarefied Gas Dynamics," (Ninth International Symposium), V. 2, paper C-4, DFVLR Press, Porz-Wahn (1974).

45. I. Shames, "Mechanics of Fluids," McGraw-Hill, New York (1962).

46. E. Washburn, Ed., "International Critical Tables of Numerical Data," V. 5, McGraw Hill, New York (1930).

47. P. Kirstein, "Space Charge Flow," McGraw-Hill, New York (1967).

48. J. Pierce, "Theory and Design of Electron Beams," D. Van Nostrand Company, New York (1954).

49. E. Voldner, et al., "Proceedings on Shock Tubes and Waves," (Eleventh International Symposium), University of Washington Press, Seattle (1978).

50. J. Bander, M. S. Thesis, V.P.I. and S.U., Blacksburg, Virginia (1974).

51. W. Lipkea, et al., Combust. Sci. and Technol., 6, 257 (1973).

52. S. C. Baber, et al., Int. J. Chem. Kinetics, 7, 381 (1975).

53. A. Dean, Int. J. Chem. Kinetics, 8, 459 (1976).

54. G. Skinner, Int. J. Chem. Kinetics, 9, 863 (1977).

55. G. Skinner, et al., J. Phys. Chem., 75, 1 (1971).

56. A. Lifshitz, et al., J. Chem. Phys., 53, 3050 (1970).

57. G. Marsters, et al., "International Symposium on Shock Tubes (5th)," U.S. Naval Ordnance Laboratory, Silver Springs, MD (1965).

58. H. Ashkenas and F. Sherman, "Rarefied Gas Dynamics," (4th International Symposium) Academic Press, New York (1966).

59. D. Halliday and R. Resnick, Physics, John Wiley and Sons, Inc., New York (1963).

60. W. R. Hindmarsh, Atomic Spectra, Pergamon Press, Oxford (1967).

61. W. Braun, et al., J. Am. Opt. Soc. 60, 166 (1970).

62. F. Kaufman and D. Parkes, J. Chem. Soc. (Trans. Faraday Soc.) 66, 1579 (1970).

63. W. Braun and T. Carrington, J. Quant. Spectros. Rad. Transfer, 9, 1133 (1969).

64. D. Davis and W. Braun, Applied Optics, 7, 2071 (1968).

65. A. Lifshitz, et al., J. Chem. Phys., 70, 5607 (1979).

66. C-C. Chiang, et al., J. Chem. Phys., 70, 5614 (1979).

67. A. L. Myerson and W. S. Watt, J. Chem. Phys., 49, 425 (1968).

68. D. Appel and J. Appleton, "Proceedings on Shock Tubes and Waves", (Fifteenth International Symposium), The Combustion Institute, Pittsburgh (1975).

69. T. Just, et al., "Proceedings on Shock Tubes and Waves", (Sixteenth International Symposium), The Combustion Institute, Pittsburgh (1976).

70. P. Roth and T. Just, Ber. Bunsenges Phys. Chem., 79, 682 (1975).

71. A. Lifshitz, et al., "Proceedings on Shock Tubes and Waves", (Thirteenth International Symposium), SUNY Press, New York (1982).

72. C-C. Chiang, et al., J. Phys. Chem., 84, 939 (1980).

73. C-C. Chiang and G. Skinner, "Proceedings on Shock Tubes and Waves", (Eighteenth International Symposium), The Combustion Institute, Pittsburgh (1981).

74. C-C. Chiang and G. Skinner, "Proceedings on Shock Tubes and Waves", (Twelfth International Symposium), The Magnes Press, Jerusalem (1980).

75. W. Tsang, J. Chem. Phys., 44, 4283 (1966).

76. R. N. Burrell and A. F. Trotman-Dickenson, J. Chem. Soc. Part 4, 4218 (1960).

77. T. C. Clark, et al., J. Chem. Phys., 54, 1295 (1971).

78. A. Lifshitz, et al., J. Chem. Phys., 70, 5607 (1979).

79. K. Pamidimukkala, et al., J. Chem. Phys., 75, 1116 (1981).

80. K. Pamidimukkala and G. Skinner, "Proceedings on Shock Tubes and Waves," (Thirteenth International Symposium), SUNY Press, New York (1982).

81. P. Roth and R. Lohr, "Proceedings on Shock Tubes and Waves," (Thirteenth International Symposium), SUNY Press, New York (1982).

82. W. Tsang, J. Chem. Phys., 44, 4283 (1966).

83. W. Tsang, J. Chem. Phys., 43, 352 (1965).

84. J. Bradley and K. West, J. Chem. Soc. (Trans. Faraday Soc.), 72, 8 (1976).

85. S. Benson, ed., Kinetic Data on Gas Phase Unimolecular Reactions (NSRDS-NB521), NBS, Washington, DC (1970).

86. M. Cathonnet, et al., "Proceedings on Shock Tubes and Waves" (Eighteenth International Symposium), Combustion Institute, Pittsburgh (1981).

87. J. Kerr and M. Parsonage, Evaluated Kinetic Data on Gas Phase Hydrogen Transfer Reactions of Methyl Radicals, Butterworth's, London (1976).

88. K. Laidler, Theories of Chemical Reaction Rates, McGraw-Hill Book Company, New York (1969).

89. G. Skinner and B. S. Rabinovitch, J. Phys. Chem. 76, 2418 (1972).

90. D. M. Golden, et al., J. Phys. Chem. 75, 1333 (1971).

91. R. R. Baker, et al., J. Chem. Soc. (Trans. Faraday Soc.) 66, 2812 (1970).

VI. APPENDIX

APPENDIX A

Discussion of Estimated Rate Constants in Table 19

The estimates for reactions 2, 9 and 11 were based on data from the work of Skinner and coworkers. The literature rate constants for these second order reactions were in poor agreement. In addition, the only existing data on reaction 2 were obtained from low temperature experiments. It is well-known from the literature[87] that extrapolation of such data to ranges of higher temperature, such as those used in shock tube experiments, is not necessarily accurate; there is curvature in the Arrhenius plots at higher temperatures. Consequently, the following estimates for the rate constants of reactions 2, 9 and 11 were used, based on rate data from shock tube work.

The reaction $CH_3 + C_3H_8$ (propane) was considered to be a realistic model for the $CH_3 + C_5H_{12} \rightarrow CH_4 + C_5H_{11}$ reaction. Both reactions involve attack of a methyl group on two respective hydrocarbons of about the same alkane chain length. Consequently, the Arrhenius parameter E_a, which reflects the orientation effects of the CH_3 radical as it approaches the hydrocarbon molecule, and A, which is a function of hydrocarbon chain length, should be about the same for both reactions.* Similarly, reactions 9 and 11, which also

*Some of these qualitative arguments are discussed in references 87 and 88. Refer to the Evans-Polyani relationship for a discussion of factors which influence the activation energy.

involve methyl radical attack on two similar hydrocarbons, should have similar E_a and A values.

The vita has been removed from the scanned document

1. TEST OF THE COUPLED SHOCK-TUBE/MASS SPECTROMETER TECHNIQUE

2. THE PYROLYSIS OF NEOPENTANE BY ATOMIC RESONANCE ABSORPTION SPECTROPHOTOMETRY

by

Diane Lois Bernfeld

(ABSTRACT)

Part 1

The coupled shock-tube/mass spectrometer apparatus is characterized in terms of its capabilities for chemical kinetic studies. Criteria for doing kinetic measurements by this experimental technique are discussed.

The characterization experiments showed that our apparatus was capable of giving plausible signal shapes for non-reactive dynamic shots at P_1 = 5 torr. Measurements of ion current under static conditions showed that response of the quadrupole mass spectrometer was linear over a range of P_1 = 0-5 torr. Schlieren measurements indicated that the shock wave velocity was erratic and non-reproducible over the last 5 feet of the test section and that the velocity at the endwall could not be predicted from the schlieren data. The electron beam width was found to be $\sim$.1" and the implications of this measurement for further studies on the free jet are outlined. The present beam width is suitable for jet studies in which bulk ionization of gas from a cross-section of the jet is

performed. Design improvements needed for future reactive studies on our system are reviewed.

In addition, experimental studies of jet risetime with a pulsed molecular beam apparatus showed poor agreement between the experimental and theoretical jet risetimes. The apparent discrepancy is discussed and possible explanations for it are given.

Part 2

The rate constant k_1 for the reaction $C_5H_{12} \rightarrow C_4H_9 + CH_3$ was determined from reflected shock experiments (1100-1300°K) in which the progress of reaction was monitored by the appearance of H atoms. Atomic resonance absorption spectrophotometry at the Lyman-α line was performed on three mixtures (20 ppm, 10 ppm, 5 ppm) of neopentane in argon to give $k_1 = .17 \times 10^{18} \exp(-84800 \pm 6200/RT)\ sec^{-1}$. This result is in very good agreement with earlier single pulse shock tube experiments.

In addition, calibration experiments for H atom were performed by shock-heating two mixtures (10 ppm and 5 ppm) of neopentane in argon. The results obtained were in good agreement with previous calibration data.